

DISSERTATION ZUR ERLANGUNG DES DOKTORGRADES DER FAKULTÄT  
FÜR CHEMIE UND PHARMAZIE DER  
LUDWIG-MAXIMILIANS-UNIVERSITÄT MÜNCHEN

---

# Multi-Channel Orbital Tracking Microscopy

---

Frank Mieskes

aus

Ingolstadt, Deutschland

2024



## Erklärung

Diese Dissertation wurde im Sinne von §7 der Promotionsordnung vom 28. November 2011 von Herrn Prof. Don C. Lamb, PhD betreut.

## Eidesstattliche Versicherung

Diese Dissertation wurde eigenständig und ohne unerlaubte Hilfe erarbeitet.

München, den 04.11.2024

---

Frank Mieskes

Dissertation eingereicht am 13.11.2024

1. Gutachter: Prof. Don C. Lamb, PhD

2. Gutachter: Prof. Dr. Philip Tinnefeld

Mündliche Prüfung am 13.12.2024



A wizard is never late, Frodo Baggins, nor is he early! He arrives precisely when he means to.

---

*(Gandalf The Grey)*



# Abstract

Throughout the last decades, we could observe the tremendous advancements in fluorescence microscopy not only in sample preparation, but also in the development of instrumentation. This has made it possible to discover and understand cellular processes better. But every new discovery also raises new unanswered questions to be solved. This makes it mandatory to improve existing methods as well as to develop new techniques in this field.

A quite specialized and sophisticated subfield of fluorescence microscopy is Single Particle Tracking, providing high spatiotemporal information of the trajectories of individual particles. With this data, velocities and motion types of can be determined to describe transport mechanisms in biological systems. Extending the toolbox of existing particle tracking methods, leads to even better understanding of such processes.

3D Orbital Tracking is one tool of this box. By carrying out a correlation analysis on the obtained trajectories from living zebra fish larvae, it is possible to distinguish between active and passive transport. The big advantage of this approach lies in the intrinsic accessibility of the threshold, which distinguishes between the transport types, in the data. The corresponding details are described in the first part of the thesis.

The second part of the thesis will describe the redesign of the 3D Orbital Tracking software increasing the efficiency of data acquisition, enabling to perform particle tracking in solution with multichannel detection. With this, it is possible carry out dual color particle tracking as well as single particle tracking with simultaneous probing of FRET at 40 MHz resolution. By post processing of the FRET data, accurate FRET values are obtained.

In case of samples that cannot be fluorescently labeled, label free microscopy techniques have to be used. The final part of the thesis describes the software development for a Stimulated Raman Scattering microscope. The new software not only allows for scans but also for automatic spectra acquisition of selected points in the field-of-view. Furthermore, the scanning can be carried out in combination with single photon counting detection based on time correlated single photon counting arising from photoluminescence. The successful implementation of the software is proven by the investigation of the quality of graphene samples.





# Contents

<b>1</b>	<b>Introduction</b>	<b>1</b>
<b>2</b>	<b>Theoretical Background and Concepts</b>	<b>5</b>
2.1	Interaction of Light and Matter . . . . .	5
2.1.1	Fluorescence . . . . .	5
2.1.2	Scattering of Light . . . . .	10
2.2	Light Microscopy . . . . .	15
2.2.1	The Diffraction Limit . . . . .	15
2.2.2	Confocal Microscopy . . . . .	16
2.2.3	Single Particle Tracking . . . . .	17
2.2.4	3D Orbital Tracking Microscopy . . . . .	24
<b>3</b>	<b>Trajectory data of antero- and retrograde movement of mitochondria in living zebrafish larvae</b>	<b>31</b>
3.1	Structure of Orbital Tracking Data File . . . . .	31
3.2	Correlation Analysis . . . . .	32
3.3	Key Results . . . . .	34
<b>4</b>	<b>Multicolor 3D Orbital Tracking</b>	<b>37</b>
4.1	Orbital Tracking Software . . . . .	38
4.1.1	Software Description: The Host . . . . .	40
4.1.2	Software Description: The real time (RT)-Target . . . . .	52
4.1.3	Software Description: The field programmable gate array (FPGA) . . . . .	54
4.2	Key Results . . . . .	58
<b>5</b>	<b>Software Development for Correlative Imaging by Stimulated Raman Scattering and Photoluminescence</b>	<b>61</b>
5.1	Software Description: The Host . . . . .	62
5.1.1	Settings Module . . . . .	64
5.1.2	Visualization Module . . . . .	66
5.1.3	Beam Modulation Module . . . . .	71
5.1.4	Toptica Module . . . . .	72
5.1.5	TimeHarp Module . . . . .	72
5.1.6	Data Stream Module . . . . .	72
5.2	Software Description: The RT Target . . . . .	73
5.2.1	Move Piezo . . . . .	74
5.2.2	Point Intensity . . . . .	74

5.2.3	Acquire Intensity . . . . .	75
5.2.4	Confocal Scan . . . . .	75
5.2.5	Error . . . . .	75
5.2.6	Stop . . . . .	75
5.3	Implementation: Field Programmable Gate Array . . . . .	76
5.3.1	Move Piezo . . . . .	77
5.3.2	Point Intensity . . . . .	77
5.3.3	Acquire Intensity . . . . .	77
5.3.4	Confocal Scan . . . . .	77
5.4	Software Proof of Concept on Graphene . . . . .	80
<b>6</b>	<b>Conclusion and Outlook</b>	<b>83</b>
	<b>Bibliography</b>	<b>85</b>
	<b>List of Abbreviations</b>	<b>91</b>
	<b>List of Figures</b>	<b>95</b>
	<b>List of Tables</b>	<b>97</b>
<b>A</b>	<b>Publications</b>	<b>99</b>
A.1	Trajectory data of antero- and retrograde movement of mitochondria in living zebrafish larvae . . . . .	99
A.2	Multicolor 3D Orbital Tracking . . . . .	106
<b>B</b>	<b>Acknowledgments</b>	<b>123</b>

## Chapter 1

---

# Introduction

Thanks to the development of highly sensitive devices, novel analysis tools and easy access to databases during this epoch of *Industry 4.0*, scientific investigations and developments have gained speed in obtaining results compared to several decades ago. A remarkable example is the pandemic outbreak of SARS-CoV-2, where scientists designed a novel messenger ribonucleic acid (mRNA) vaccine within a few months. Those drug development processes involved multiple complex steps such as the isolation of the SARS-CoV-2 virus from the infected organic tissue, purification/sequencing of its spike protein and finally the design and synthesis of the corresponding mRNA. Just a few years ago, such a rapid progress in developing a medical drug was just utopia.

However, the majority of cellular processes are still poorly understood or even unknown. Hence, a lot of efforts are devoted to their investigations. For example, it is mandatory to understand the cellular processes involved for the treatment of different diseases such as cancer, HIV or Morbus Alzheimer. Nowadays, scientists have access to multiple excellent methods, e.g. atomic force microscopy (AFM), nuclear magnetic resonance (NMR) spectroscopy, X-Ray crystallography or cryo electron microscopy (cryoEM), which enable the detection and structural analysis of (bio)molecules. However, these methods are not applicable *in vivo*. For example, experiments in X-ray crystallography require single crystals of the sample, which is not only extremely time as well as cost-consuming, but it cannot be guaranteed that the discovered structure is identical to the one in a cell or in solution. In cryoEM, the specimen is measured at cryogenic temperatures below  $-150^{\circ}\text{C}$ , which is way below the temperatures those molecules function at.

This is where fluorescence microscopy plays a major role, bridging the *in vivo* gap. Classical microscopy exploits the physical properties of fluorescence (see subsection 2.1.1) as imaging contrast. If the system of interest is not able to fluoresce it needs to be labeled with fluorescent emitters, such as organic fluorophores, in order to visualize it. In addition to these small organic molecular markers, *Shimomura's* discovery of the green fluorescent protein (GFP) in the jellyfish *aequorea victoria* (Shimomura, Johnson, and Saiga, 1962) demonstrated the ability of proteins to autonomously become fluorescent. Big efforts have been spent on improving the fluorescent properties and expanding the spectral coverage of fluorescent proteins as well as developing labeling and expression techniques for them. For example, decades of such work made it possible to decode the dynamic processes of HIV-1 Gag (Qian et al., 2022).

Parallel to the development of fluorescent probes, considerable efforts have been put into the improvement of microscopy techniques - and it is still ongoing. Nowadays, in fluo-

rescence microscopy, detecting single molecules is state-of-the-art. A standard method is the illumination of immobilized, fluorescently labeled species using a total internal reflection (TIR) geometry. In this configuration, the signal of dyes in a certain field-of-view (FOV) is recorded by an electron multiplying charge-coupled device (EMCCD) or a complementary metal-oxide-semiconductor (CMOS) sensor. Extending the microscope to multiple excitation and detection sources allows for investigating molecular interactions based on single molecule assays, such as Förster Resonance Energy Transfer (FRET), protein induced fluorescence enhancement (PIFE) or quenching, with high throughput (Lerner et al., 2016; Smit et al., 2019). Furthermore, it is possible to monitor long fluorescent traces on the order of seconds to minutes of each single molecule in the FOV. However, careful interpretation of the obtained data is needed. The immobilized molecules are hindered in their degrees of freedom regarding rotation, which can bias their interaction. A second standard approach, which can monitor such fast transitions in solution, uses confocal microscopes equipped with avalanche photodiode (APD). Prominent methods are  $\mu$ s-alternated laser excitation (ALEX), ns-ALEX or pulsed interleaved excitation (PIE) - multiparameter fluorescence detection (MFD) (Kapanidis et al., 2005; Müller et al., 2005; Widengren et al., 2006; Kudryavtsev et al., 2012). Compared to TIR fluorescence setups, PIE with MFD microscopes have higher time resolution due to the pulsed excitation sources, fast point detectors and time correlated single photon counting (TCSPC) logic. With this approach, it is possible to extract multiple parameters from the obtained data such as fluorescent lifetime or anisotropy. However, PIE - MFD data does not consist of long fluorescent traces of individual fluorophores but of bursts representing snapshots of an ensemble of molecules. For investigating biological samples on the the single molecule level, it is necessary to combine those two microscopy techniques to obtain a full picture of the system. It would be beneficial to combine the advantages of the described approaches for monitoring long FRET traces in solution within one experiment. For this, it is necessary to follow a particle of interest on the fly. A sub field in fluorescence microscopy which is capable of doing so is single particle tracking (SPT) (see subsection 2.2.3).

One technique in this subfield is three dimensional (3D) Orbital Tracking microscopy, a feedback based approach (see subsection 2.2.4). The hereby acquired high resolution data allows for accurate analysis of particle movement. This will be presented in chapter 3 where a correlation of trajectories is performed on moving mitochondria in living zebra fish larvae.

Chapter 4 of this thesis will highlight the improvement of the existing 3D Orbital Tracking microscope. First, I will explain the redesign of the software to use the queued message handler (QMH) architecture increasing the performance and enabling the implementation of further features. Next, results of dual-color tracking experiments in solution, including the first successful simultaneous tracking of two individual particles using a feedback approach, will be presented. The last part of this chapter will describe the results of 3D single particle tracking while probing FRET in solution using the novel orbit point single photon counting (OPSPC) data acquisition algorithm.

When studying molecules that are similar in size or even smaller than the fluorescent label, fluorescent labeling can strongly interfere with their biological function. In this

case, fluorescence cannot be exploited for imaging contrast. Here, label-free imaging techniques play a major role. One of them is Stimulated Raman Scattering (SRS) microscopy. In chapter 5 of this thesis, the novel measurement software for carrying out SRS experiments will be presented. Its architecture is based on the QMH design, which allows for executing fast scans and can be combined with photon counting in parallel using TCSPC, followed by automated spectra acquisition.



## Chapter 2

---

# Theoretical Background and Concepts

When enjoying a glass of gin tonic on a hot and sunny summer day, it might be observed that the drink glows in a pale blue color. Exactly this phenomenon was first described by *Sir John Frederick Gabriel Herschel* in 1845 (Herschel, 1845). Today the source of that "magical" behavior is known. It is the light emitted from quinine molecules that are ingredients in tonic water. The phenomenon, known as fluorescence, is the basis of modern fluorescence microscopy. With this technique, it is not only possible to investigate biological processes in vitro for developing new drugs, it is furthermore a standard method in laboratories to detect diseases in biological tissues by target specific labeling.

In the following chapter, the theoretical background for techniques used in this thesis will be highlighted. Starting with the interaction of light and matter in the first two sections, a discussion follows on confocal microscopy. With those sections being the theoretical basis for modern microscopy, SPT, a subfield of fluorescence microscopy, will be highlighted in detail. Here, the main focus will be set on 3D Orbital Tracking, which is a confocal feedback based SPT technique.

## 2.1 Interaction of Light and Matter

### 2.1.1 Fluorescence

#### Absorption and Emission Processes

*Herschel's* observation of "glowing" tonic water led to further investigation of this phenomenon. Today, it is well known that the process of fluorescence is based on the interaction of fluorescent materials with light. In this case, molecules absorb photons and undergo a transition to an energetically excited state. The energy of the photon has to match the energy gap between two electronic states of the molecule and can be calculated by *Planck's* law

$$E = \frac{hc}{\lambda} \quad (2.1)$$

where  $h$  is *Planck's* constant,  $c$  the speed of light and  $\lambda$  the wavelength of the corresponding photon (Planck, 1900). The molecule aims to reach back to its energetic ground state, i.e. the absorbed energy has to be released again. In figure 2.1, example spectra for absorption and emission of the fluorescent dye ATTO647N are shown.

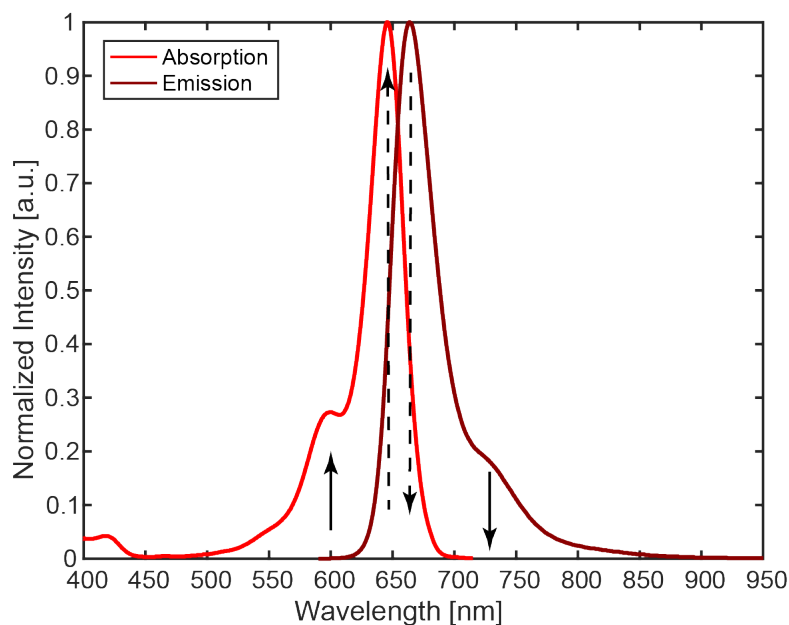


**Figure 2.1: Absorption and emission spectra of ATTO647N.**<sup>1</sup>Due to the *Stokes* shift, the emission spectrum is shifted to higher wavelengths compared to the absorption spectrum.

The processes responsible for the spectra in figure 2.1 can be described by a *Jablonski* diagram developed by *Aleksander Jablonski* and published in 1935 (Jablonski, 1935). In this representation, the nuclei coordinates of the molecule are neglected and not shown in the diagram. This convention results from the *Born-Oppenheimer* approximation which states that the motion of heavy (nuclei) and light (electrons) particles takes place on different time scales (Born and Oppenheimer, 1927). This assumption allows for the separate treatment of the wave functions of nuclei and electrons. An example of a *Jablonski* diagram is given in figure 2.2. Here, only the ground state  $S_0$  as well as the first excited states  $S_1$  and  $T_1$  are shown which is a consequence of *Kasha's* rule that will be discussed later on. In general, electron transitions between electron states of different energies are represented by vertical arrows. After the excitation of an electron from the ground state to a higher electronic state, it reaches a vibronic state of  $S_1$  by *Internal Conversion* followed by vibrational relaxation to vibronic ground state of  $S_1$ . From this point on, several pathways for the electron to reach back to  $S_0$  exist. In general, they can be split into non-radiative and radiative processes. In the lowest vibrational state of  $S_1$ , the system again can undergo *Internal Conversion*, an iso-energetic transition, reaching a highly energetic vibronic level  $S_0$  from which the electron relaxates to the vibronic ground state. Other non-radiative pathways which are worth to be mentioned are quenching, solvent relaxation or FRET. The process of FRET will be discussed in more detail on page 8.

Furthermore, it is possible that an electron reaches back to the electronic ground state by

<sup>1</sup>from: <https://www.atto-tec.com/ATTO-647N.html> (22.12.2022)



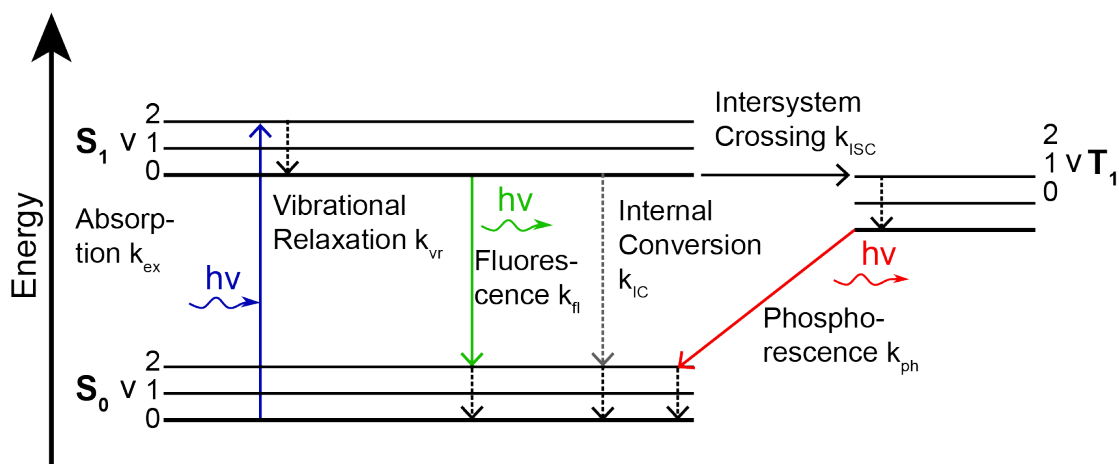


**Figure 2.2: Jablonski diagram.** By absorbing a photon, a fluorophore is excited from the ground state to a higher vibronic state of  $S_1$  (blue arrow,  $k_{ex}$ ). By vibrational relaxation (black dashed line,  $k_{vr}$ ) the electron moves to the vibronic ground state of  $S_1$  from where the electron can return to  $S_0$  by emitting a photon (green arrow,  $k_{fl}$ ). A non-radiative pathway (gray dashed arrow,  $k_{IC}$ ) with constant spin multiplicity is the process of Internal Conversion, an iso-energetic transition to a higher vibronic state of  $S_0$  followed by vibrational relaxation to the ground state. Furthermore, an iso-energetic transfer with a change of spin multiplicity to a higher vibronic state of  $T_1$  can occur (black horizontal arrow,  $k_{ISC}$ ). The lifetime of this state is on the order of seconds due to spin-forbidden emission of a photon (red arrow,  $k_{ph}$ ).

emitting a photon. As mentioned before, the *Jablonski* diagram illustrated in figure 2.2 only shows the energetic ground state and the first excited state. The reason for this is *Kasha's rule*, an empiric rule which states that spontaneous emission processes only occur from the lowest excited state to the ground state of same multiplicity (Kasha, 1950). When comparing the energies of absorbed and emitted photons, an important fact arises. Due to vibrational relaxation, the emitted photon is always lower in energy. In honor of *Sir George Gabriel Stokes*, this red shift is termed the *Stoke's shift* (Stokes, 1852).

A third pathway is the process of *Intersystem Crossing*. Similar to *Internal Conversion*, the system undergoes an iso-energetic transition. However, the spin multiplicity does change here, meaning that the system switches from the ground state of  $S_1$  to a higher vibronic state of the first excited triplet state  $T_1$ . After vibrational relaxation to its vibronic ground state, the system remains in  $T_1$ . Since the emission of a photon is spin forbidden, the life time of the triplet state can be on the order of seconds. This type of emission is also known as phosphorescence.

Radiative and non-radiative processes are always in competition with each other. To obtain a measure for which of the processes is dominant, the quantum yield  $\Phi$  can be taken into account. This is the ratio of emitted and absorbed photons of a molecule. As shown in Equation 2.2, it can be calculated from the the rates  $k$  of the different pathways

$$\Phi = \frac{k_{fl}}{k_{fl} + \sum k_{nr}} \quad (2.2)$$

where  $k_{fl}$  is the rate of fluorescence and  $k_{nr}$  rates of non-radiative pathways, e.g.  $k_{IC}$  and  $k_{ISC}$ . It is desirable, that the quantum yield of fluorophores is as high as possible.

### Förster Resonance Energy Transfer

As described in the previous subsection, one non-radiative pathway is FRET. This phenomenon was theoretically described by *Theodor Förster* (Forster, 1946; Förster, 1948). After exciting a fluorescent emitter (*donor*), the energy can be transferred to a second molecule (*acceptor*) by dipole-dipole interactions. The acceptor can now emit a photon of wavelength that is not covered by the emission spectrum of the donor. A corresponding *Jablonski* diagram describing the involved processes is given in figure 2.3.

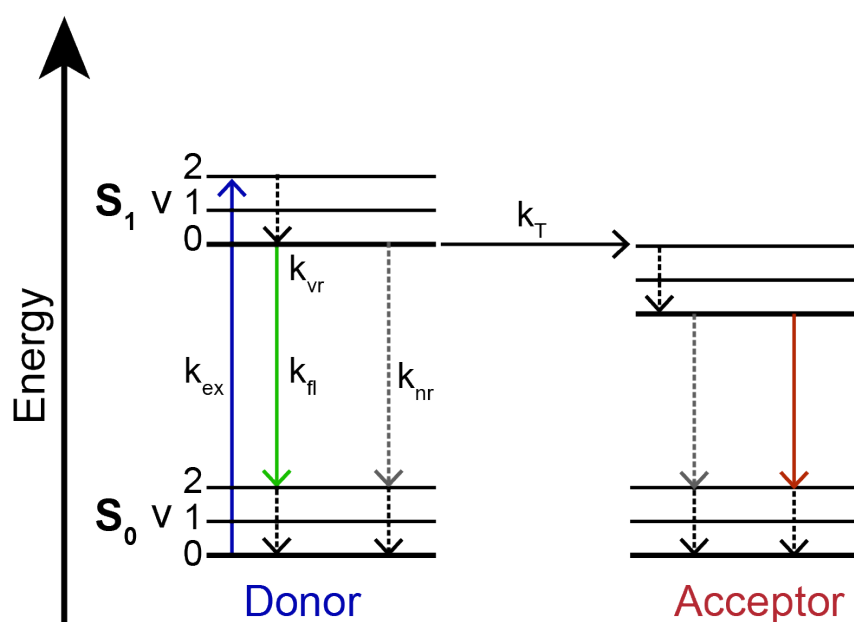


**Figure 2.3: Jablonski diagram illustrating the processes of FRET.** By absorbing a photon, the donor is excited from the ground state to a higher vibronic state of  $S_1$  (blue arrow,  $k_{ex}$ ). After vibrational relaxation (black dashed line,  $k_{vr}$ ) to the vibronic ground state of  $S_1$ , the donor can return to  $S_0$  by emitting a photon (green arrow,  $k_{fl}$ ) or by non-radiative decay (gray dashed arrow,  $k_{nr}$ ) as discussed in subsection 2.1.1. It is further possible, that the energy is transferred to the acceptor by dipole-dipole interactions (black horizontal arrow,  $k_T$ ), exciting the electron of the acceptor to a higher vibronic state of  $S_1$ .

Without photon absorption, the acceptor is now in the excited state  $S_1$  and, as described in subsection 2.1.1, several pathways are available to return the system back to the electronic ground state. For FRET to occur, there needs to be an overlap of the donor's emission spectrum with the acceptor's excitation spectrum. As can be seen in the *Jablonski* diagram, a new parameter,  $k_T$ , which is the energy transfer rate, is introduced. It can be calculated by

$$k_T = \frac{1}{\tau_D} \left( \frac{R_0}{R} \right)^6 \quad (2.3)$$

with  $\tau_D$  being the lifetime of the donor in the absence of an acceptor,  $R$  the distance between the FRET pair and  $R_0$  the *Förster* radius, which is the characteristic distance between two fluorophores at which the efficiency of energy transfer is 50 %. Instead of the energy transfer rate, the FRET efficiency is a more intuitive measure. It can be calculated using Equation 2.4:

$$E = \frac{k_T}{k_T + k_{fl} + k_{nr}} \quad (2.4)$$

Together with equations 2.3 and 2.4, the FRET efficiency  $E$  can be rewritten as a function of distance.

$$E = \frac{R_0^6}{R_0^6 + R^6} \quad (2.5)$$

As can be seen, it is strongly dependent on the distance  $R$  between both dyes and the *Förster* radius  $R_0$ , making it suitable for measuring molecule interactions on the nanometer scale. Furthermore,  $R_0$  depends on the surrounding of the dyes and can be calculated as follows

$$R_0^6 = \frac{9000(\ln(10))\kappa^2 J(\lambda)\Phi_D}{128n^4\pi^5 N_A} \quad (2.6)$$

with  $\kappa$  being a function of the relative orientation of the dipole,  $J(\lambda)$  the overlap integral,  $\Phi_D$  the quantum yield of the donor,  $N_A$  *Avogadro's* constant and  $n$  the refractive index of the medium.

The uncorrected FRET efficiency,  $E^*$ , known as the proximity ratio is experimentally accessible by measuring the fluorescent intensities  $F_{XY}$  of the dye pair, respectively. In the notation of  $F_{XY}$ ,  $F$  is the background corrected fluorescence intensity measured with X laser excitation detected in channel Y. The proximity ratio can then be calculated using Equation 2.7.

$$E^* = \frac{F_{DA}}{F_{DA} + F_{DD}} \quad (2.7)$$

However, the value of  $E^*$  is biased. Hence, it is not suitable for calculating  $R$  and can lead to wrong values and misinterpretation of the results. The correct distance of a dye pair is only accessible by correcting the  $E^*$  for direct excitation  $\alpha$ , spectral crosstalk  $\beta$  and the detection efficiency  $\gamma$ . All correction factors are intrinsically present in the data of PIE-MFD (Müller et al., 2005; Kudryavtsev et al., 2012) or ALEX (Kapanidis et al., 2004) experiments. They can be calculated with the following formulas

$$\alpha = \frac{F_{DA}^{A_{\text{only}}}}{F_{AA}^{A_{\text{only}}}}, \quad \beta = \frac{F_{DD}^{D_{\text{only}}}}{F_{DA}^{D_{\text{only}}}}, \quad \gamma = \frac{\Phi_A \eta_A}{\Phi_D \eta_D} \quad (2.8)$$

in which  $F_{XY}^{\text{Aonly}}$  represents the detected fluorescence signal of the acceptor in the absence of the donor and  $F_{XY}^{\text{Donly}}$  detected fluorescence signal of donor in the absence of the acceptor. With these correction factors, the proximity ratio  $E^*$  from Equation 2.7 can be extended to accurate FRET efficiency.

$$E = \frac{F_{\text{DA}} - \alpha F_{\text{AA}} - \beta F_{\text{DD}}}{F_{\text{DA}} - \alpha F_{\text{AA}} - \beta F_{\text{DD}} + \gamma F_{\text{DD}}} \quad (2.9)$$

## 2.1.2 Scattering of Light

Besides fluorescence discussed in subsection 2.1.1, another interaction of light with matter is scattering. This can appear in two different processes: elastically and inelastically. In elastic scattering, which is termed *Rayleigh* scattering, the energy of the scattered photon is preserved, i.e. incident and scattered light are of same wavelength  $\lambda$  (Strutt, 1871). During inelastic scattering, known as *Brillouin* and *Raman* scattering, energy is exchanged between the incident photon and the scattering medium. In particular, *Raman* scattering, i.e. scattering between light and optical phonons in the medium, is isotropic and can occur in a bidirectional manner (Raman and Krishnan, 1928). Its mechanism is shown in figure 2.4.

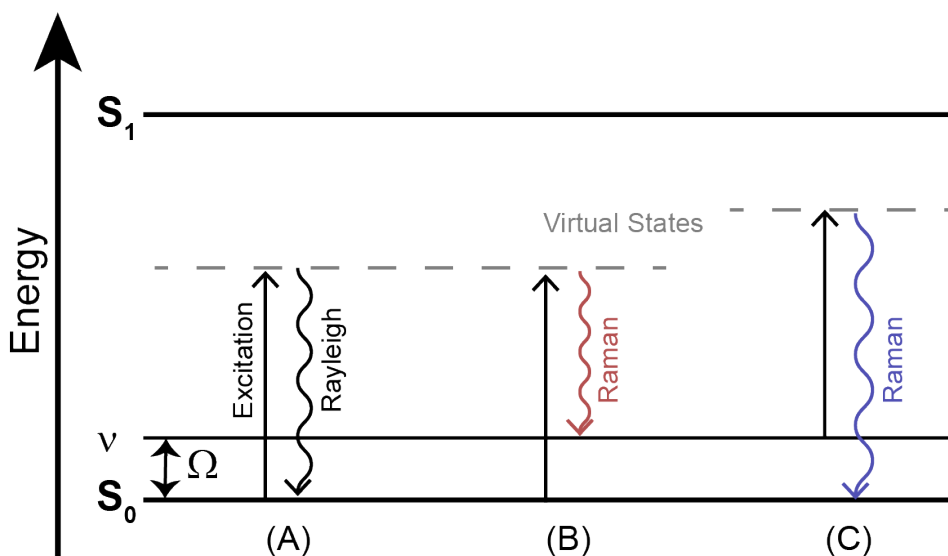


**Figure 2.4: Jablonski diagram illustrating *Raman* scattering processes.** (A) Elastic or Rayleigh scattering: during this process, the energy of the scattered photon is preserved. (B) Red-shifted inelastic scattering (Stokes): the scattering medium is in the vibrational ground state of the electronic ground state  $S_0$ . Collision with a photon leads to an occupation of a virtual state (left grey line). The energy is transferred from the photon to the medium being then in the first vibrational state of  $S_0$ . (C) Blue-shifted inelastic scattering (Anti-Stokes): the scattering medium is in the first vibrational state of  $S_0$ . Collision with a photon leads to an occupation of a virtual state (right grey line). The energy is transferred from the medium to the photon with the system being in the vibrational ground state of  $S_0$ .

Panel **(A)** illustrates the process of *Rayleigh* scattering in which the incident and scattered photon are of same wavelength. Panels **(B)** and **(C)** sketch the two possibilities of energy transfer between the incident photon and the molecule during *Raman* scattering. In case **(B)**, energy is transferred from the photon to the molecule with the result of a spectral red shift of the scattered light. In panel **(C)**, the molecule is already vibrationally excited. During interaction with light, the molecule relaxes to the vibrational groundstate, energy is released and the scattered light undergoes a blue shift. To align with the naming convention in fluorescence, these energy shifts are called Stokes- and anti-Stokes shift, respectively.

Generally, the cross section for *Raman* scattering ( $10^{-28}$  to  $10^{-30}$  cm<sup>2</sup>) is magnitudes of order smaller compared to Fluorescence ( $10^{-19}$  cm<sup>2</sup>), which means that this process is very rare resulting in very low detection signals and/or elevated excitation powers of the light sources (Tittel, Knechtel, and Ploetz, 2023). However, several techniques exist to increase the signal of scattered light such as Tip-Enhanced Raman Scattering (TERS) (Fleischmann, Hendra, and McQuillan, 1974), Surface-Enhanced Raman Scattering (SERS) (Pérez-Jiménez et al., 2020), Coherent Anti-Stokes Raman Scattering (CARS) (Zumbusch, Holtom, and Xie, 1999) or SRS (Ploetz et al., 2007; Freudiger et al., 2008). As SRS will be employed later in this thesis, it will be discussed together with spontaneous Raman in the following section.

### Spontaneous Raman Scattering

As already mentioned, energy is exchanged between the incident photon and the molecule during Raman scattering. This can be expressed as

$$\omega_{Raman} = \omega_{ex} \pm \Omega \quad (2.10)$$

where  $\omega_{Raman}$  as well as  $\omega_{ex}$  denote the frequencies of the scattered and incident photons and  $\Omega$  the frequency of the molecular vibration. Depending on the sign of  $\Omega$ , the scattered photon (de-)excites vibrational state of the material. In a classical approach, this can be described in bulk by two molecules representing a spring that oscillate with a frequency  $\Omega$

$$q(t) = q_0 \cos(\Omega t) \quad (2.11)$$

where  $q$  is the distance between both centers of mass.

The incident photon can be expressed as an oscillating electric field

$$E(t) = E_0 \cos(\omega_{ex} t) \quad (2.12)$$

that induces a microscopic dipole momentum  $\mu(t)$  on the molecule

$$\mu(t) = \alpha(t)E(t) \quad (2.13)$$

where  $\alpha(t)$  is the polarizability of the electron cloud. It is distance dependent and can be expressed as

$$\alpha(t) = \alpha_0 + \left( \frac{\partial \alpha}{\partial q} \right) \Big|_0 \cdot q(t) \quad (2.14)$$

In an ensemble of  $N$  “springs” the macroscopic polarization  $P(t)$  is given by

$$P(t) = N\mu(t) \quad (2.15)$$

With equations 2.11 to 2.14, it can be rewritten to

$$P(t) = N \cdot \left[ \alpha_0 + \left( \frac{\partial \alpha}{\partial q} \right) \Big|_0 \cdot q_0 \cos(\Omega t) \right] \cdot E_0 \cos(\omega_p t) \quad (2.16)$$

which contains three terms:

$$\begin{aligned} P(t) &= N \cdot \alpha_0 \cdot E_0 \cos(\omega_{ex} t) \\ &+ \frac{1}{2} N \cdot \left( \frac{\partial \alpha}{\partial q} \right) \Big|_0 \cdot E_0 q_0 \cdot \cos(\omega_{ex} + \Omega) t \\ &+ \frac{1}{2} N \cdot \left( \frac{\partial \alpha}{\partial q} \right) \Big|_0 \cdot E_0 q_0 \cdot \cos(\omega_{ex} - \Omega) t \end{aligned} \quad (2.17)$$

The first term represents Rayleigh scattering without a change in polarizability and no energy exchange. The last two terms describe Raman scattering with a frequency shift  $\pm\Omega$  compared to the incident light. It is important to mention that this inelastic scattering only occurs when the polarizability changes  $\left( \frac{\partial \alpha}{\partial q} \right) \Big|_0$ .

Finally, the intensity of scattered Raman photons is proportional number of molecules  $N$  as well as the intensity  $I_{ex}$  of the excitation source. Furthermore, it scales with the fourth power of the frequency  $\omega_{Raman}$  of the scattered light and with the square of the change of polarizability.

$$I_{Raman} \propto N \cdot I_{ex} \cdot \frac{\omega_{Raman}^4}{\Omega \left( 1 - e^{-\frac{\hbar\Omega}{kT}} \right)} \cdot \left( \frac{\partial \alpha}{\partial q} \right) \Big|_0^2 \quad (2.18)$$

The Raman signal can be enhanced when the frequency of the incident photon is close to the electronic transition of the material which will be discussed in the following for SRS.

### Stimulated Raman Scattering

Due to its very low cross section, spontaneous Raman scattering is a rare process resulting in longer acquisition times. As shown in Equation 2.18, the Raman intensity is proportional to the number of scatterers  $N$  as well as the laser intensity  $I_{ex}$  and can be increased when choosing higher concentrations and/or higher laser powers. However, high concentrations are often not suitable when it comes to the investigation of biochemical samples. This is also true for high laser powers since this applies photochemical stress on

the illuminated specimen. As briefly mentioned on page 11, several strategies to enhance the Raman signal have been developed. One technique is SRS, which is a third-order, non linear process. A detailed mathematical description of this mechanism is beyond the scope of this thesis but can be found in literature, e.g. (Bloembergen, 1967; Penzkofer, Laubereau, and Kaiser, 1979).

In brief, two pulsed laser sources are needed that fulfill the following requirements:

1. spatiotemporal overlap between both laser pulses in the specimen
2. match of samples's vibrational transition  $\Omega$  (see Equation 2.10) to the energy difference, i.e. the difference in frequency, between both laser pulses

With both requirements fulfilled, signal enhancement of up to eight orders of magnitude can be achieved. The mechanism during stimulated Raman scattering is depicted in a Jablonski diagram in figure 2.5. First, the pump and Stokes beam coherently excite the scattering material. The next pump beam then stimulates the material to emit a Stokes photon that is of the same frequency  $\omega_s$  as the Stokes laser pulse. When in resonance with the transition, energy is transferred from the pump beam through the material to the Stokes beam. This leads to an intensity increase of the Stokes beam, called Stimulated Raman Gain (SRG), and to an intensity decrease of the pump beam, termed Stimulated Raman Loss (SRL), shown in figure 2.6. With suitable instrumentation, i.e. beam modulation by an acousto-optic modulator (AOM) and a lock-in amplifier (LIA), the small energy differences in SRG or SRL can be detected by a photodiode. Here, the LIA is the core hardware component for the detection of the SRS signal. In brief, it receives two inputs: the acquired signal of the photodiode, which is a superimposition of the *Stokes* beam and SRG or SRL as well as the periodic signal of the AOM. The second input serves as the reference, allowing the LIA to filter the SRG or SRL component and amplify it (Tittel, Knechtel, and Ploetz, 2023). At this point, it is worth mentioning that SRS is a chemically sensitive and background free method due to the required frequency difference between both pulses to a vibrational transition  $\Omega$  of the sample.

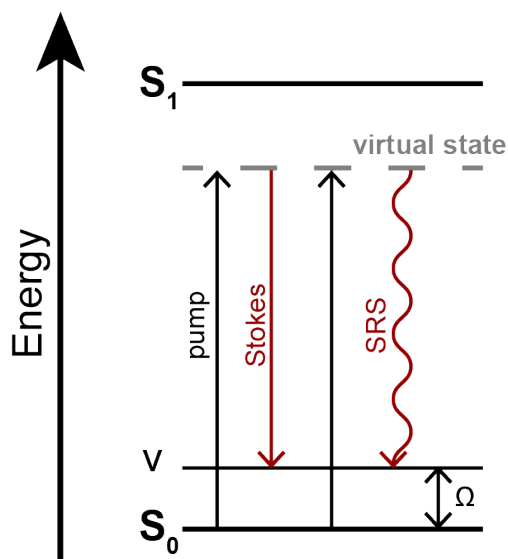


**Figure 2.5: Jablonski diagram illustrating SRS on the Stokes side.** Two spatiotemporally overlapping laser pulses (Pump and Stokes) that have a frequency shift matching a vibrational state  $\Omega$  of the scattering medium lead to coherent excitation of the material. This coherent excitation can be thought of as a transition from the vibrational ground state to an excited vibrational level via a virtual state. If the next pump pulse arrives, the system is stimulated to emit a Stokes photon (SRS).

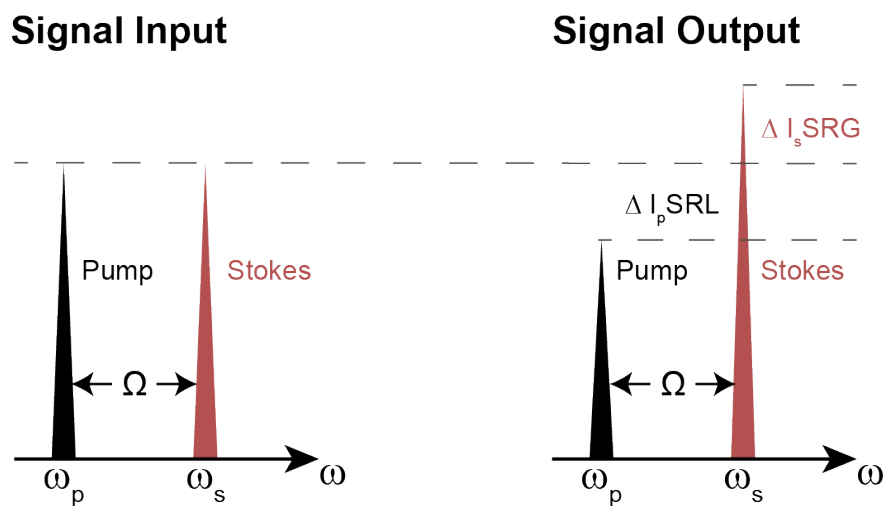


**Figure 2.6: Principles of SRL and SRG during SRS.** Energy is transferred from the pump pulse to the Stokes resulting in SRL in the intensity  $I_p$  of the pump beam and SRG in the intensity  $I_s$  of the Stokes beam.



## 2.2 Light Microscopy

With the discussion of the physical background of fluorescence and scattering of light in section 2.1, it is now worth having a closer look on the concepts of applications which make use of these phenomena. The basis for all applications is a light microscope, which can be grouped into three sections. Those are excitation source, sample illumination and signal detection. The beauty here is that various samples can be investigated by adjusting and harmonizing those three groups. This can range from a simple excitation source with continuous spectrum with a simple camera for taking magnified pictures of a sample to highly advanced excitation sources, such as (pulsed) lasers, that can be in synchronization with a photo-diode allowing for chemically sensitive imaging based on SRS or in combination with highly sensitive detectors, e.g. electron multiplying charge-coupled device (EMCCD) cameras or avalanche photodiodes (APDs), allowing for the detection of molecular interactions or the investigation of complex cellular mechanisms on the single molecule level. Imaging experiments on the single molecule level are often based on fluorescence, naming this field Fluorescence Microscopy. By integrating complex software in such instruments, it is today possible to develop customized microscopes. Such customization can range from automatized data acquisition procedures to highly specialized techniques as SPT.

This chapter will first discuss the physical limitation of optical microscopy followed by an “easy to implement” solution of circumventing this limitation. After the introduction of the diffraction limit and confocal microscopy, a subfield of fluorescence microscopy, single particle tracking (SPT), will be introduced. Here, the main focus will be set on 3D Orbital Tracking, a feedback based SPT technique allowing for tracking particles of interest on the fly.

### 2.2.1 The Diffraction Limit

Until recently, all light microscopes were intrinsically limited in their resolution. This means, if two point emitters are too close together, they cannot be distinguished anymore but appear as one emitter. In 1873, *Ernst Abbe* published his theoretical work on microscopes in which he could mathematically prove that the maximum resolution is given by

$$\Delta x = \frac{\lambda}{2NA} \quad (2.19)$$

where  $\lambda$  is the wavelength and  $NA$  the numerical aperture (Abbe, 1873). The numerical aperture is a dimensionless number that describes the goodness of resolution for an objective. It is defined as

$$NA = n \sin \alpha \quad (2.20)$$

with  $n$  being the refractive index between specimen and objective and  $\alpha$  the maximum half angle of the collected light. Today’s microscopes have reached this limit with a resolution of 200 nm–300 nm.

Methods have been developed to overcome the diffraction limit such as Stimulated Emission Depletion (STED) microscopy or photoactivated localization microscopy (PALM) as well as Stochastic Optical Reconstruction Microscopy (STORM) (Hell and Wichmann, 1994; Dickson et al., 1997; Betzig et al., 2006; Rust, Bates, and Zhuang, 2006). It is worth mentioning, that this breakthrough was awarded with the Nobel Prize in Chemistry in 2014 and has brought fluorescence microscopy to a new epoch known as *Nanoscopy*. However, a drawback of these methods is the requirement of static samples, i.e. biological samples such as cells need to be fixed. This means, their processes have to be suppressed. Methods that can also circumvent the diffraction limit is SPT techniques. The advantages here are, that those methods do not require static samples but are capable of tracking moving particles (on the fly) which will be discussed in greater detail in subsection 2.2.3. A lot of instruments are based on the confocal design which will be described in the following.

## 2.2.2 Confocal Microscopy

An “easy to implement” approach of circumventing the diffraction limit of light and hence increasing the resolution in images is the confocal design of a microscope. It was patented by *Marvin Minsky* in 1961 (Minsky, 1961). The difference between a classical microscope design is illustrated in figure 2.7.

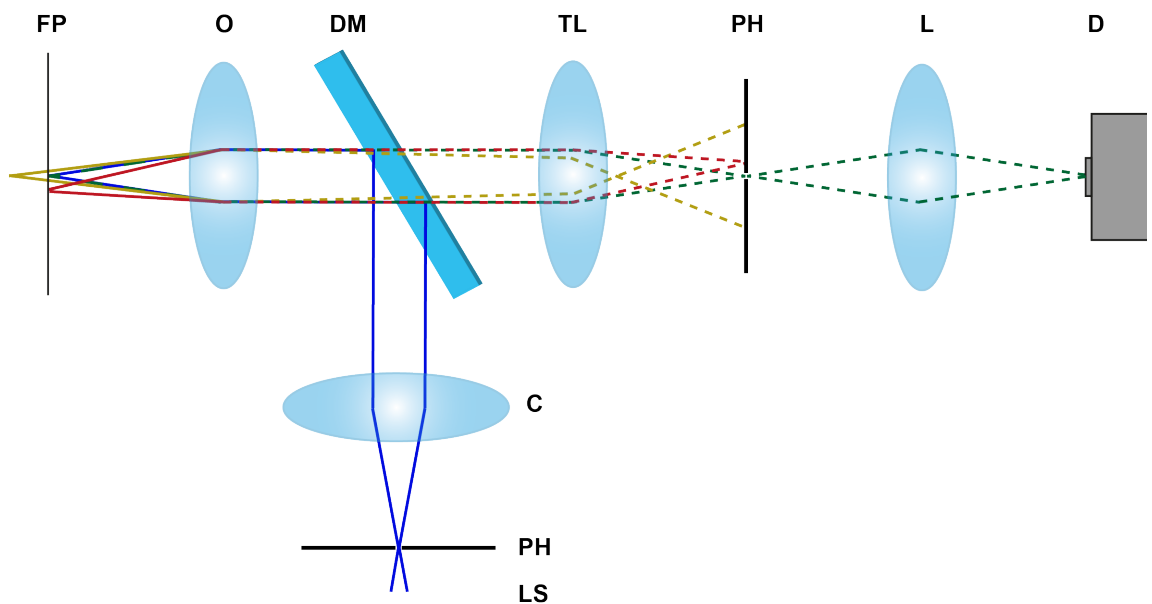


**Figure 2.7: Scheme of a confocal microscope.** C: collimator, D: point detector, DM: dichroic mirror, FP: focal plane, L: lens, LS: light source, O: objective, PH: pinhole, TL: tube lens, blue: excitation beam, green: fluorescence signal in focus, yellow: out of focal plane fluorescence, red: blocked fluorescence from focal plane.

*Minsky* introduced two pinholes (PH) which have to be in focus or *confocal* with the focal plane. In contrast to a “classic” design, which suffers from a low signal-to-noise

ratio (SNR) and blurry images due to photons emitted out of focus, the detection pinhole blocks these. However, due to the pinholes only a single point in the specimen and not an area is illuminated. To obtain an image, a certain area in the sample has to be scanned point by point. Compared to a wide field image, the resulting confocal image has a higher resolution, which is improved by a theoretical factor of  $\frac{1}{\sqrt{2}}$ . The definition of the diffraction limit in Equation 2.19 can be now rewritten as

$$\Delta x = \frac{0.37\lambda}{NA}. \quad (2.21)$$

Nowadays in a confocal microscope, the two pinholes are often replaced by two optical fibers. With this “easy to implement” improvement of resolution, confocal microscopes have become standard instrumentation in almost every microscopy laboratory.

### 2.2.3 Single Particle Tracking

With the concept of confocal microscopy introduced in the previous section, it is not only possible to obtain scans with higher resolution, but it can also be the basis for the development of highly advanced microscopy techniques such as single particle tracking (SPT). Due to the development of highly sensitive detectors and optical elements, it is state of the art to detect fluorescence on the single molecule level on surfaces or in solution. Molecules in solution are measured as they diffuse through the confocal volume yielding a burst of photons that are detected by single point detector such as APD or photomultiplier tube (PMT), as bursts (Kudryavtsev et al., 2012). With improved surface chemistry, molecules can also be immobilized on the surface and detected by a EMCCD camera (Elbert and Hubbell, 1996; Lamichhane et al., 2010; Szkop, Kliszcz, and Kasprzak, 2018). In both approaches the desired experiments are not carried out in bulk and the study of single molecule interactions can be performed on the nanometer scale (by using FRET) with high temporal resolution (Felekyan et al., 2005; Bartnik et al., 2020). This makes it possible to investigate processes that would not be observable in bulk. However, both methods have their drawbacks. In a classical burst experiment, the detection of a single molecule in the confocal volume is very short (on the orders of a millisecond). Hence, the investigation of processes of interest have to be carried out by collecting snapshots of many particles diffusing through the confocal volume. In a surface experiment, each particle can be detected on the order of minutes. However, due to the immobilization of the particle, its rotation can be hindered which could influence interaction processes. Furthermore, the time resolution of typical surface experiments is lower, which means that very fast processes on the microsecond timescale cannot be detected.

These drawbacks can be overcome by SPT approaches where the particle of interest free to diffuse is tracked over time in the specimen. In contrast to the approaches mentioned above, the particle trajectories make it possible to determine diffusion constants or velocities as well as to investigate possible interactions with the environment by analyzing the type of diffusion. Worth mentioning is the first SPT experiment carried out in 1971

by *Berg* (Berg, 1971). Here, the movement of *E.coli* bacteria in solution was detected using a feedback loop.

SPT methods can be split into two categories: *post processing* and *feedback based* SPT approaches. The nature of both groups is different from each other and will be discussed in greater detail on the following pages.

### Post Processing SPT

For the post processing approach, the typical workflow consists of two steps. First, the experiment is carried out and data is acquired. Generally, the data format is based on video which was recorded by a EMCCD camera. The second step is running an algorithm to detect particle movement and hence determine its trajectory. Examples of algorithms for such trajectory extraction are the nearest neighbor algorithm or maximum likelihood estimator (Mazzaferri et al., 2014; Enderlein, 1995). In case of very poor SNR, a wavelet analysis can be carried out to identify the particles before the extraction of trajectories (Olivo-Marin, 2002). The clear advantage of post processing approaches is the relatively high throughput withing one dataset. Since this type of SPT is mainly based on video recordings, high statistics due to the extraction of multiple particle trajectories from a single movie is possible. However, this advantage also comes along with a major drawback. In a standard installation, i.e. the imaging plane can not be shifted in z-dimension by an piezo, the camera can only detect particle movement within the focal plane. This means, the particle diffusion is restricted to be two dimensional (2D) (lateral diffusion). To the cost of time resolution, the third dimension can be accessed by recording z-stacks. Furthermore, trajectory extraction algorithms can suffer in localizing particles, when multiple trajectories cross each other. This can be reduced by pre-selecting a certain area in the video to be analyzed. Within the last years, several methods have been developed to overcome this “third dimension problem”. Examples are shown in figure 2.8 One technique is the so called defocused imaging. Here, the diffraction pattern which is dependent on the axial position of the particle is used for determining the axial position of the particle. An example is published by *Speidel et al* (Speidel, Jonáš, and Florin, 2003). A second approach is point spread function (PSF) engineering introduced by *Moerner* (Pavani et al., 2009). In general, a phase plate or a spatial light modulator is implemented in the Fourier plane of the microscope modulating the phase of the excitation beam. In *Moerner’s* case, this creates a double helix of the PSF. A particle is then no longer imaged by a single Gaussian intensity spot, but by two. The center of mass of both spots encodes the the lateral position of the particle. The axial position is encoded in the relative orientation of the spots within the field of view. *Shechtman et al.* took this idea and pushed it further by introducing the Tetrapod increasing the axial detection range (Shechtman et al., 2015).

It is worth mentioning that intensive research in this field has made it possible to specifically design phase plates and optimize data analysis for each experiments by using artificial intelligence (Nehme et al., 2020).

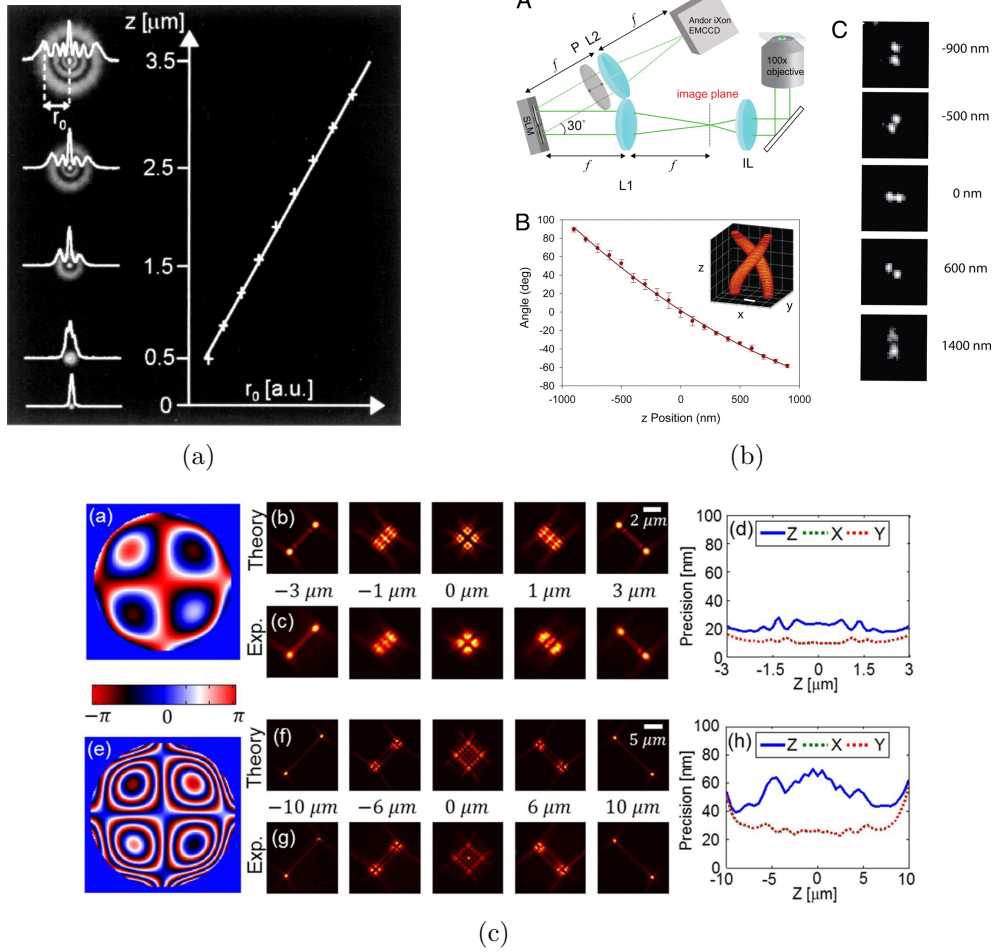


**Figure 2.8: Overview of SPT techniques using the post processing approach.** (a) Off-focus imaging by *Speidel, et al.* Depending on the size of the diffraction pattern, the particle can be localized in all three dimensions. (b) Double-Helix PSF by *Pavani, et al.*. By changing the shape of the PSF using a phase mask, the 3D position of the particle is encoded in the detected shape of the fluorescent signal. The lateral position of particle can be extracted by calculating the center of mass of the fluorescent spots. The axial position is directly read from the relative orientation of one fluorescent pair withing the FOV. (c) *Shechtman* improved this technique introducing the Tetrapod. With this, he could increase the axial detection range that is covered by the engineered PSF. Adapted from (*Speidel, Jonáš, and Florin, 2003; Pavani et al., 2009*) and (*Shechtman et al., 2015*).

### Feedback Based SPT

As already mentioned, *Berg* published the first SPT instrument in 1971 using a feedback based approach (Berg, 1971). The original sketch of the microscope is illustrated in figure 2.9. Light reflected by bacteria floating around in a sample holder was collected by three fiber pairs and detected by photomultipliers connected to each fiber. The pairs were aligned to span the axes of a 3D coordinate system. By comparing the measured intensities of two corresponding detectors, the particle movement along an axis could be extracted. All signals were fed into an electromechanical transducer for repositioning the sample holder. Hence, the 3D movement of *E.coli* was tracked on the fly.

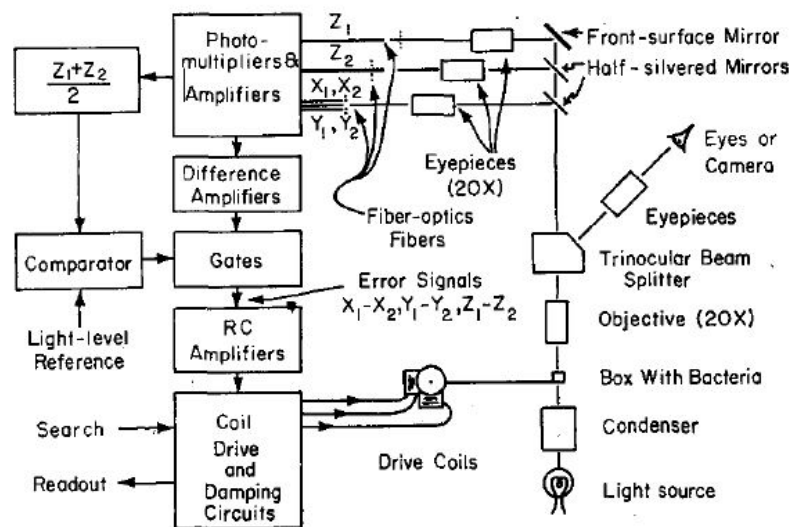


**Figure 2.9: Instrumentation of the first feedback based SPT setup by *Berg*.** Three pairs of fibers span a 3D volume in which the reflected light of a bacterium is detected. By comparing the detected intensities of a corresponding detector pair, the diffusion along this axis can be determined. The signal of all three axes str read in into a electromechanical transducer, which was repositions the sample holder. Adapted from (Berg, 1971).

With this technique, *Berg* pioneered feedback based SPT pointing out the two major steps that are still necessary today:

- position determination of the particle of interested
- repositioning the apparatus to the last known coordinates

With improving technology and more sensitive detectors, feedback based SPT has also emerged in fluorescence microscopy. Generally, these approaches can be divided into two types:

1. spanning the detection volume
2. beam steering

In the first type, several detectors are aligned to span a 2D area or a 3D volume. Prominent examples are the Tetrahedral tracking published by *Werner et al.*, the TSUNAMI approach by *Perillo et al.* or PIE-MINFLUX described by *Masullo et al.* illustrated in figure 2.10 (Lessard, Goodwin, and Werner, 2007; Perillo et al., 2015; Masullo et al., 2021). In the Tetrahedral tracking, two fiber pairs are aligned in a way that they span a tetrahedron. Analogous to *Berg*, each detector pair encodes the particle movement along one coordinate axis. The axial position of the particle can be extracted by comparing the intensities of both pairs against each other.

Similarly to *Werner's* method, the TSUNAMI instrument also uses tetrahedral geometry but for excitation. The excitation source is a pulsed light amplification by stimulated emission of radiation (laser). The pulses for each excitation volume are delayed by 3.3 ns. Using TCSPC electronics for detection, each photon can be assigned to the corresponding excitation volume. Hence, in addition to the position information of the particle, the lifetime information of the fluorescent species is also accessible. This approach was recently extended to a second detection channel (Liu et al., 2020).

A pulsed laser source is also used in PIE-MINFLUX. Here, the laser pulse is split and coupled into four fibers of different lengths delaying each beam. The four fibers are adjusted to span a 2D excitation pattern. Using TCSPC detection, the photons can be assigned to the corresponding excitation volume, and the lifetime information of the fluorescent species is accessible. With a sophisticated localization algorithm, the particle can be localized with very high accuracy.

For the second approach, the excitation beam is moved with a defined pattern to probe a certain area for the presence of the particle of interest. Examples for SPT approaches based on beam steering are the first attempt of MINFLUX by *Balzarotti et al.* or the 3D-DyPLOT by *Hou et al.*, both published in 2017 (Balzarotti et al., 2017; Hou, Lang, and Welsher, 2017). A third technique is the Orbital Tracking approach first described by *Enderlein* in 2000 and realized by *Kis-Petikova and Gratton* in 2004 (Enderlein, 2000; Kis-Petikova and Gratton, 2004). The concepts of these approaches are illustrated in figure 2.11. In contrast to PIE-MINFLUX, the approach from *Hell* uses continuous wave (cw) laser excitation. Furthermore, the excitation pattern is not defined by aligned fibers, but the beam is steered using electro-optical deflectors (EODs) generating the same pattern.

In 3D-DyPLOT, an EOD is used for steering the beam covering a  $1\ \mu\text{m} \times 1\ \mu\text{m}$  area. This area is scanned using the knight's tour pattern. To obtain information from the third dimension, a tunable acoustic gradient (TAG) lens is used for performing a fast z-stack covering a range of  $4\ \mu\text{m}$ .

In Orbital Tracking (figure 2.11(c)), the the excitation beam is rotated in a circular pattern, generating an orbit, using galvanometer driven mirrors. Axial information is obtained by either scanning in different positions or detecting the signal in two different planes. The Orbital Tracking approach will be discussed in greater detail on the following pages.

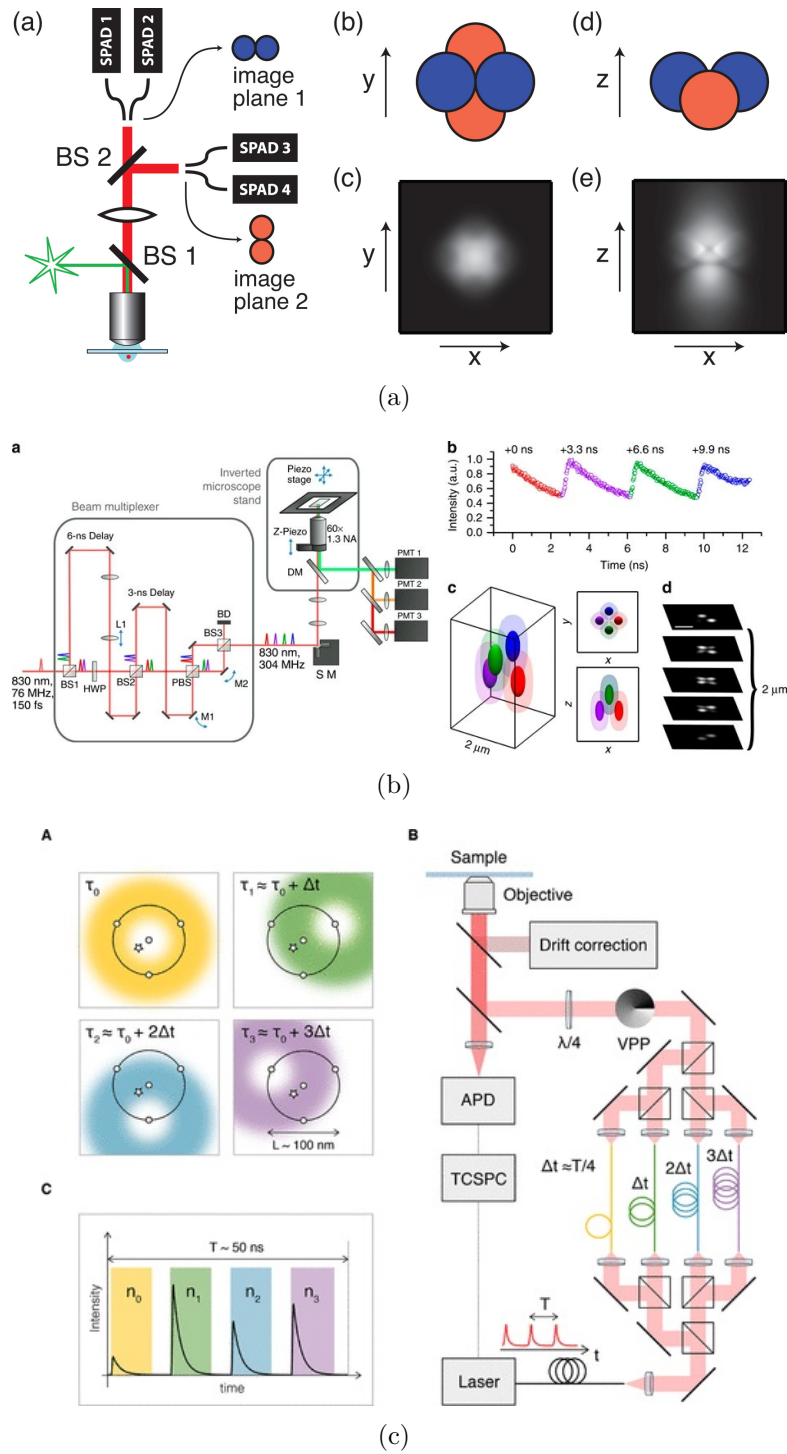
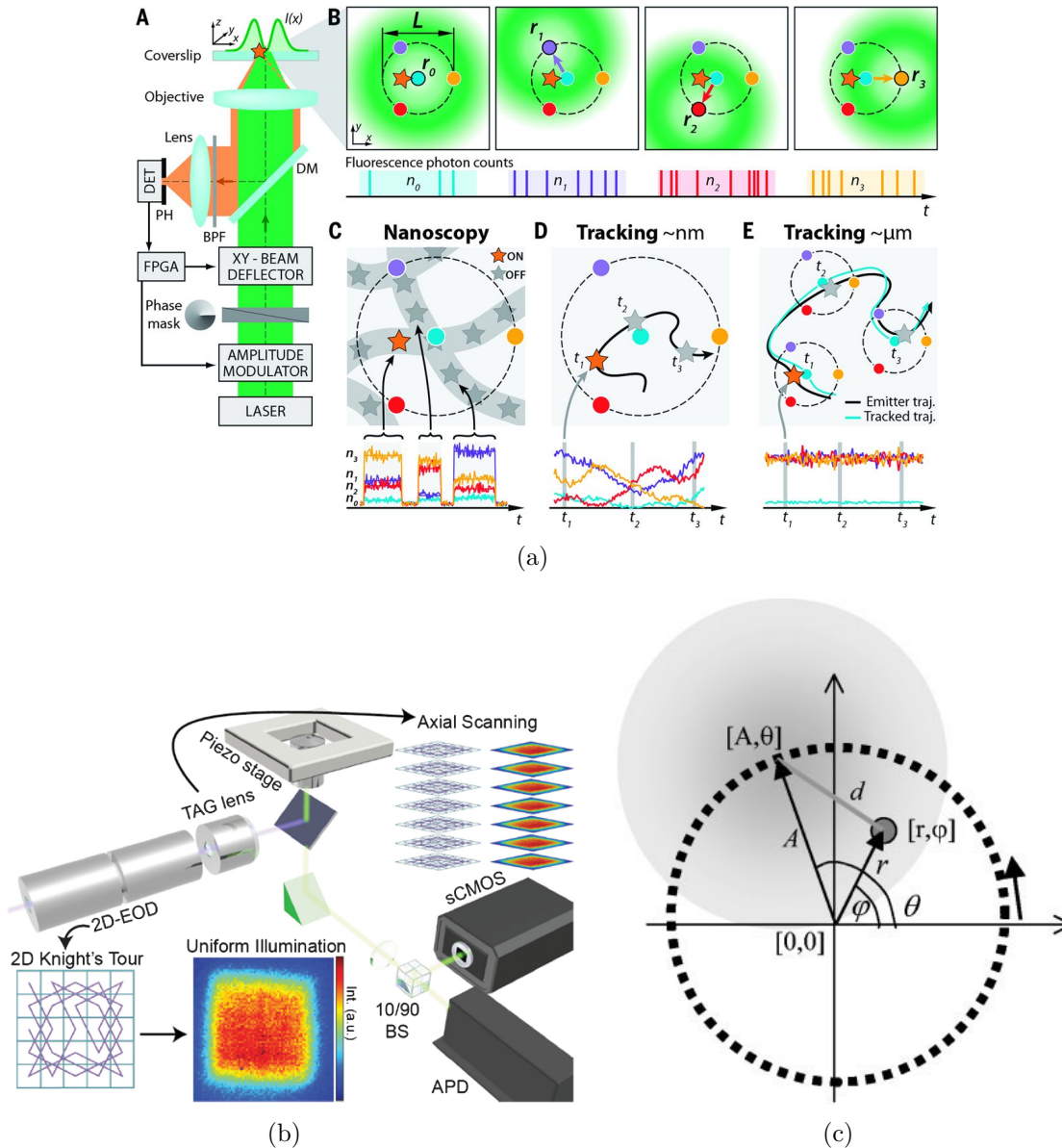


**Figure 2.10: Overview of feedback based SPT approaches spanning the detection volume for localizing the particle of interest** (a) Tetrahedral tracking by *Lessard et al.* Inspired by *Berg's work*, two fiber pairs aligned in tetrahedral geometry are used to localize the particle within the detection volume. (b) Similar to PIE-MINFLUX and tetrahedral tracking, the TSUNAMI approach by *Perillo et al.* probes four distinct areas in 3D for the particle position. (c) PIE-MINFLUX published by *Masullo et al.* using four donut pulses to determine the particle position within the probed area. Adapted from (*Lessard, Goodwin, and Werner, 2007; Perillo et al., 2015*) and (*Masullo et al., 2021*).





(a)

(b)

(c)

**Figure 2.11: Overview of feedback based SPT approaches that steer the excitation beam.**

(a) MINFLUX approach by *Balzarotti et al.* With EODs, the excitation beam is moved to four distinct positions in the scanning area. The position of the particle can be determined from the detected intensities of each probing position. (b) 3D-DyPLOT by *Hou et al.* A  $1\ \mu\text{m}$  by  $1\ \mu\text{m}$  area is scanned in the knight's tour pattern using an EOD. Axial information of the particle movement is obtained by scanning a z-stack (c) Orbital Tracking approach by *Kis-Petikova and Gratton*. The excitation beam is rotated in a circular shape around the particle by galvanometer mirrors generating an orbit. The particle position within the orbit is encoded in the detected fluorescent signal during one orbit. Adapted from (Balzarotti et al., 2017; Hou, Lang, and Welscher, 2017) and (Kis-Petikova and Gratton, 2004).

### 2.2.4 3D Orbital Tracking Microscopy

As mentioned in the previous section, one feedback based SPT technique is the Orbital Tracking approach, which was theoretically proposed first for lateral diffusion of molecules within a 2D membrane by Enderlein (2000). In brief, this technique is based on a confocal microscope in which the excitation laser beam is rotated in a circle generating an orbit around the particle to be tracked. The particle position within the orbit is directly encoded in the modulation of the detected signal as illustrated in figure 2.12. The intensity of the maximum of the modulation encodes the distance of the particle from the orbit center. The angular position of the particle in the orbit can directly be read from the phase of the modulation, i.e. the position of the detected maximum with respect to the orbit position.

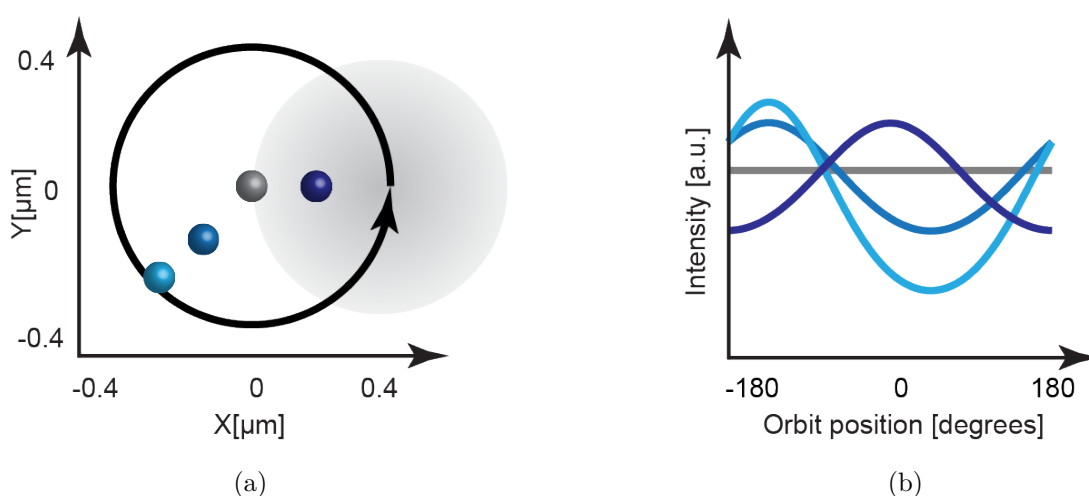


**Figure 2.12: A simulation of the signal coming from a fluorescent particle for different positions in the orbit.** (a) Scheme of different particle positions (filled grey and blue spheres) within one orbit (thick circle). The arrow defines the direction of rotation of the PSF (transparent grey circle) and starting position of the orbit. (b) Corresponding detected signals (same color coding) of the particles plotted against the orbit position. The position of the amplitude encodes the angular position of the particle within the orbit. The distance of the particle from the orbit center is obtained from the intensity.

The first practical realization of this approach was published by *Levi et al.* in which they could successfully track the 3D motion of a 500 nm sized sphere in agarose gel (Levi et al., 2003). The axial information was accessible by moving the z-position of the objective by a piezoelectric-nanopositioner. The axial position information was obtained by alternating the orbit scan symmetrically above and below the last known position of the particle. In this approach, the time critical factor for acquiring 3D trajectories of moving particles is the response time of the nanopositioner, which is on the order of kHz, as well as the scanning cycle for both planes. Since the internal response of a piezoelectric device is slower compared to galvanometer driven system, the alternation rate between the z-planes is a multiple  $n$  of the orbit time. The acquisition speed of the

instrument could be increased by exchanging the nanopositioner by an electrical tunable lens (Annibale, Dvornikov, and Gratton, 2015). *Katayama et al.* could overcome this problem by scanning in the focal plane but simultaneously detecting the signal above and below the focal plane using two detectors that were slightly misaligned spanning symmetric 3D detection volume covering the focal plane (Katayama et al., 2009).

## Theory

### Lateral Localization

In general, two possibilities for determining the particle position within the orbit exist. The first one is by a fitting based algorithm in which the position is geometrically fitted from the intensity distribution detected during an orbit. Since this approach is fairly time consuming, the particle diffusion should be slower than the orbit time. As demonstrated, the detected fluorescent signal is periodic. Hence, the particle position can also be obtained by calculating a fast Fourier transformation (FFT) of the fluorescence signal (Berland, So, and Gratton, 1995; Kis-Petikova and Gratton, 2004).

### Fitting Based Approach

Assuming an immobilized or a slowly diffusing particle on a surface, i.e. the motion of the particle is on a time scale slower than the orbit rotation, the particle position during one orbit can be estimated as constant. In this case, scanning is performed in the same plane and the axial position does not change. The fluorescent intensity  $I(d)$  of the particle with respect to the position of the PSF can then be described with an 2D *Gaussian* model

$$I(d) = I_0 e^{-\left(\frac{2d^2}{w_0^2}\right)} \quad (2.22)$$

where  $I_0$  is the maximum fluorescent intensity,  $w_0$  the beam waist and  $d^2$  the square of the distance between the center of the PSF and the center of the particle position as illustrated in figure 2.13. In cartesian coordinates, the distance  $d$  is calculated as follows

$$d = \sqrt{(X - x)^2 + (Y - y)^2} \quad (2.23)$$

with  $(X,Y)$  being the coordinates the PSF and  $(x,y)$  of the particle. Since the excitation beam is rotated in a circle, it is convenient to transform from cartesian into polar coordinates with

$$r = \sqrt{(x)^2 + (y)^2} \quad (2.24)$$

and

$$R = \sqrt{(X)^2 + (Y)^2} \quad (2.25)$$

for the distances of the particle and the PSF to the center of the orbit (origin of coordinate system at  $[0,0]$ ). The corresponding angular positions can be calculated as

$$\varphi = \arccos\left(\frac{x}{r}\right) \quad (2.26)$$

and

$$\Theta = \arccos\left(\frac{X}{R}\right) \quad (2.27)$$

where  $\Theta$  encodes the rotation frequency of the orbit described as  $\Theta = 2\pi ft$ .

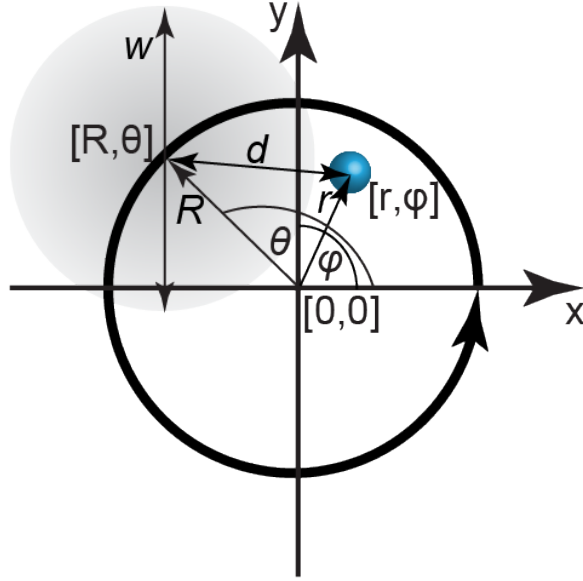


**Figure 2.13: Schematic for position determination of a particle (blue) in polar coordinates during an orbit.** The detected signal varies for every position of the PSF (grey) during the orbit.

With Equations 2.24 to 2.27, Equation 2.23 can be rewritten as

$$d = \sqrt{r^2 + R^2 - 2rR \cos(\Theta - \varphi)}. \quad (2.28)$$

With this, Equation 2.22 can now be expressed as

$$I(\Theta) = I_0 e^{-\left[\frac{2(r^2 + R^2 - 2rR \cos(\Theta - \varphi))}{w_0}\right]} \quad (2.29)$$

where the beam waist  $w_0$ , the maximum intensity  $I_0$  as well as the coordinates  $[R, \Theta]$  of the PSF are known. Hence by fitting the detected fluorescent signal to Equation 2.29, the particle position within the orbit can be determined which was demonstrated on immobilized particles (Kis-Petikova and Gratton, 2004). However, fitting algorithms are time critical operations and several iterations are needed to obtain reasonable results. Hence, this position determination approach is not practical for real time applications.

### Fast Fourier Transformation Based Approach

Since the fluorescent signal during one orbit rotation is periodic, it is further possible to extract the particle position by a *Fourier* analysis of the intensity. With the *Fourier* transform, any time dependent signal  $f(t)$  can be represented in frequency space  $F(\omega)$ .

$$F(\omega) = \frac{1}{\sqrt{2\pi}} \int_{-\infty}^{\infty} f(t) e^{-i\omega t} dt \quad (2.30)$$

Vice versa, any periodic signal  $F(\omega)$  from the frequency space can be displayed in the time domain.

$$f(t) = \frac{1}{\sqrt{2\pi}} \int_{-\infty}^{\infty} F(\omega) e^{i\omega t} d\omega \quad (2.31)$$

For discrete signals, the integral in Equation 2.31 can be solved by a *Fourier* series

$$f(t) = \frac{a_0}{2} + \sum_{k=1}^{\infty} (a_k \cos(kt) + b_k \sin(kt)) \quad (2.32)$$

where  $a_k$  and  $b_k$  are the *Fourier* coefficients (Fourier, 1822). In 1965, an efficient algorithm for calculating the *Fourier* series in processors was published (Cooley and Tukey, 1965). With the fluorescent signal  $I(R, \Theta)$  detected during one orbit, the particle position can now be determined from the corresponding *Fourier* series

$$I(R, \Theta) = \frac{a_0(R)}{2} + \sum_{k=1}^{\infty} (a_k(R) \cos(k\Theta) + b_k(R) \sin(k\Theta)) \quad (2.33)$$

by analyzing its *Fourier* coefficients. The average intensity is encoded in the zeroth order coefficient  $a_0$ . The particle position in the orbit can be obtained from  $a_1$  and  $b_1$ . A summary is listed in table 2.1.

**Table 2.1:** Characteristics of the *Fourier* coefficients for the Orbital Tracking approach.

<i>Fourier</i> Coefficients	Amplitude	Phase
$a_0$	average countrate during one orbit	-
$a_1$ & $b_1$	distance to the orbit center	angular position in orbit

In reality, the maximum signal intensity  $I_0$  can vary for different orders of magnitude. Hence, the calculated modulation (Equation 2.34) has to be normalized to obtain reasonable values.

$$Mod = \frac{\sqrt{a_1^2 + b_1^2}}{0.5a_0} \quad (2.34)$$

The angular and radial coordinates  $[\varphi, r]$  are calculated from

$$\varphi = \arctan \frac{b_1}{a_1} \quad (2.35)$$

and

$$r = f(R, w_0) \cdot Mod \quad (2.36)$$

where  $f(R, w_0)$  is a calibration function that converts the modulation into real distances. This scaling function depends on the orbit radius  $R$  and beam waist  $w_0$  and can be determined experimentally. To reduce computational workload during tracking experiments, this function is incorporated in the tracking feedback loop as a look-up table (LUT). After the calculation of the modulation, the corresponding distance can be read from the LUT by applying a binary search algorithm, making the values accessible on the fly.

### Axial Localization

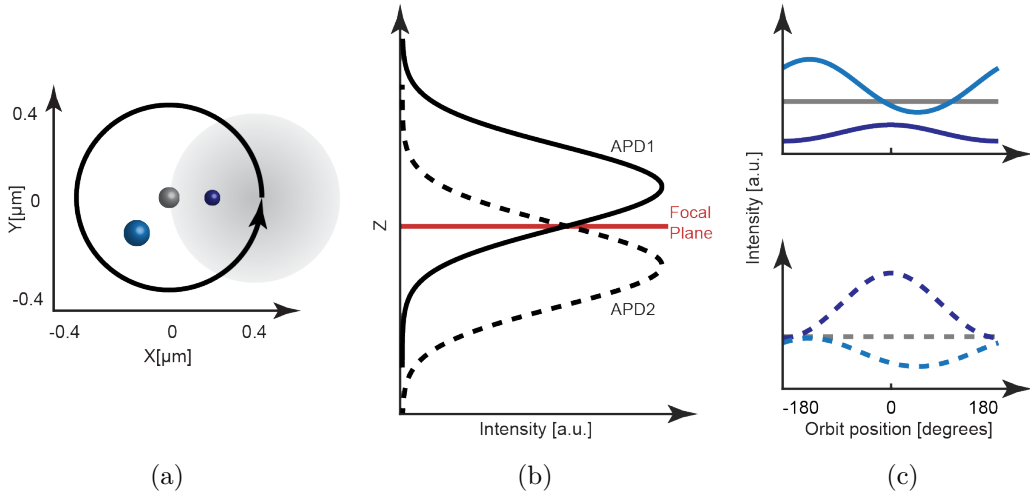


**Figure 2.14: 3D particle localization by Orbital Tracking.** (a) 2D projection onto the focal plane of particle positions (small spheres) in the orbit. The PSF of a focused beam (transparent gray circle) is rotated probing the fluorescence signal of the particle. The gray particle is placed in the focal plane, the light blue above and the dark blue one below the focal plane. (b) By shifting the detection maxima of two APDs symmetrically out of the focal plane, a 3D detection volume is generated. (c) The modulated signal during one orbit is now collected by two APDs. The amplitude of the modulated signal is dependent on the axial position of the particle within the generated 3D detection volume without influencing the phase. For obtaining a higher accuracy in lateral position determination, it is convenient to calculate the position within the orbit by the sum of both detectors. However, due to the axial position dependence of the fluorescence signal, the particle position is now directly encoded in the signal ratio of both detectors and can be calculated with Equation 2.37.

The described approach on page 27 does not include axial information. To obtain localization in the third dimension, one possibility is to detect the fluorescence collected after two pinholes that are symmetrically misaligned above and below the focal plane. This spans a detection volume covering the excitation plane, hence splitting the fluorescence signal between two detectors as illustrated in figure 2.14. The distance of the parti-

cle with respect to the focal plane can directly be accessed by comparing the detected intensities of both detectors

$$d_z = f(d_{planes}, \omega_z) \frac{I_1 - I_2}{I_1 + I_2} \quad (2.37)$$

where  $f(d_{planes}, \omega_z)$  is a calibration function. It depends on the axial beam waist  $\omega_z$  and the distance of  $d_{planes}$  of both detection planes. Analogous to the scaling function for lateral position determination described on Equation 2.36, this scaling function is also incorporated into the feedback algorithm as a LUT. Compared to the Orbital Tracking approach of Levi et al. (2003) and the improvement by introducing an electrical tunable lens by Annibale, Dvornikov, and Gratton (2015), the big advantage of a feedback algorithm based on LUT is the immediate access of the particle's z-position after one orbit.

### Orbital Tracking Setup

A sketch of the configuration of the Orbital Tracking microscope used throughout this thesis is illustrated in figure 2.15. Detailed information is given in the corresponding publication A.2. In brief, four laser lines are controlled electronically by two acousto-optic tunable filters (AOTFs) and split by a 70:30 beam splitter (BS) before coupled into two single mode fibers, each equipped with an collimator (Schäffter & Kirchhoff) at the fiber output, respectively. One excitation beam path is then widened by a telescope consisting of 50 mm and 180 mm lenses and guided into a 60x water objective, which is mounted in the epi-direction on a piezo-nanopositioner for the wide field modality (green box). The second beam path is guided through galvanometer driven systems into the same objective. With these galvanometer driven mirrors, confocal scans and orbit rotations are carried out. After passing the laser combining dichroic mirror (DM), the fluorescence signal is guided into the detection path of the confocal modality. This is grouped into two detection channels each consisting of a pair of APDs. A long pass filter separates fluorescence arising from 488 nm excitation and guides the emitted photons into the first detection channel (blue box). A 50:50 BS is divides the signal before each of both beams is focused into a multimode fiber connected to an APDs, respectively. For the second detection channel, two configurations are possible. Due to the flexible design of the second detection channel (yellow to red faded box), it can be aligned for carrying out dual color tracking experiments or multicolor tracking experiments i.e. tracking with simultaneous FRET detection. For dual color experiments, the second channel as the same geometry as detection channel 1. For multicolor experiments, the BS is replaced by a DM. In this configuration, detection channel 2 acts as the FRET channel while tracking is executed in channel 1. Software implementation on the microscope and key results of this novel modality will be discussed in the following chapter.

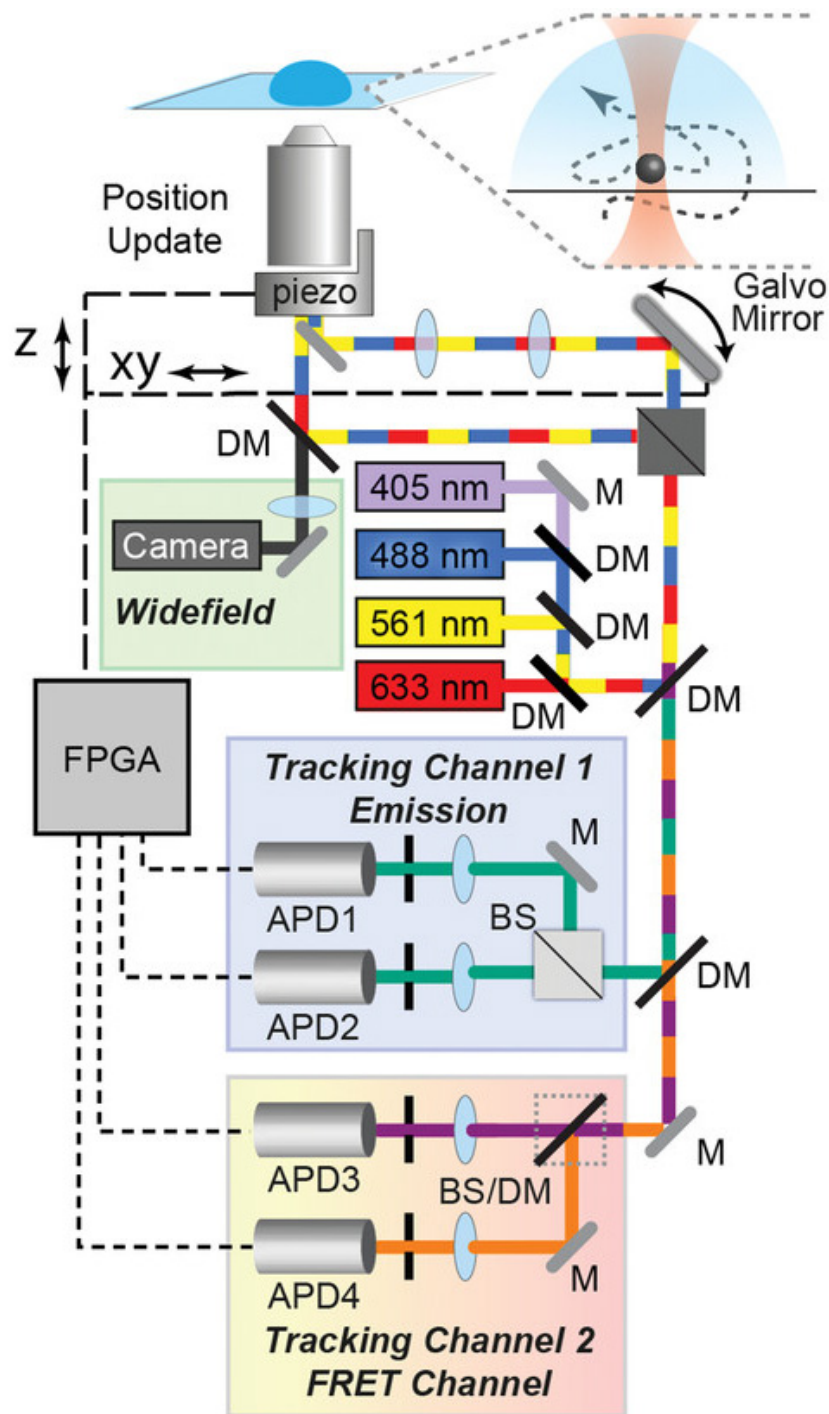


**Figure 2.15:** Sketch of the Multicolor 3D Orbital Tracking instrument used for this thesis.

After passing a beam splitter, four laser lines are guided by a dichroic mirror onto a 2-axes galvo mirror system. Here, the 405 nm laser serves for photoactivation. The galvo system rotates the beams and reflects them into the objective which is mounted on a piezo-nanopositioner. The emitted photons from the specimen are collected by the objective and split on two detection channels by a long-pass filter. Depending on the experiment, the signal in each channel is either separated by a 50:50 beam splitter or by a dichroic mirror. Furthermore, the three laser lines (488–633 nm) are reflected into a wide-field geometry. Together with the EMCCD camera, they build up the wide-field modality of the instrument that can be used for parallel imaging of the surrounding, while tracking a particle. APD: avalanche photodiode; BS: beam splitter; DM: dichroic mirror; FPGA: field-programmable gate array; M: mirror.



## Chapter 3

---

# Trajectory data of antero- and retrograde movement of mitochondria in living zebrafish larvae

As described in subsection 2.2.4, Orbital Tracking is a feedback based SPT technique. Nowadays, those approaches provide highly accurate 3D trajectories of moving targets allowing for a very detailed analysis of the particle of interest. With the increase of obtained information in feedback based SPT approaches, the data files become more and more complex, making the documentation of the data structure an important topic. This gains even more weight when data is publicly accessible, which is a currently a trend towards *open science*. With this accessibility and documentation of several data structures, a standard might be established in the SPT community in future. The first part in the given chapter will provide a description of the data structure of the 3D Orbital Tracking instrument. Next, a correlation analysis will be applied on example data of moving mitochondria in living zebra fish larvae. With this correlation approach, it is possible to robustly distinguish between active and passive transport states, which are not accessible by camera based approaches.

### 3.1 Structure of Orbital Tracking Data File

The information contained in the data file during an Orbital Tracking experiment is highly detailed. Several parameters are stored including the particle coordinates or activation of the tracking algorithm. All the acquired data is written into a .txt file on the hard drive for later analysis. An overview of the general file structure is listed in table 3.1. In general, it consists of two parts: a file header and individual data points. The file header stores meta data regarding the executed experiment. This includes the time stamp, the selected orbit time and radius, the tracking threshold defining when tracking is executed or the search algorithm is started and the number of delay orbits in which the excitation laser is switched off and no particle detection is performed. Furthermore, the *Number of Particle* row stores information regarding the number of active detection channels. The *Long Range* entry indicates whether data was acquired in long range tracking mode or not. Finally, the threshold for repositioning the sample on the xy-stage is provided by the *Long Range Threshold*. The file header is followed by the data section. All data acquired during an experiment is stored in eleven columns in

total. Each row of this table corresponds to one orbit rotation. The first five columns contain particle as well as orbit information. The calculated particle coordinates after each orbit for x, y and z are stored in columns 1 to 3, respectively. The corresponding number of executed orbit and its time are written in columns 4 and 5. It is worth mentioning that the orbit time takes delay orbits into account. Columns 6 and 7 provide the detected signal after an orbit rotation of the detector pair. In case a wide-field video is recorded during tracking, the camera frame corresponding to the executed orbit is saved in column 8. This is followed by the indication whether the tracking or search algorithm was engaged (Column 9). Finally, the last two columns store information if the sample was repositioned during a long range tracking experiment.

## 3.2 Correlation Analysis

With the provided high resolution data described in the previous section, the trajectories of mitochondriae in living zebra fish larvae can be analyzed to identify active and passive states during moving. The high number of data points makes a classical mean squared displacement (MSD) approach not applicable due to statistical degeneration along the curve and the lack of identifying local changes in particle behavior. Furthermore, the type of motion that is determined by the factor  $\alpha$  is spoiled with uncertainties. Thresholds of this factor for distinguishing different types of diffusion can not experimentally be determined and vary for different conditions. Hence, a new correlation approach was developed (Wehnekamp et al., 2019). Here, a sliding window is moved over the trajectory, resulting in a correlation carpet

$$Cor(t, \tau) = \frac{1}{n - \tau} \sum_{i=t}^{t+\tau_{max}-\tau} \phi(i)\phi(i + \tau) \quad (3.1)$$

where  $t$  is the orbit time,  $\tau$  the correlation lag time,  $n$  the number of data points,  $\tau_{max}$  the size of the correlation window and  $\phi$  the angle between two orbits along the trajectory. The beauty of this approach is that the threshold separating both states is not gestimated but can be calculated for each trajectory individually. For this, the correlation is repeated for randomized angles  $\phi_{rand}$  along the trajectory obtaining  $Cor_{rand}$ . Taking the mean and standard deviation of  $Cor_{rand}$  into account, the threshold  $T$  can be determined by searching for correlation amplitudes which deviate  $w$  (weighting factor) times from the standard deviation using following equation.

$$T = M(Cor_{rand}) + w \cdot \sigma(Cor_{rand}) \quad (3.2)$$

Here,  $M$  is the mean value for a given set of  $Cor_{rand}$  and  $\sigma$  the corresponding standard deviation.

**Table 3.1:** Structure of Orbital Tracking data file including file header and data entries.

	Entry/Column Number	Description
<b>File Header</b>	File Path	original file path of raw data
	Date	date of data acquisition
	Time	time stamp of start
	Orbit Time [ms]	user defined orbit time
	Orbit Radius [V]	user defined orbit radius
	Tracking Threshold [Hz]	intensity limit for executing tracking or search algorithm
	Delay Orbits	number of dark orbits
	Number of Particles	number of active detection channels during the experiment (1: single color mode; 2: dual color mode)
	Long Range	information regarding long range tracking mode (0: disabled; 1: activated)
	Long Range Threshold [V]	user defined threshold for automated repositioning of stage
<b>Data</b>	1 - 3	particle coordinates (x,y,z)
	4	orbit number
	5	calculated orbit time (including delay orbits and long-range tracking events)
	6 & 7	total detected signal of each detector during the given orbit
	8	camera frame for the wide-field detection
	9	tracking (0: inactive; 1: active)
	10 & 11	repositioning information for activated long-range tracking for x (column 10) and y (column 11) axis (0: no repositioning; 1: repositioning of sample)

### 3.3 Key Results

The impact of a chosen set of parameters on the calculations is summarized in figure 3.1. The calculations were carried out on subregion of the same mitochondrial retrograde trajectory (zoom in panel (a)). Panel (b) illustrates the correlation carpets calculated for three different sliding windows ( $\tau_{max} = [32, 64, 128]$ ). As expected, the noise is more dominant for smaller sliding windows. The influence of the weighting factor  $w$  on the calculation of the threshold  $T$  is depicted in upper half of panel (c). For bigger values of  $w$ , the threshold shifts to higher limits, influencing the detection of moving and stationary phases. This is illustrated in the lower half of panel (c) in which the zoomed fraction of the analyzed trajectory is colorized for both states. Here, red areas represent stationary and green areas directed motion. It may be argued, that this threshold can be actively moved to preferred values by choosing the weighting factor accordingly. However, with this approach, the threshold between both phases is standardized for each individual trajectory allowing for better statistical analysis and comparison.

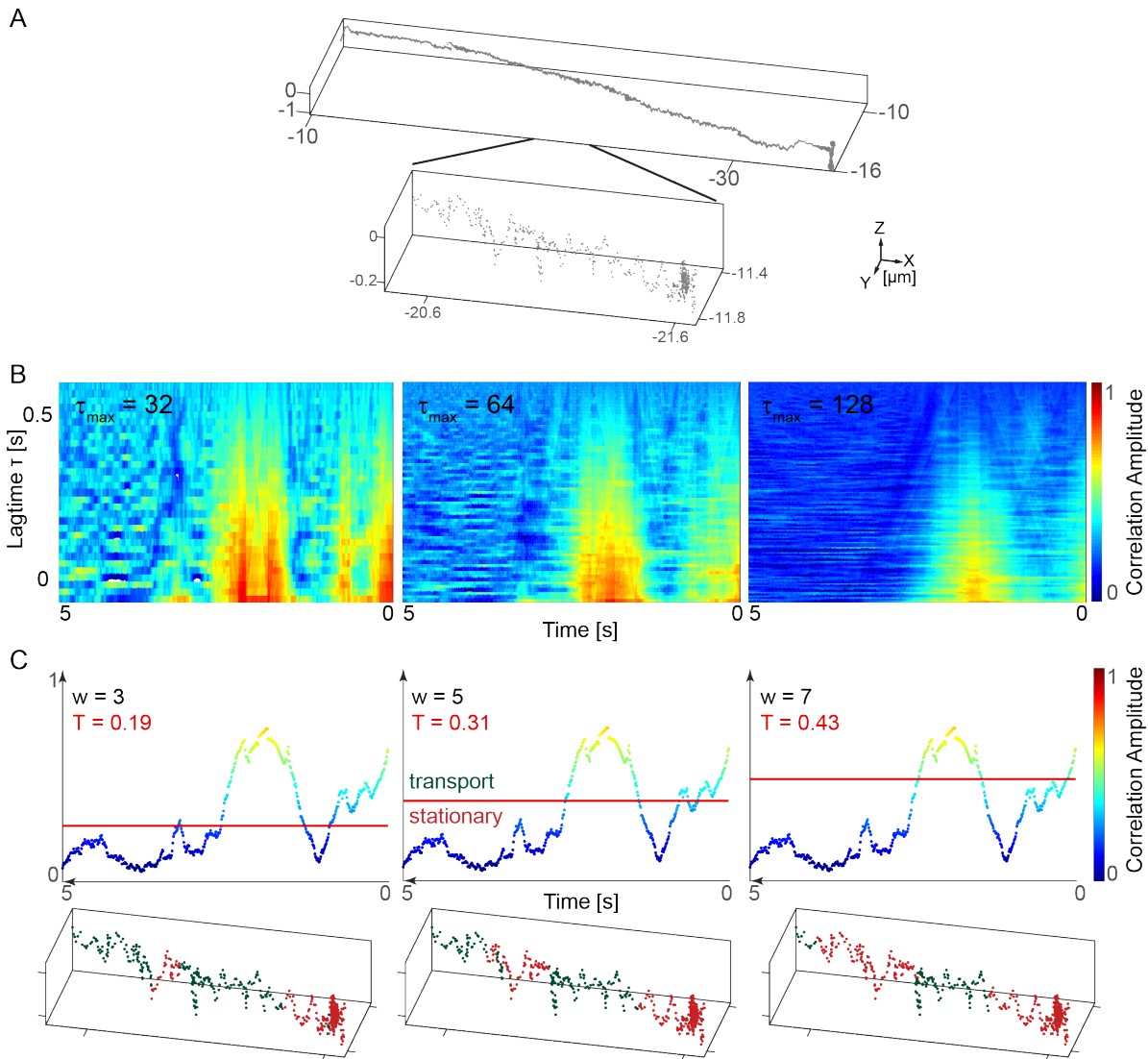


**Figure 3.1: Correlation analysis of a mitochondrial retrograde trajectory.** (a) An example trajectory and zoom in of a moving mitochondrion in the retrograde direction with a time resolution of 100 Hz. (b) Correlation carpets of the lateral angles  $\phi(t)$  between consecutive orbits with different sliding windows  $\tau_{\text{max}}$ . (c) The correlation amplitude determined from the sum of the correlation function over a sliding window of 64 data points is plotted. Three different weighting factors corresponding to thresholds of 3, 5, and 7 times the standard deviation of the correlation function calculated from the randomized trace (Equation 3.2) are shown in red. The lower plots show the influence of the different thresholds on the separation of regions of directed transport (shown in green) and stationary phases (shown in red) for the zoomed in region of the trace in panel (a).



## Chapter 4

---

# Multicolor 3D Orbital Tracking

Data obtained by 3D Orbital Tracking contains a large amount of information allowing for detailed analysis of the detected particle. However, the vast majority of feedback based single particle tracking (SPT) microscopes are designed for single color experiments due to high hard- and software complexity. Even though some exceptions being capable of dual color tracking exist presented by Keller et al. (2018), Liu et al. (2020), and Kis-Petikova and Gratton (2004), most SPT, none of the presented techniques has yet tackled the problem of tracking two individual freely diffusing particles in solution using a feedback approach.

This chapter presents a successful implementation of multicolor Orbital Tracking modalities on our setup. As briefly mention in subsection 2.2.4, the detection path of the confocal modality consists of two detection channels. With both channels in tracking configuration, dual color Orbital Tracking experiments are possible. In general, the type of experiments can be grouped into two categories: dual color tracking of correlative and independent diffusion. The first approach is suitable for particles that are in close proximity (on the scale of orbit size) during the motion. Here, the tracking feedback loop is activated for one detection channel. The second channel detects the fluorescence signal of the second particle for an orbit rotation at the position of the previous orbit without a lock-in on the current particle position. For individually freely diffusing particles, their separation can be larger than the orbit size and it cannot be assumed that both particles are permanently present in the same orbit. Hence, the feedback loop is enabled for both detection channels for the second category of dual color SPT. Now, the lock-in is performed for both particles and tracking is carried out by switching orbits between both particle positions.

Furthermore, one detection channel can be configured to detect the fluorescence of a Förster Resonance Energy Transfer (FRET) pair. In this modality, tracking is carried out in one channel while the fluorescence signal of a FRET pair is detected with the novel OPSPC logic in the other channel. This chapter will first give a brief overview of the microscope's soft- and hardware design that is executing the the Orbital Tracking program. After that, a detailed description of the new software architecture on the host level will be given. In the next step, the software extensions that execute the novel approach of combined tracking and FRET detection will be discussed. Here, the main focus will be on data acquisition and transfer. After introducing the software, key results of tracking experiments for each modality will be presented. For dual color 3D Orbital Tracking, two types of experiments will be discussed, serving as a proof of

principle. In the first one, red fluorescent spheres labeled with green emitting dyes were tracked to mimic correlative motion. This will be followed by individually tracking of red and green fluorescent beads in solution. As last proof of principle, experiments for the successful implementation of the combination of the 3D Orbital Tracking with parallel FRET readout will be presented. Here, beads labeled with green emitting dyes and a double stranded (ds) deoxyribonucleic acid (DNA) containing a FRET dye pair were tracked in solution.

## 4.1 Orbital Tracking Software

In feedback based SPT experiments, the acquired data has immediately to be processed in order to follow the particle of interest on the fly. Here, not all executions of the software are of same priority, i.e. required for the tracking feedback loop. Hence, it is crucial to identify such highly prioritized tasks. For instance, highly prioritized, or time-critical, processes in SPT are the position calculation of the particle after one orbit and the position update for the optical element to execute the next iteration. In contrast to those examples, less prioritized, or non time-critical, tasks are the writing of acquired data into files on disk or the visualization of it on screen. Delays in those processes do not influence the feedback loop of the tracking algorithm. Present processors can handle huge amounts of computational workloads in parallel. However, this parallelism is managed by multi-threading, meaning that computational resources are shared between active programs. Time slots for execution are assigned and scheduled to the programs. Due to this scheduling performed on the ms time scale, we perceive these quasi-parallel executions as parallel. However, those execution interruptions by multi-threading can impact feedback based SPT algorithms. Consequently, it is convenient to separate time-critical from non-time critical tasks and execute them on different hardware. In order to be able to communicate with each other, a sophisticated connection between the different hardware has to be configured. Figure 4.1 illustrates the hard- and software design which is used on the Orbital Tracking setup. It consists of a deterministic and a non-deterministic unit. The deterministic unit is hardware that guarantees the complete and correct execution of code in a given time. In this case, it consists of a field programmable gate array (FPGA) and real time (RT) processor. A non deterministic unit is conventional computer scheduled by multi-threading as described above. Each hardware component independently executes code which will be described in detail from page 40 on. Communication between the hardware components is carried out via tag communication and streaming. In general, variables are used for tag communication for updating and displaying parameters. For transferring acquired data from the deterministic to the non-deterministic unit, streaming is the method of choice. Compared to variables, which can only store one value at a time, streaming allows (to a certain extend) for buffering of data points. On the 3D orbital Tracking setup, this is implemented as first in - first out (FIFO) buffers and network streams.

The first program block, level **(1)**, has the highest complexity and priority. It is executed on a FPGA with a clock rate of 40 MHz. This code level is responsible for the exact



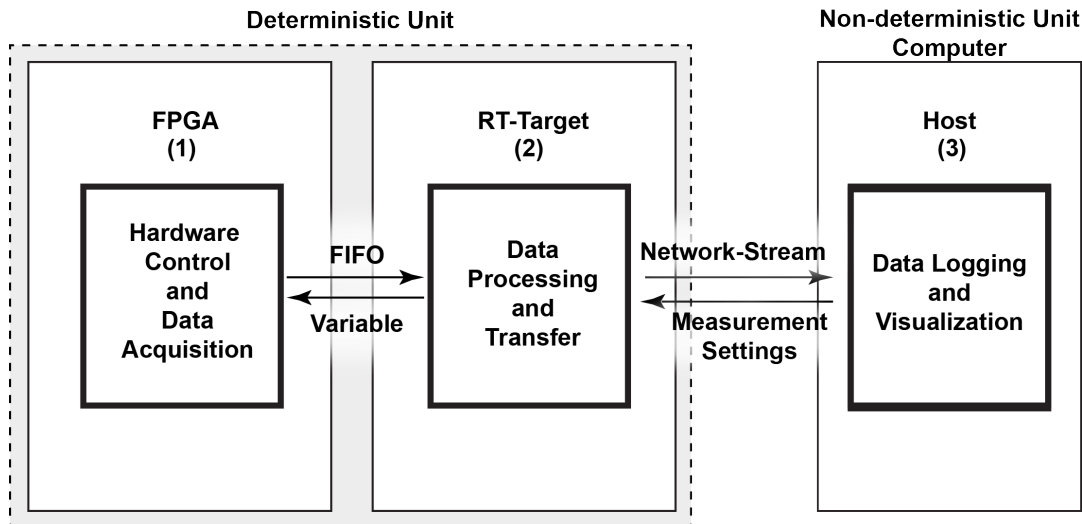


**Figure 4.1: Sketch of soft- and hardware architecture.** The orbital tracking program is executed on two independent hardware devices: a deterministic and a non deterministic unit for separating the execution of time critical from non time critical tasks. Furthermore, the software is split into three blocks of different complexity in terms of deterministic execution, decreasing in priority from (1) to (3).

hardware control and synchronization, i.e. applying the desired voltages on the control board to tilt the galvanometer driven mirrors, trigger the AOTF with transistor-transistor logic (TTL) pulses for alternating the lasers or sampling the TTL signals from the detectors. Furthermore, it transfers the sampled data to the processor (code block (2)) of the RT-target using the FIFO logic.

Level (2) in the program architecture can be described as a bridge between the FPGA and the non-deterministic unit. One important task is processing the transferred data sampled on (1). In case of orbital tracking, this is the calculation of the FFT of the detected intensity followed by the 3D position determination for each orbit rotation (page 27). Afterwards, the coordinates (in [V]) are updated on the FPGA by tag communication using a variable for the next orbit iteration. Furthermore, the received and processed data is transferred to the non-deterministic unit in a ethernet network by a network stream.

The code block of level (3) is the human machine interface (HMI). Here, the user can define the settings for the measurement via the graphical user interface (GUI) which are then updated by tag communication on the RT-target. Furthermore, it reads the data from the network stream and writes it to the hard disk.

The basic functions of the software are based on Wehnekamp (2016). It is developed in Laboratory Virtual Instrumentation Engineering Workbench (LabVIEW) 2018. However, for the implementation of 3D orbital tracking with FRET, two major changes of the code were required:

- decoupling data logging from data updating on the GUI (level (3))
- implementing code logic for the detection of the raw photon stream(levels (1 - 3))

The code structure for all levels will be discussed in detail in the following subsections.

### 4.1.1 Software Description: The Host

The software architecture on the non deterministic unit is based on the QMH template (Baros et al., 2019). This design allows for the parallel execution and synchronization of several tasks. In general, it consists of an event loop and a message handling loop. The event loop detects user events such as mouse hovers or button presses that are triggers for specific code executions. Those are scheduled and synchronized in the background by the message handling loop. The synchronization is achieved by message queues, which are data structures being capable of buffering objects in a defined order. The advantage of this software architecture is the separation of different execution tasks like the decoupling of data logging from data visualization. Furthermore, it is easily extendable for new modalities. Figure 4.2 illustrates the event loop's main GUI the hierarchy of the QMH of the current Orbital Tracking software that consists of front-end and backend components. In brief, frontend defines part of program that is visible for the user such as GUIs. Software components that are executed in the background without the user's perception are defined as backend. The current software consists of six subvirtual instruments (VIs) (modules). For synchronizing execution tasks, a dedicated queue is assigned to each module. A short summary of each module and its corresponding task is listed in table 4.1. Pressing one of the six buttons in figure 4.2(a) triggers a message cascade in the message handling loop which opens the corresponding frontend (more details in the *Profile Settings Module* (page 43) and in *Confocal Module* (page 41) subsections).

**Table 4.1:** Overview of modules, their tasks and types used in the QMH architecture of the RT Tracker software version 5.1.

Module	Task	Type
Profile Settings Module	user profile management	frontend
Confocal Module	subGUI management	frontend
Data Module	data logging	backend
Image Module	image processing on GUI	backend
Camera Module	camera handling	backend
Calibration Module	instrument calibration	frontend

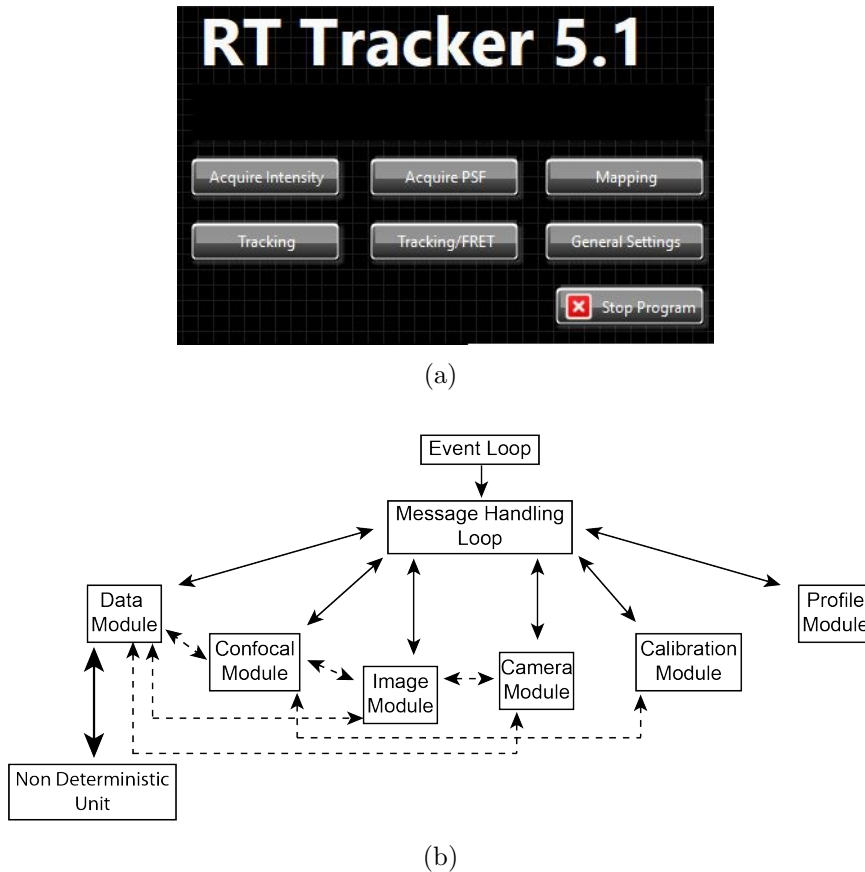


**Figure 4.2: Main GUI and execution hierarchy of the RT Tracker software version 5.1.** (a) MainGUI of the RT Tracker 5.1 software. Pressing one of the six button launches the corresponding subGUI. (b) Flow chart of the implemented QMH design. The interface in panel (a) is the frontend of the *Event Loop*. The *Message Handling Loop* synchronizes the execution of the modules by dedicated queues (solid arrows). In the background, the modules can exchange data and triggers between each other (dashed arrows). The *Data Module* is further connected via ethernet network to the deterministic unit (bold arrow).

### Profile Settings Module

The Profile Settings Module manages measurement parameter settings for different user. The specific data is stored in separate configuration files. After starting the the program, a GUI appears, on which either a existing user profile can be selected from a dropdown menu, deleted or a new file configured. When a profile is selected, the module loads the corresponding configuration file and reads the data from it. The data is sorted and updated in the variables accordingly. An overview is given in table 4.2. Most variables are *Clusters*, which is LabVIEW specific data type. A *cluster* is a container that can be individually configured by the developer. When creating a new user profile, a second GUI opens, which shown in figure 4.3. Here, measurement parameters can be configured. When closing the GUI, the data is written into the corresponding variables from table 4.2 and is accessible for the other modules. This window can further be

opened during execution of the program via the *General Settings* button of the main GUI (figure 4.2(a)) When quitting the program, this module writes the current state of the parameters into the corresponding configuration file.

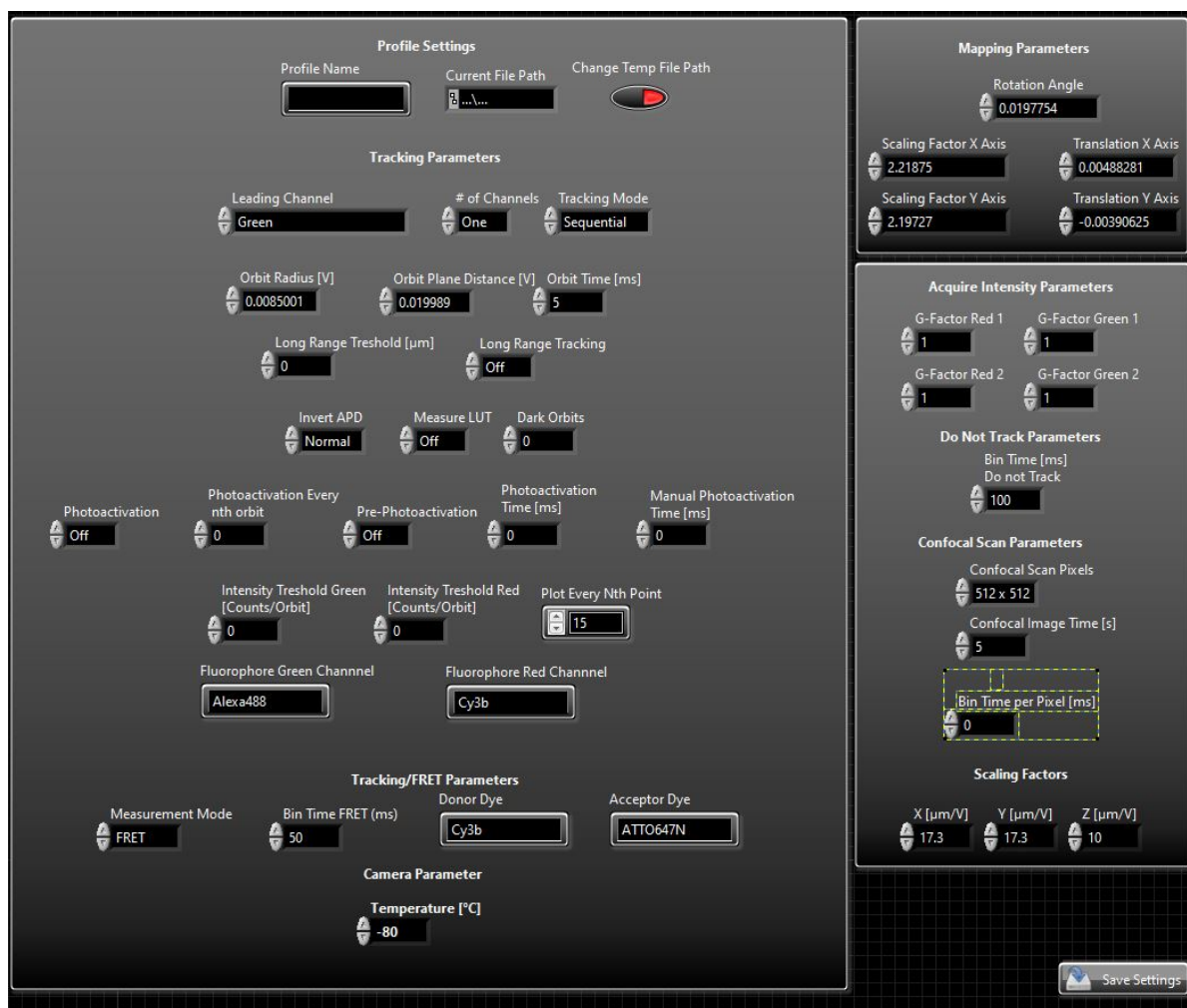


**Figure 4.3: General settings GUI launched by the Profile Module.** The parameters are grouped by the corresponding modalities of the program. The values are written into global variables and updated in the remaining modules.

**Table 4.2:** Overview of the variables used in the RT Tracker software version 5.1 listed in alphabetical order.

Variable Name	Data Type
Acquire Intensity	Cluster
Camera Settings	Cluster
Confocal Settings	Cluster
Plot every $n$ th orbit	I32
Scaling Factors	Cluster
Temp File Path	File Path

## Confocal Module

The Confocal Module is the main frontend code block of the software as it stores all GUIs of the subroutines that carry out different measurement modii. An overview of the implemented subVIs is listed in table 4.3. They can be launched by pressing a button in the mainGUI (figure 4.2(a)). When a subroutine is launched, all necessary parameters are read from the global variables (table 4.2 on page 43) and updated on the GUI. Each subVI is programmed in the event based state machine design (Lynch and Tuttle, 1989). State machines are suitable for small programs and allow for dynamic orders of code executions execution. For every GUI, this module is highly synchronized with the *Data Module*. When a task requires other modules, the synchronization will be automatically executed by the backend.

**Table 4.3:** Overview of subVIs, its tasks managed by the *Confocal Module*.

GUI	Trigger Button (from figure 4.2(a))	Task
Acquire Intensity (page 43)	Acquire Intensity	Readout of count rates
Acquire PSF (page 44)	Acquire PSF	Image scan
Mapping (page 45)	Mapping	Image calibration for camera and scan coordinates
Tracking (page 47)	Tracking	Execute Orbital Tracking code
Tracking/FRET (page 47)	Tracking/FRET	Execute combined Orbital Tracking/FRET code

## Acquire Intensity

When starting the RT Tracker software version 5.1, this GUI (figure 4.4) is automatically loaded after processing the profile tasks in the *Profile Settings Module*. Here, the detected count rate for all APDs, which are automatically grouped according to the detection

channel, is displayed in kHz. The user can activate the channels and define binning time [ms] for data acquisition.



**Figure 4.4: GUI of the Acquire Intensity subVI.** In this interface, the count rates of both detector pairs are displayed. The user can define the binning time parameter and activate the channels.

### Acquire PSF

In this subVI, PSF scans along the three coordinate axes can be carried out. The corresponding GUI is shown in figure 4.5. When starting this subroutine, the coordinates of the last tracked particle are extracted in the background. The user can define the PSF parameters, i.e. number of data points, binning time in [ms] and scan range in [ $\mu\text{m}$ ]. Using drop down menus, the channel as well as the coordinate axis can be chosen. The focus is then symmetrically steered over the defined range around the corresponding coordinate of the chosen axis using the galvanometer mirrors for the lateral and the piezo-nanopositioner for the axial PSF. The detected intensity is displayed on the screen for the corresponding APDs of the chosen channel in real time. This module is designed for detector alignment, especially for separating the detection volumina in  $z$  to obtain axial information of the particle position (see page 28).



**Figure 4.5: GUI of the PSF scan subVI.** In this subroutine, detection channel and coordinate axis on which the PSF scan is performed can be chosen. Furthermore, the number of data points per scan, binning time [ms] and scan range [ $\mu\text{m}$ ] can be defined. The scan is displayed on screen in real time.

## Mapping

The mapping subVI is used for the alignment of the wide field image, acquired from the EMCCD camera, with the image acquired in a confocal scan. It synchronizes itself in the background with the *Camera Settings* and *Image Module*. For carrying out the coordinate transformation, the back reflection of the laser on the surface of the coverslip is imaged on the camera. The galvano mirrors move the laser on a defined pattern to nine different points that span two orthogonal lines. The corresponding pixel coordinates of each laser reflection are extracted by center of mass analysis of the intensity distribution. A fitting routine then determines the transformation factors for both axes that are used for the calculation of the image transformation. To avoid high inaccuracies due to the low number of data points, the process is repeated until the difference of the determined rotation angle  $\varphi$  between the last two executions is less than  $0.3^\circ$ . Detailed information regarding the math of this mapping routine is given in Wehnekamp (2016).



**Figure 4.6: GUI of the mapping subVI.** A defined pattern of nine spots is scanned by the galvanometer mirrors. The laser is focused on the bottom of a coverslip and the backreflection recorded by the camera is displayed on the upper left panel (white). During the routine, pixel coordinates of the backreflection are extracted by a center of mass analysis and displayed in the middle panel. The calculated rotation angle  $\varphi$  is plotted against the number of iterations in the right chart. After completing the fit, the values are displayed in the GUI and written into the *Confocal Settings Variable*.



## Tracking

In this subVI, “classical” Orbital Tracking measurements (single or dual color SPT) are carried out. The corresponding GUI is shown in figure 4.7. When this sub-application is started, all required parameters are extracted from the global variables and updated in the background. If adjustments need to be done, the user can change the values of the corresponding parameters which are then written into the respective variable. After a confocal scan, which is displayed in the white panel in figure 4.7, the user can activate the tracking routine. By clicking into the scanned FOV, the tracking algorithm is started. The corresponding message is sent by the *Data Queue* to the *Data Module*. During tracking, the trajectory information, i.e. fluorescence count rate, orbit modulation, particle velocity and particle coordinates of the corresponding tracking channel are plotted in real time on the right. Furthermore, after tracking a particle of interest, the microstage can be controlled from this GUI to move the specimen and scan the next FOV. This subVI is further communicating with the *Image Module* as well as the *Calibration Module*. When recording a video during the SPT, the tracking VI is additionally synchronizing with the *Camera Module*. A newly implemented feature of this GUI is the automated trajectory saving function. After completing a track, the data acquisition of a trajectory is quit by the user, the corresponding file is automatically saved in the background to a user-defined file destination. For every trajectory file, the program concatenates the pre-defined filename with consecutive numbers to exclude overwriting of data.

## Tracking/FRET

This subVI is newly implemented into *RT Tracker 5.1*. Its GUI is illustrated in figure 4.8. The sub-program is able to carry out SPT in 3D with simultaneous FRET probing. Here, the user can choose between *FRET* and *ALEX* mode. In the *FRET* mode, only the donor excitation is activated. In the *ALEX*, the acceptor and donor excitation are alternated. The tracking procedure is implemented as mentioned above. However, two restrictions currently apply that should be mentioned:

1. SPT is defined for only 488 nm excitation.
2. The FRET pair needs to be suitable for 561 nm/633 nm excitation.

For optimizing the efficiency of data acquisition during time critical experiments, the equivalent trajectory parameters as well as the intensity traces of the FRET pair are plotted in real time. When the tracked particle does not contain the FRET pair or both dyes are photobleached, data acquisition can be stopped by the user. If the automated trajectory saving is enabled, the data is then saved in the background as explained above.

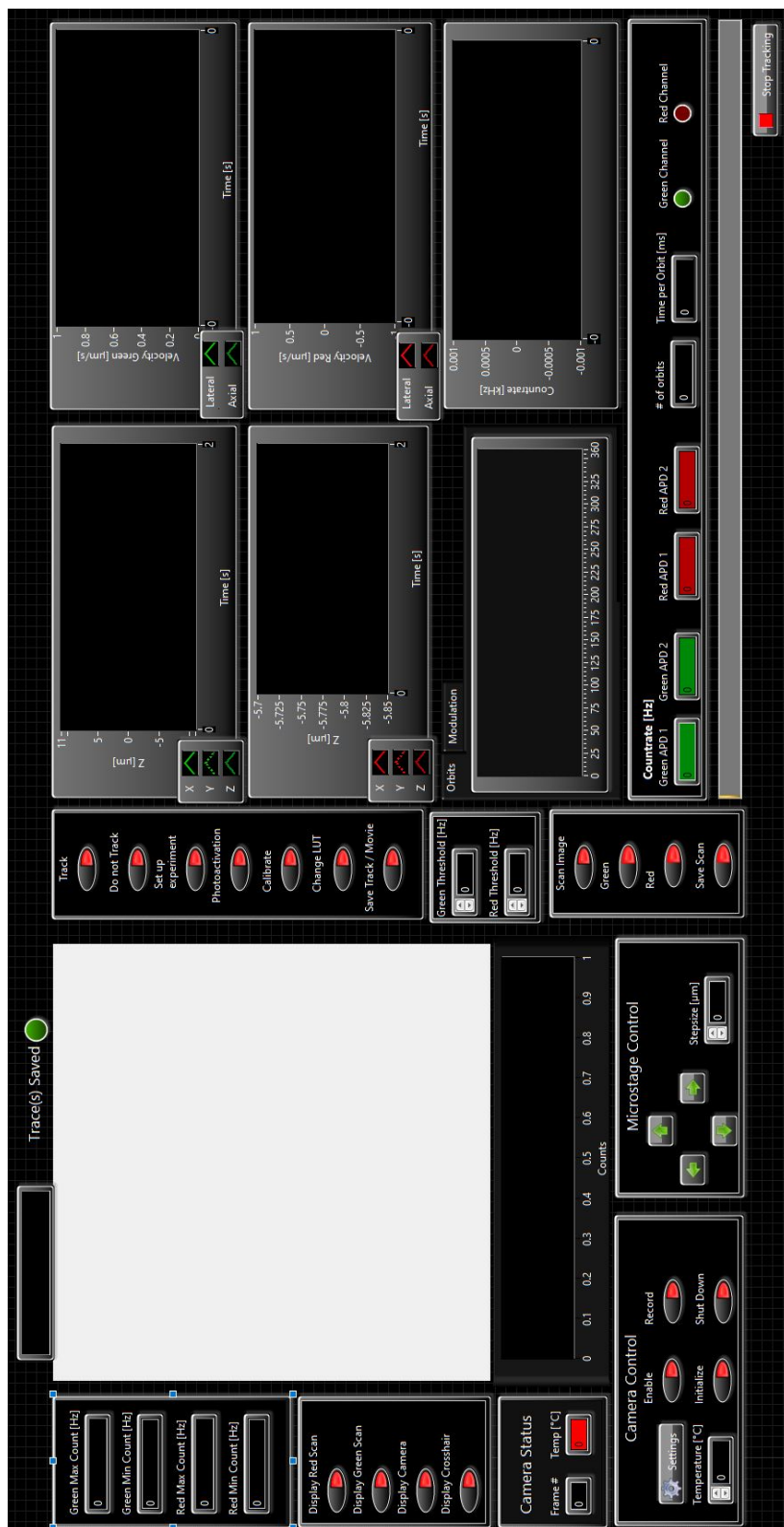


**Figure 4.7: GUI of the tracking subVI.** With this sub-program “classical” Orbital Tracking experiments can be run. In the white panel, the confocal scans of both detection channels can be superimposed. By clicking in this FOV, the tracking algorithm is started from these coordinates. During data acquisition, parameters of the trajectory are plotted in real time: coordinates and particle velocity of the corresponding channel, orbit modulation and detected intensity.

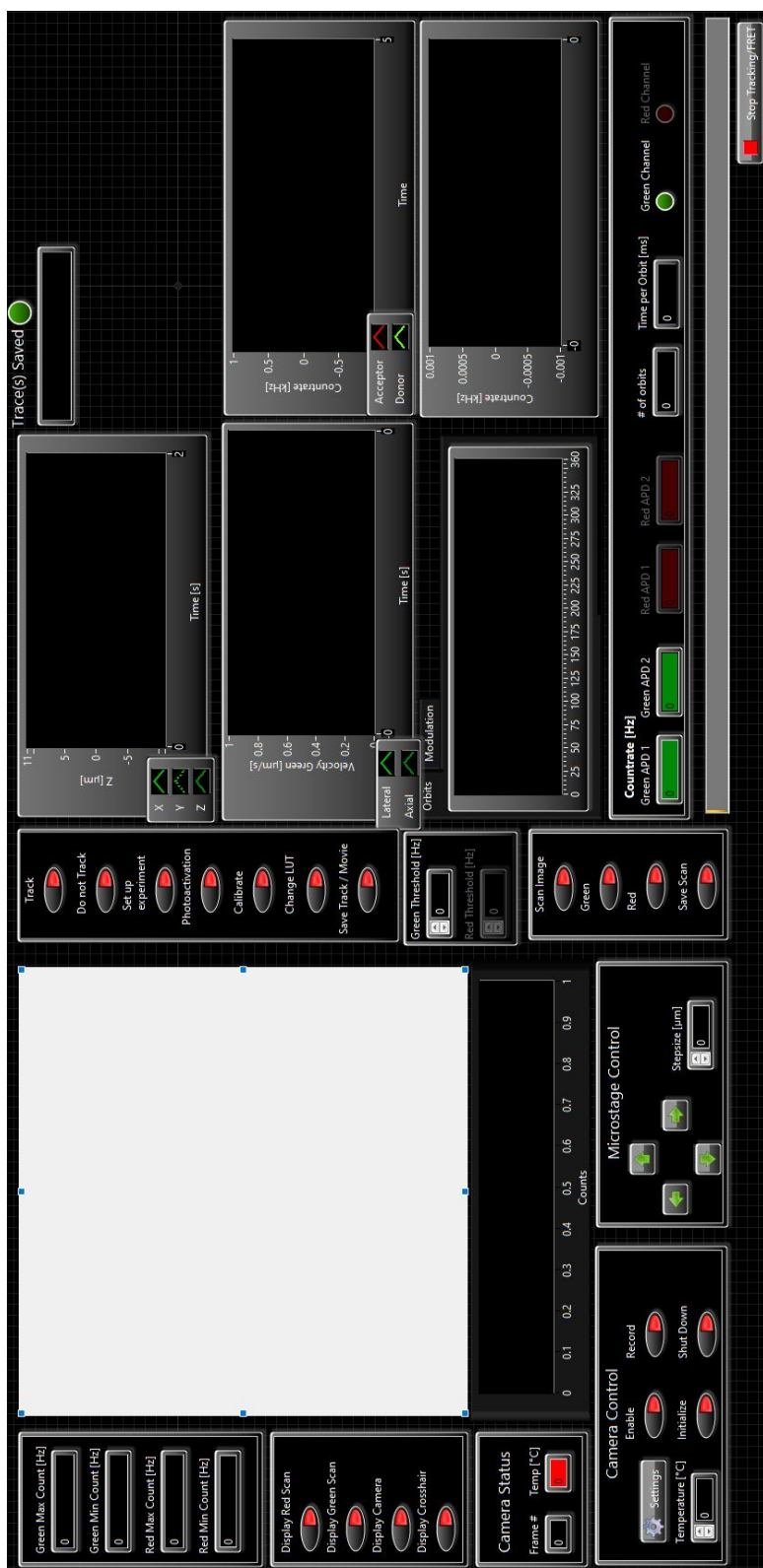


**Figure 4.8: GUI of the tracking/FRET subVI.** With this sub-program, combined orbital tracking experiments and FRET measurements are carried out. In the white panel, a confocal scans with 488 nm excitation is displayed. By clicking in this FOV, the tracking/FRET algorithm is started from these start coordinates. During data acquisition, parameters of the trajectory as well as the intensities of the FRET pair are plotted in real time.

## Data Module

The *Data Module* is responsible for the communication between the non-deterministic and the deterministic unit executing in the background. When the user starts data acquisition in one of the subVIs presented before, the *Confocal Module* sends the corresponding message via the *Data Queue* to this module for executing the required code. The module then reads the required data for the data acquisition mode from the global variables. If necessary, the parameters are converted into fixed-point (FXP) representation to be processed by the RT target. Next, the values are written into the corresponding network variable and sent to the deterministic unit followed by a starting trigger for data acquisition. Afterwards, the *Data Module* reads the data from the network stream which is processed before being saved on the hard drive. The data is also streamed by the *confocal queue* to the *Confocal Module* to be displayed in the GUI. When data acquisition is ended, i.e. the user aborts the measurement or the data acquisition time is elapsed, the *Data Module* stops reading the network streams and sends a trigger command to the RT unit to stop the task. A general sketch of the three main execution blocks are illustrated in figure 4.9.

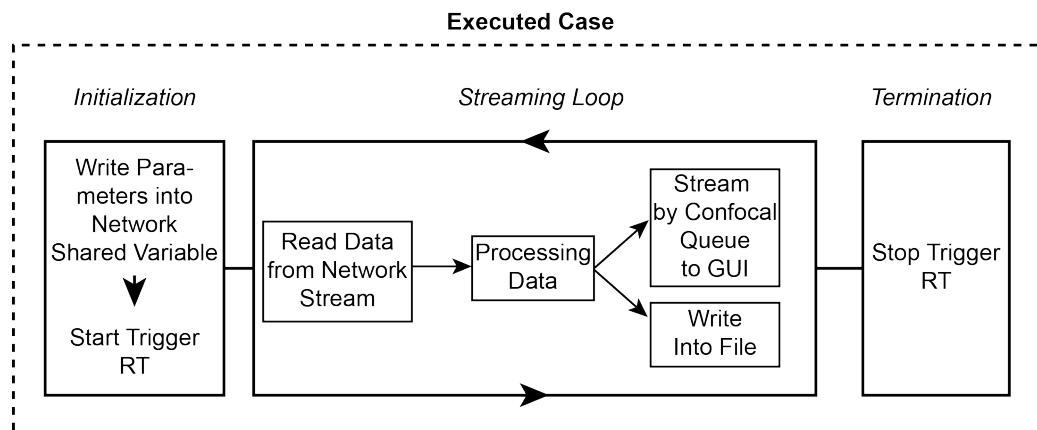


**Figure 4.9:** Main principle steps performed by the *Data Module* during data acquisition.

After receiving the data acquisition message from the *Confocal Module*, the corresponding case is executed. First, the required parameters are read from the global variables, translated and written into network shared variables to be updated on the deterministic unit. In step 2, it reads the acquired data from the network stream, which is then processed, written on the hard drive and streamed by the *Confocal Queue* to the GUI to be displayed on screen. This loop is executed until either the user quits this process or the measurement time is elapsed. In the last step, the *Data Module* sends a trigger command to the deterministic unit to end the task.

This module executes two special tasks when starting and closing the RT Tracker software version 5.1, i.e. activating/sending the deterministic unit from/to standby and creating/destroying three network streams between the host and the RT target. Three network streams are required due to the newly implemented Tracking/FRET mode, which will be discussed in more detail on pages 52 to 54.

The main advantage of the new software architecture is the separation of data logging from the GUI in which the data is visualized on the screen. In general, the visualization is very resource intensive and will consequently lead to interruptions of time critical tasks, which are crucial for feedback based SPT. From the four following steps being iteratively executed by feedback based SPT software,

1. read-out of the network stream
2. data processing
3. data logging
4. displaying on screen

the last step would be the bottleneck and slows down steps 1–3. In worst case, the buffer of the network stream could overflow. Newly acquired data can then not be written into the network stream and is lost. Furthermore, with the QMH design, it is possible not to stream all acquired data, but to send snapshots of it. As the human eyes and brain can process image data at rate of roughly 30 Hz, there is absolutely no need to stream at a higher update rate and hence sacrifice resources of the central processing unit (CPU). Another new implementation worth mentioning, is the automatic restart of the RT target after three unsuccessful attempts to establish the network streams.

### Image Module

The *Image Module* handles the RGB images of the two detection channels as well as of the widefield image recorded by the EMCCD camera. It updates the the image panel in the corresponding GUI. During confocal scans, the *Data Module* updates this module by tag communication, ensuring that the complete image data is transferred after the scan. Furthermore, it scales the received image data into intensity and extrapolates the image to  $512 \times 512$  pixels if the scan was carried out at lower resolution. This module updates the reference in the corresponding GUI in real time by tag communication, i.e. the scan image is built up on the fly. If a video is recorded in parallel, the image transformation is calculated in this module. During tracking, this module updates and displays the crosshair with the current lateral coordinates of the particle diffusion in the FOV.

### Camera Module

This backend module carries out the camera control. It updates the specified settings, e.g. exposure time, gain or operating temperature, on the device. The corresponding functions are stored and implemented in this module by a dynamic link library (DLL). When the camera is activated during a measurement, the *Camera Module* receives a start trigger from the *Confocal Module*. It then activates the RT unit for external camera triggering.

## Calibration Module

The Calibration Module triggers the deterministic unit to move the xy-Piezo controller - and hence the specimen - in precised steps that are defined by the user while orbiting at the same position. This is useful for generating the LUT (see page 27). Furthermore, it can send a command to the RT unit to apply a sine-patterned voltage on the Piezo controller to simulate particle motion. This module can only be called from the *Tracking* and *Tracking/FRET* GUIs.

### 4.1.2 Software Description: The RT-Target

The program code on the RT target is implemented as an executable. The device is held in standby until it receives the start trigger from the host, which is sent by the *Data Module*. This action initializes the implemented code. First, the bitfile that contains the compiled code for the FPGA is loaded on it. After that, a connection to the host is established using three network streams. Furthermore, the required communication ports to the desired hardware components are opened. The algorithm is designed by two state machines depicted in figure 4.10, which run independently of each other.

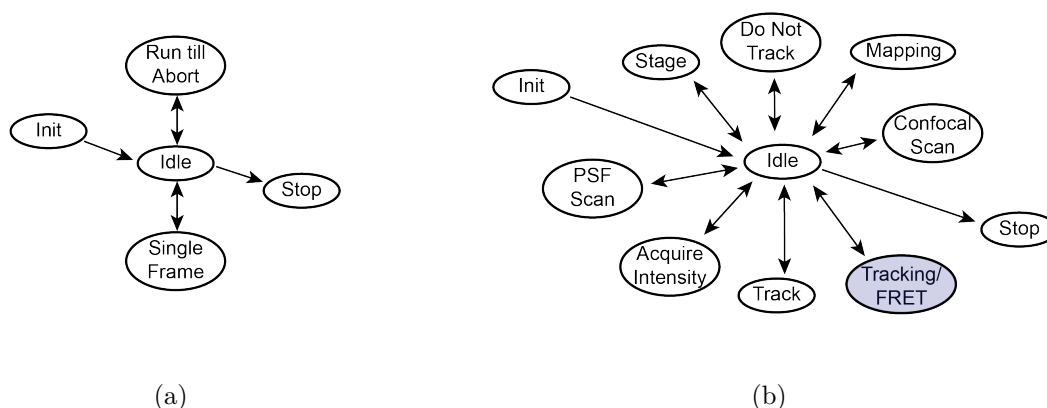


**Figure 4.10: State machines implemented on the RT target.** (a) The camera state machine executes the synchronization necessary for external triggering of the EMCCD camera. (b) The confocal state machine receives trigger commands from the *Data Module* of the non-deterministic unit. It updates the parameters on the FPGA, receives the acquired data and transfers it via network connections to the host.

The camera state machine communicates with the FPGA, sending the parameters for external camera triggering. The confocal state machine bridges the FPGA with the host for data exchange during the experiment. When the user has selected a certain measurement type, the corresponding trigger sent by the *Data Module* of the non-deterministic unit is read first. The state that is connected to this trigger is selected and executed. In general, the basic steps of tasks for the states are the same as illustrated in figure 4.11. In step one, the required parameters are extracted from the shared network variables

to load them on the FPGA. After accomplishing this, a trigger command for data acquisition is sent. In step two, the data is read from the FIFO buffer for processing. If the measurement type requires active feedback, the processed values are updated on the FPGA by tag communication. In parallel, the data is written into the buffer of the corresponding network stream and sent to the host. When acquisition is finished, the FPGA task is stopped by a trigger command.

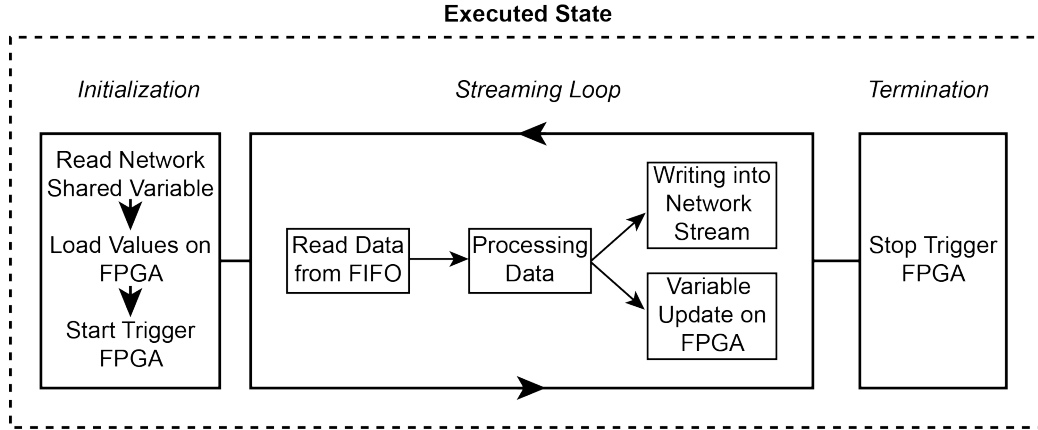


**Figure 4.11: Main principle steps of the state machine RT target during data acquisition.**

After receiving a data acquisition command from the host, the corresponding case of the state machine is executed. In step one, the required parameters are read from the corresponding network shared variable and loaded onto the FPGA followed by a start trigger for data acquisition. After the initialization, the streaming loop that can be grouped into three code blocks is executed. First, the acquired data is read from the FIFO and processed in the second step. In the third code block, this data is written into the corresponding network stream and transferred to the non-deterministic unit. If the feedback loop is active on the FPGA, the position data is updated by tag communication. When the streaming loop is terminated, the RT unit sends a stop trigger to the FPGA.

The already implemented functions are explained in Wehnekamp (2016). Only the new extensions will be discussed in detail on the following pages. As already shortly mentioned, three network streams listed in table 4.4 are established for connecting the deterministic and the non deterministic units.

**Table 4.4: List of all implemented network streams between the deterministic and non-deterministic units.** Each stream sends different data independently.

Name	Data Type	Task
Tracking	U64	tracking data transfer
Raw Photon	U64	RPS data transfer from the FRET pair
Binned FRET Intensity	U32	binned intensity transfer from the FRET pair

The implementation of three network streams is necessary because the sampling frequency for each type is different. In a typical SPT experiment, the orbit is rotated

at 200 Hz. However, for obtaining maximum time resolution in the raw photon stream (RPS), this data is sampled on the maximum clock rate of the FPGA, which is 40 MHz (see detailed description on page 54). Due to the nature of fluorescence, neither the photon absorption nor the emission can be predicted in time. Hence, it is theoretically possible that photon emission and orbit completion can occur at the same point of time. In this case, it would not be possible to transfer both values simultaneously from the FPGA to the RT target to be streamed. If the binning time of the binned FRET intensities is a multiple of the orbit time, the same problem would occur between these two data streams.

A new implemented feature in the confocal state machine on the RT target is the *Tracking/FRET* state executing the following tasks. Here, SPT with simultaneous FRET readout is executed. The 3D position of the tracked particle is calculated as explained on page 25. By tag communication, the last coordinates are transferred to the FPGA. In parallel, the photon data is read from the RPS-FIFO and written into the *Raw Photon* network stream. Furthermore, another FIFO that is sending binned intensity data from the FRET pair is read after every loop iteration. In case of available data, it is written into the *Binned FRET Intensity* network streaming, which will be explained in the following chapter in more detail.

### 4.1.3 Software Description: The FPGA

Three independent loops are programmed on the FPGA, which are executed in parallel. One loop consists of a simple data polling design. It executes the calibration routine for the LUT determination and the sine patterned voltages on the xy-Piezo scanner. Similar to the RT unit, the two remaining loops handle the camera triggering and the different measurement modes. Both are based on the state machine design sketched in figure 4.12.

A new implemented state into the confocal state machine is the *Tracking/FRET* feature. Here, the FPGA triggers the hardware necessary for performing SPT with 488 nm excitation combined with FRET readout for a 561 nm and 633 nm suitable dye pair. The tracking algorithm is the same as explained in Wehnekamp (2016). In brief, the FPGA controls the galvanometer mirrors, which rotate the laser beam in a circular pattern defined by 16 points in a given time. For each orbit point, the fluorescence intensity is detected by both APDs and transferred to the RT unit by a target to host direct memory access (DMA) FIFO. The theoretical maximum achievable time resolution would be here  $\frac{1}{16}$  of the chosen orbit time. To obtain the maximum time resolution for the FRET pair, the following changes have been implemented into the software. First, the excitation is alternated to prevent spectral crosstalk from the tracking fluorophores into the FRET channel. It is possible to choose between two excitation patterns represented in figure 4.13. Second, both channels are decoupled from each other, i.e. the SPT feedback algorithm is only enabled for 488 nm excitation and deactivated for the remaining laser lines. This means, the instrument tracks the particle of interest, stays at the last position while orbiting with one of the two remaining wavelengths for the FRET measurement before performing another position update.



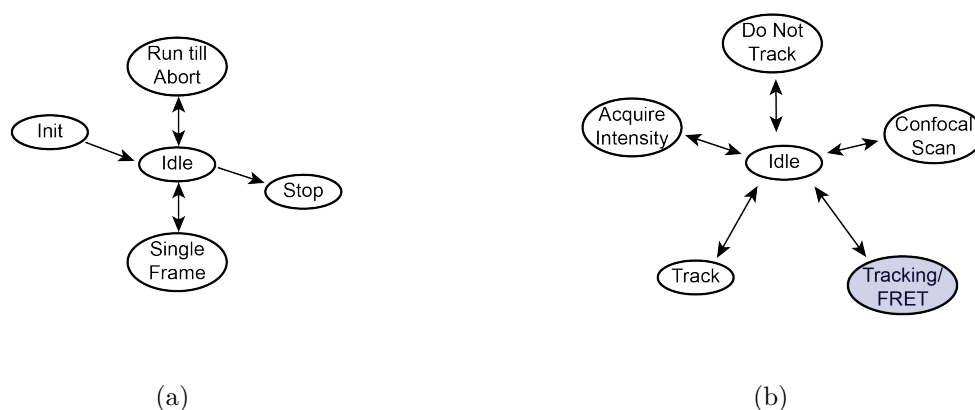


**Figure 4.12: State machines implemented on the FPGA.** (a) The camera state machine triggers the AOTF for the lasers in the widefield channel as well as the EMCCD camera. (b) The confocal state machine receives trigger commands from the RT target. It controls/triggers the required hardware, samples for new data and streams it by FIFO to the RT target. The colored state is a new implemented feature into the software.

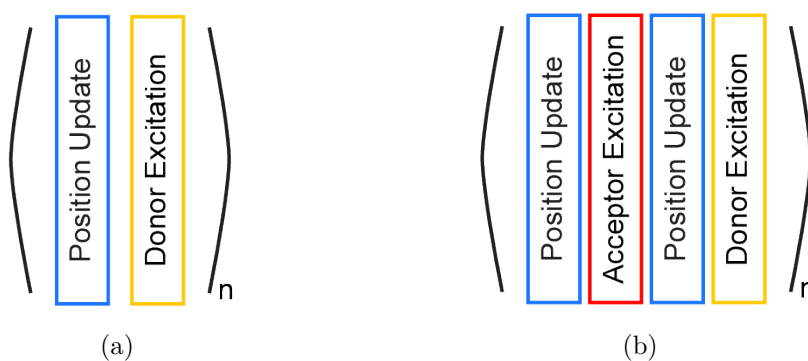


**Figure 4.13: Implemented laser excitation schemes for the new Tracking/FRET mode.** (a) FRET mode: the laser excitation alternates between 488 nm for tracking and 561 nm for the FRET measurement. Each block represents one orbit rotation. (b) ALEX mode: the laser excitation alternates between 488 nm for tracking and 561 nm/633 nm in the shown pattern for FRET measurements while alternating the laser excitation between the donor and acceptor fluorophores. Each block represents one orbit rotation.

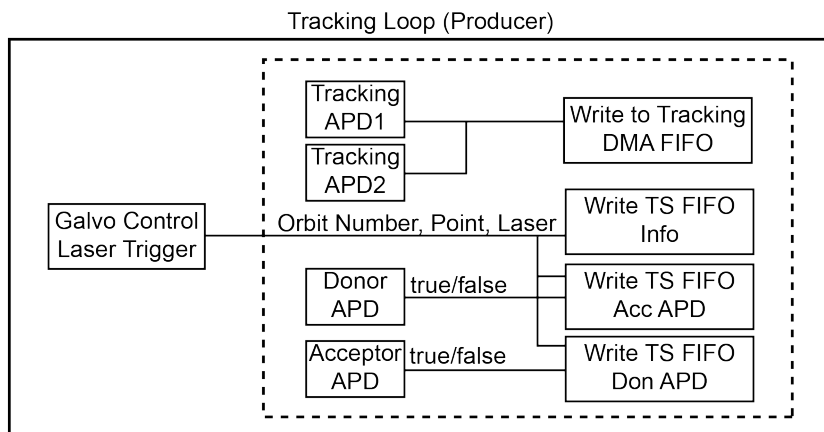
Third, a new detection logic based on TCSPC is introduced for detecting photons in the FRET channel with the maximum time resolution of 40 MHz and referred to as orbit point single photon counting (OPSPC). For this, a producer-consumer design pattern, which consists of two single-cycle timed loops, is implemented as illustrated in figure 4.14. The single-cycle timed loops guarantee the deterministic execution of the implemented logic. When a photon is detected by one of the two APDs of the FRET channel, the received trigger is written into one of the two the corresponding target scoped (TS)-FIFO buffer, which are optimized for data streaming on the FPGA. A third TS-FIFO transfers additional information, i.e. the current excitation wavelength,

the number of performed orbit as well as the current laser position on the defined circular points. To avoid tremendous network traffic during data transfer as well as huge data files, only photon signals from the FRET pair are streamed to the RT target and non-deterministic unit. For acquiring OPSPC information from the tracking fluorophores, the source code has to be adapted accordingly. The second single-cycle timed loop counts clock cycles at 40 MHz, representing the photon microtime. Furthermore, it constantly reads the values from the two detector- and the information FIFOs. As soon as this loop receives a photon trigger, which is a boolean TRUE, the counted photon microtime together with additional information are then multiplexed into a U64 integer as listed in table 4.5. This value is transferred by a second DMA-FIFO to the RT target. After that, the corresponding microtime counter is set to zero for the next iteration. This new OPSPC design allows reconstruction of the FRET trace of each tracked particle.

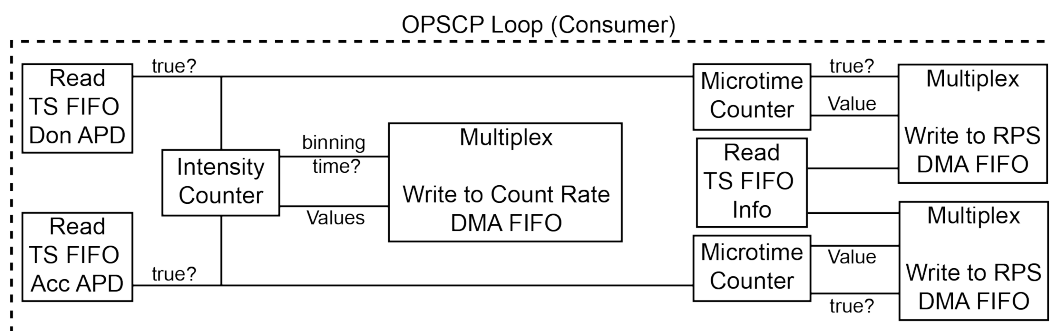
**Table 4.5: Overview of multiplexed photon information stored as a U64 integer.** Each piece of information is stored in the reserved part of a boolean array that is then converted into a U64 integer.

Start Index	Length of Sub Array	Information
0	1	Detector
1	1	Timed out?
2	2	$\lambda_{ex}$
4	1	Mode
5	5	#Orbits
10	22	Orbit Point
32	32	Microtime

In parallel to the OPSPC logic, this loop bins the detected photons for both laser lines. Every 50 ms, the U32 integer values of both detectors are converted into boolean arrays, concatenated and reconverted into an U64 integer. This value is transferred by a third target to the host DMA-FIFO to the RT target that transfers the data to the non-deterministic unit as described in subsection 4.1.2. Here, the data is displayed in the GUI in real time, giving current information regarding the dye pair to the user. If desired, the user can change this binning time in the program.



(a)



(b)

**Figure 4.14: Producer-consumer design of the OPSPC approach for the Tracking/FRET state.** The dashed rectangles represent timed loops at 40 MHz execution. (a) In the tracking loop, first the lasers are triggered according to the chosen excitation scheme. Then, the galvanometer mirrors are positioning the laser on the current orbit point. Afterwards, the signals of all four APDs are sampled for the specified binning time ( $\frac{1}{16}$  of orbit time). If the tracking laser is active, the data of the tracking APDs are streamed by the *tracking* DMA FIFO to the RT target for position determination. For the activation of a non tracking laser, the Donor/Acceptor APDs are sampled. The signals are streamed by the corresponding TS-FIFOs to the OPSPC loop. In parallel, a third FIFO transfers the photon information including orbit number, point and excitation source to the consumer loop. (b) The OPSPC loop acts as a photon microtime counter. It measures the time interval between two consecutive photons of the same excitation source. If a photon is detected, the microtime and all information are multiplexed into an U64 integer and streamed by the RPS DMA-FIFO to the RT target. In parallel, the detected photons are binned in a specified time window, multiplexed and streamed by another DMA-FIFO to the target for displaying the current count rate on screen.

## 4.2 Key Results

To highlight the implementation of an additional detection channel on the setup as well as the new capabilities upon software, two types of experiments were carried out: dual-color tracking and tracking combined with FRET. Furthermore, the dual-color tracking experiments can be divided into two types. The first one is tracking of two independently moving particles, the second one the so called correlative tracking. In the first type, the sample contained a mixture of red and green fluorescent beads, which were tracked independently. To mimick correlative diffusion, red fluorescent beads were labeled with ATTO488 fluorophores. The feedback loop of the tracking software was activated for the red emission of the bead while the presence of ATTO488 signal was probed by orbiting with a deactivated feedback loop around the last position of the bead. The detected intensities, trajectories as well as the calculated distance between the trajectories of both experiments are given in figure 4.15.

Panels (A-C) of figure 4.15 illustrate the detected intensities of two independently tracked beads, their 3D trajectories and the distance between them during the track. The independent diffusion of both particles can be observed in the well distinguishable traces. The grey, spiral shaped motion at roughly 3.25 ms and 3.75 ms indicates the activation of the search algorithm in the red channel due to loss of the corresponding bead. This independent motion is further confirmed by the calculated distance between the beads, which is not constant but varying over time. In this example, the maximum distance between both particles was more than 20  $\mu\text{m}$  (figure 4.15 panel C). Furthermore, a MSD analysis revealed that the diffusion is not dominated by Brownian motion but flow with an average flow parameter of  $1.7 \mu\text{m s}^{-1}$  for both particles. This flow was expected due to the harsh mixing of the beads in the sample chamber generating turbulences. Both beads showed a slightly different diffusion coefficient of  $0.84 \pm 0.04 \mu\text{m}^2 \text{s}^{-1}$  for the blue and  $1.03 \pm 0.05 \mu\text{m}^2 \text{s}^{-1}$  for the red particle.

The corresponding plots of a red fluorescent bead labeled with ATTO488 for correlative motion are given in panels (D-F). As expected, both trajectories are identical, which is also confirmed by the constant distance of  $\lesssim 100 \text{ nm}$  between both tracking channels. The offset is explained by the temporal delay of 5 ms between alternating orbits. Additionally, a MSD analysis of the quasi identical trajectories revealed Brownian motion with identical diffusion constants of  $0.11 \mu\text{m}^2 \text{s}^{-1}$ .

In general, it was observed that the tracking duration for two independent particles was shorter than that for single particle tracks and dual-color measurements in correlative mode. The reason for this is the continuous switching of the instrument between two different locations after each orbit which leads to a higher probability of losing a particle. This higher probability is mainly caused by the response time of the z-Piezo nanopositioner for the objective. Hence, the axial position of the particle may not be perfectly matched, leading to a faster loss of the particle.

In the next step, silica beads were labeled with ATTO488 and DNA containing a FRET pair. In this configuration, the tracking channel of the red fluorescent bead from previous experiments served as the FRET detection channel with the donor and acceptor signals split between the detectors. The 3D trajectories and the detected fluorescent intensities

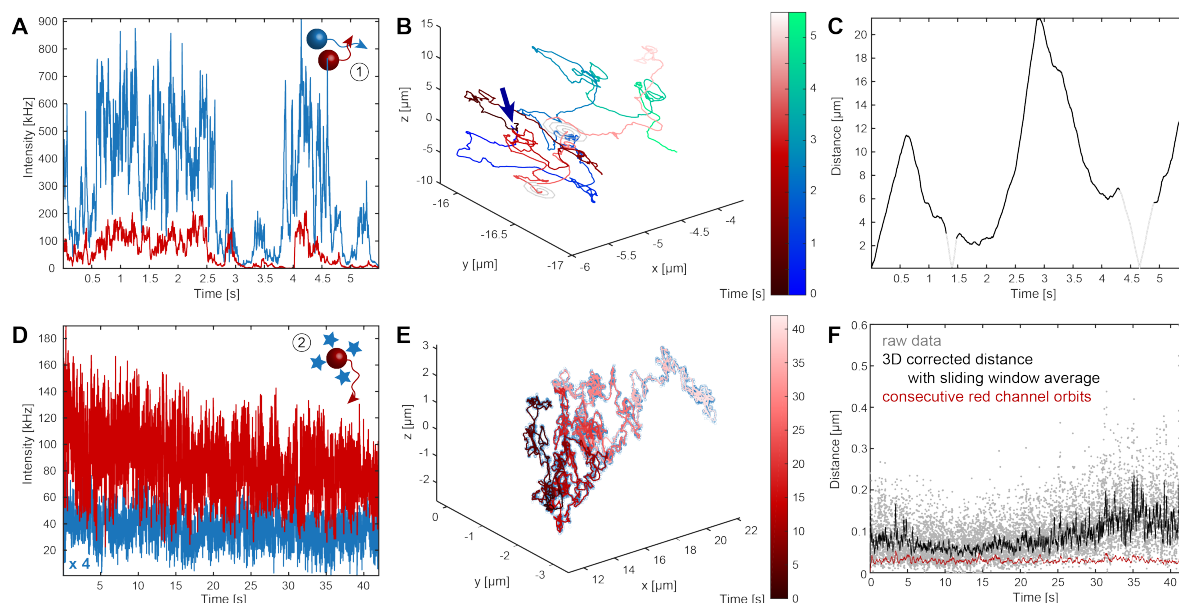


**Figure 4.15: Dual color tracking of beads.** Dual-Color Tracking of beads. A–C) Independent motion: A) fluorescence intensities, B) 3D trajectories, and C) relative distance between the two independently diffusing particles. The beginning of the trajectories is indicated by the arrow in panel (B). The particles exhibit separations of up to  $20\ \mu\text{m}$ . The blue intensity and blue-to-green color-coded trace correspond to the particle excited at  $488\ \text{nm}$ . The red signal and the black-to-red color-coded track correspond to the bead excited at  $633\ \text{nm}$ . The grey data points in panels B and C indicate regions where the red particle was not detected within the orbit. D–F) Correlative motion: D) fluorescence intensities of the red and blue signals corresponding to the fluorescent emission of the bead (with  $633\ \text{nm}$  excitation) and dye (with  $488\ \text{nm}$  excitation). To make it more visible, a factor of four has been applied to the intensity of the blue channel. E) A 3D correlated trajectory of a red-emitting bead labeled with ATTO488. The red trace represents the position of the red particle and the blue cloud surrounding the trace depicts the localization of ATTO488 probed during the tracking of the red particle. F) The distance between emission from the red particle and the ATTO488 probed signal (grey). The solid lines represent a sliding window average of 50 orbits for the correlative tracking (black) and for consecutive orbits of the tracking channel (i.e., the red channel in this case shown in red).

of three representative particles containing FRET pairs of different distances are shown in panels (A–F) of figure 4.16. The corresponding FRET histograms are given in panels (G–I).

The trajectories show the expected Brownian motion. A MSD analysis of all tracked particles showed diffusion coefficient centered at  $0.17\ \mu\text{m}^2\ \text{s}^{-1}$ .

The blue traces in the intensity plots correspond to the tracking channel, originating from  $\sim 25$ – $30$  ATTO488 molecules bound to the surface of the bead. The purple traces indicate the acceptor emission after  $633\ \text{nm}$  excitation. The orange and red traces correspond to the ATTO565 (donor) and ATTO647N (acceptor) signals after  $561\ \text{nm}$  excitation, respectively. After background correction, the traces were further corrected for direct excitation ( $\bar{\alpha} = 0.47$ ), spectral crosstalk ( $\bar{\beta} = 0.21$ ) and detection efficiency ( $\bar{\gamma} = 0.70$ ). The obtained FRET efficiencies were 25.7%, 63.1% and 80.6% for the

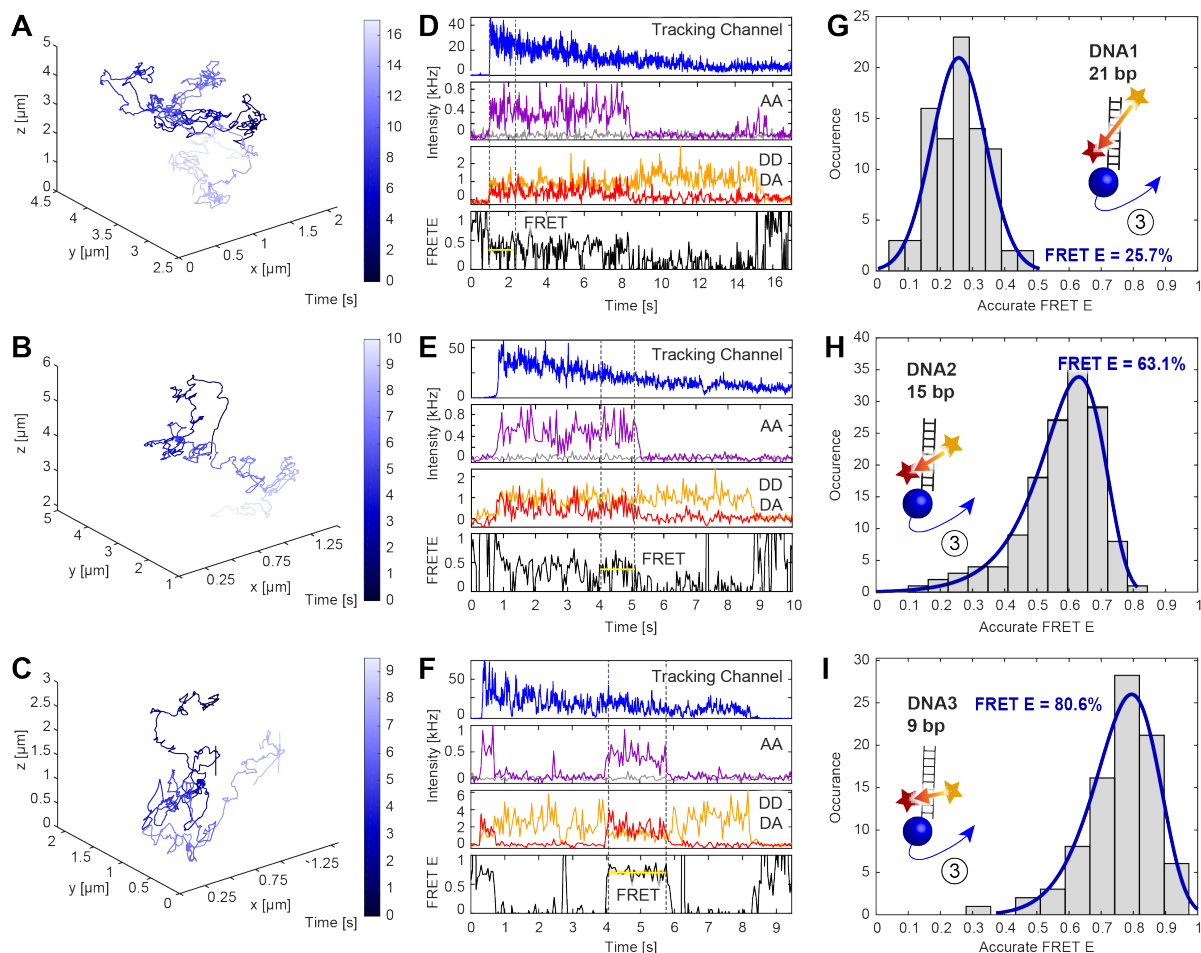


**Figure 4.16: Single-molecule FRET measurements on diffusing DNA molecules.** Single-molecule FRET measurements on diffusing DNA molecules. While tracking the reference beads marked with ATTO488 dyes in solution panel (A–C), we monitored the signature of single DNA-based FRET standards panel (D–F) that were attached to the particle via a biotin-streptavidin interaction. The dsDNA oligos were double-labeled with ATTO565 and ATTO647N. The donor dye was positioned at three different distances with respect to the acceptor dye. The resulting oligos are characterized by a G) low FRET value of  $\approx 26\%$  (DNA1), H) an intermediate FRET value of  $63\%$  (DNA2), and I) a high FRET value of  $81\%$  (DNA3).

low, intermediate and high FRET constructs. The low and intermediate FRET values are well in line with the results obtained from accessible volume (AV) calculations and control experiments by PIEMFD. Although the high FRET efficiency deviates about  $11\%$  from PIE-MFD results, it is clearly distinguishable from the other two species.

## Chapter 5

---

# Software Development for Correlative Imaging by Stimulated Raman Scattering and Photoluminescence

Despite the great power of the fluorescent-based techniques, not all systems can be investigated using fluorescence as different artifacts can occur due to size or required concentration of the labels (fluorescent quenching). For studying such systems, label free Raman scattering can be the technique of choice. This chapter will describe the novel software for a laser microscope that is capable of carrying out simultaneous imaging by SRS and photoluminescence including TCSPC logic. The microscope is based on the previously published design (Fuchs et al., 2022) and extended by a LIA, a photo diode and a cRIO-9074 (components listed in table 5.1) that synchronizes data acquisition.

**Table 5.1:** Implemented modules in the cRIO-9074 device.

Module Name	Type	Task
NI 9402	Digital	Generation of modulation signal
NI 9215	Analog In	Acquisition of analog detection signal
NI 9263	Analog Out	Generation of output voltage for hardware control

The general task of the software is the control and synchronization of multiple electronic devices through different communication ports during measurements. Here, the hardware and software design is chosen to separate time critical from non time critical tasks as described in detail in section 4.1. A simplified sketch illustrating the different executions on the deterministic and non-deterministic units is provided in figure 5.1. The deterministic unit consists of a RT processor and a FPGA. The measurement software on both hardware components consists of two independent state machines that are responsible for data acquisition and signal modulation necessary for the detection of SRS and TCSPC signals. Communication and data transfer are realized by tag communication and streaming, accordingly, as described on pages 38 and 39.

The non-deterministic unit is the human machine interface (HMI) receiving the acquired data, providing the graphical user interface (GUI) that is visualizing the data and providing possibilities for the user to define measurement parameters. Additionally, it communicates with the laser and the TCSPC card (TimeHarp260), realized by TCP/IP protocols (direct via ethernet cable) and a dynamic link library (DLL), accordingly.

In the following sections, the implemented software on each hardware level will be discussed.

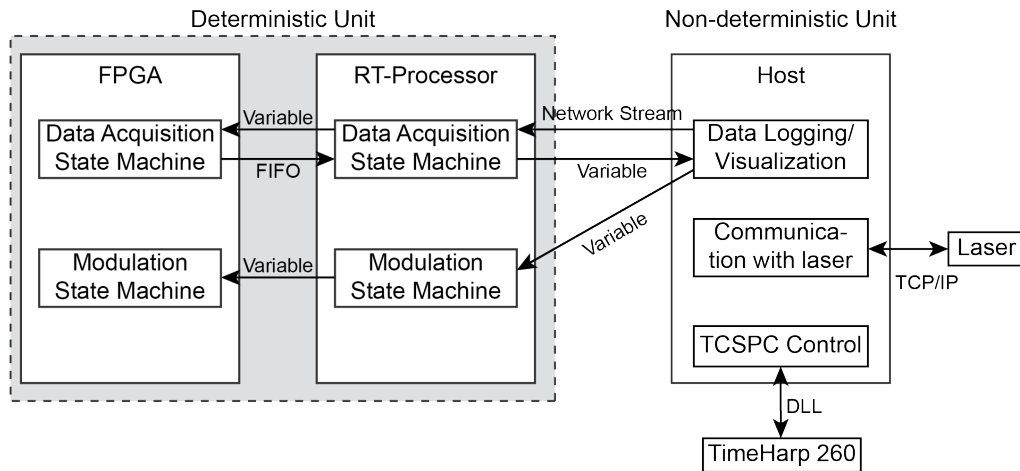
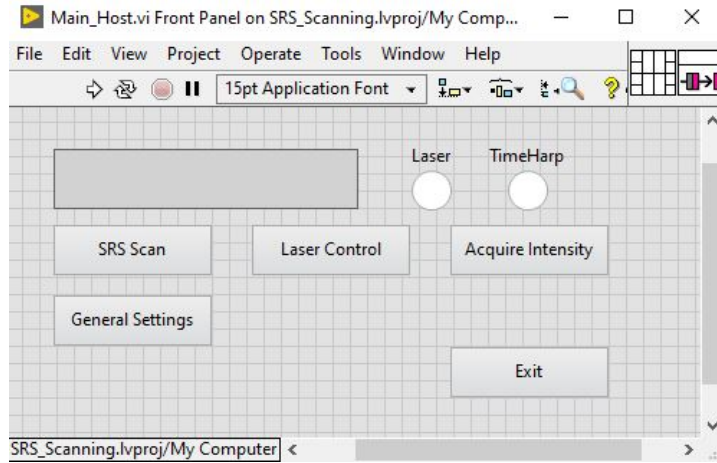


**Figure 5.1: Sketch of soft- and hardware architecture for the confocal microscope capable of synchronous SRS imaging and photon-based microscopy.** The instrument consists of deterministic and a non-deterministic unit to separate execution of time critical from non time critical tasks. The deterministic unit consists of a RT unit and a FPGA with two independent state machines, which are responsible for data acquisition and generation of a modulated TTL signal, implemented on each. Communication between both devices is realized by tag communication and the acquired data is streamed from the FPGA to the RT processor by a FIFO. The non-deterministic unit performs three major tasks: logging/visualization of the data received from the deterministic unit via network stream, control of the laser via TCP/IP protocols and of the TCSPC card by commands called from a DLL.

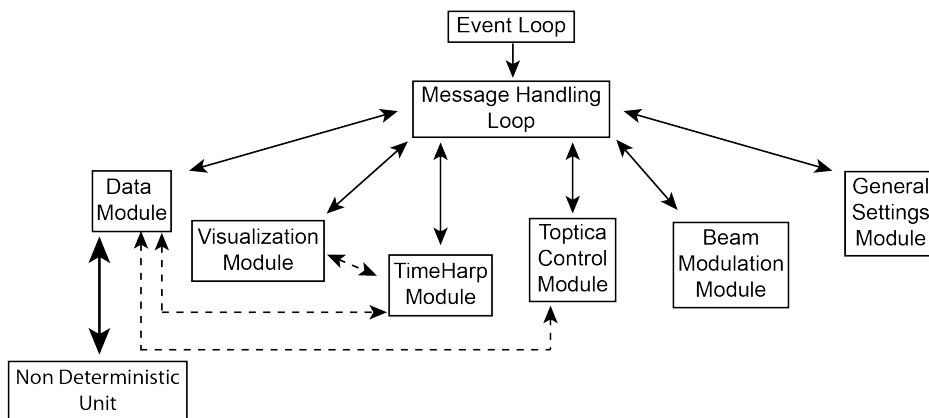
## 5.1 Software Description: The Host

Similar to the Orbital Tracking software described in section 4.1, the software architecture is based on the QMH design consisting of several modules that communicate with each other by queues. A list of all modules including the corresponding queues and tasks is provided in table 5.2. The corresponding main GUI of the program illustrated in panel (a) of figure 5.2, is the main entry point for the user to select different modes and change settings. It also displays if a connection to the laser and TimeHarp260 card is established, which is indicated by the two *Laser* and *TimeHarp* LEDs. The corresponding execution hierarchy of the software design is sketched in figure 5.2(b). The message handling loop communicates with each module indicated by the black arrows. Additionally, some modules use tag communication for triggers and value updates of variables in the backend (dashed arrows). Measurement parameter updates are handled by global variables listed in table 5.3. A detailed description of each module will be given in the following.





(a)



(b)

**Figure 5.2: Main GUI and execution hierarchy of the SRS software.** (a) MainGUI of the SRS software. Pressing one of the four buttons launches the corresponding subGUI. (b) Flow chart of the implemented QMH design. The interface in panel (a) is the frontend of the *Event Loop*. The *Message Handling Loop* synchronizes the execution of the modules by dedicated queues (solid arrows). In the background, the modules can exchange data and triggers between each other by tag communication (dashed arrows). The *Data Module* is further connected via ethernet network to the deterministic unit (bold arrow).

**Table 5.2:** Overview of modules, their tasks and types used in the QMH architecture of the SRS software.

VI	Task	Type
General Settings Module	Parameter/user management	frontend
Visualization Module	SubGUI management for different data acquisition modes	frontend
Data Stream Module	Data logging	backend
Beam Modulation Module	AOM trigger	frontend
Toptica Module	Laser handling	backend
TimeHarp Module	TCSPC card handling	backend

### 5.1.1 Settings Module

The Settings module manages experimental parameters based on user profiles. The user profile data is stored in separate text files. After starting the the program, a GUI appears, on which either an existing user profile can be selected from a dropdown menu, deleted or a new profile configured. When a profile is selected, the module loads the corresponding text file and reads the data from it, which is then stored and updated in the corresponding variables. An overview is provided in table 5.3. Most variables are defined as clusters (detailed description on page 41), which groups several parameters. Figure figure 5.3 illustrates the GUI that appears when a new user profile is created. Here, measurement parameters can be configured, which are written into the corresponding variables from table 5.3 when closing the GUI. It can further be opened by the *General Settings* button of the main GUI (figure 5.2(a)). Furthermore, this module writes the current values of the parameters into the corresponding text file, when closing the program.

**Table 5.3:** Overview of the variables used in the SRS software listed in alphabetical order.

Name	Type	Task
Modulation Variables	Cluster	Storage of Modulation parameters
Data Acquisition Variables	Cluster	Storage of Acquisition parameters
TH260 Variables	Cluster	Storage of TCSPC parameters
Laser Variables	Cluster	Storage of laser parameters
TempFilePath	Path	Folder path to temporary files
TCSPC-CR	U64	Detected count rate of TCSPC card
LoopSync	Boolean	Loop synchronization between modules

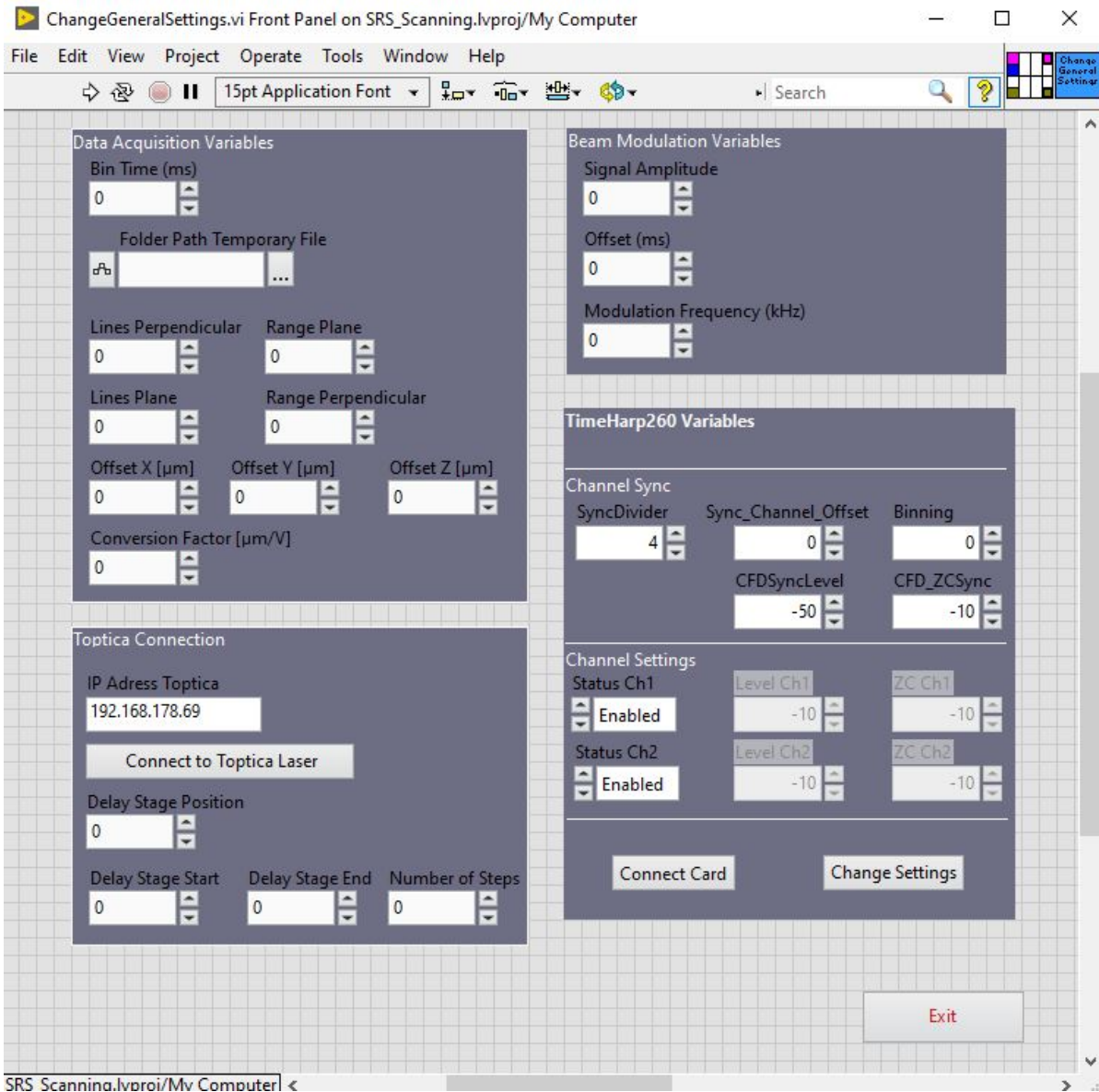


**Figure 5.3: General settings GUI of the SRS software.** The setting parameters are categorized by different execution tasks of the program. The values are written into global variables and updated in the corresponding modules.

## 5.1.2 Visualization Module

The Visualization Module is the main frontend code block of the program as it stores all GUIs of the subroutines, which are responsible for different tasks in the backend. Table 5.4 lists all implemented subVIs that can be launched by pressing the corresponding button in the mainGUI (figure 5.2(a)).

**Table 5.4:** Overview of subVIs, the corresponding trigger buttons and their tasks managed by the Visualization Module.

GUI	Trigger Button (from figure 5.2(a))	Task
Acquire Intensity (page 66)	Acquire Intensity	Readout and plot of acquired SRS signal
SRS Scan (page 69)	SRS Scan	GUI for carrying out SRS scans with/without parallel TCSPC logging and acquiring of SRS spectra after scan

### Acquire Intensity

In this subVI, the detected electronic signal of the LIA, which is proportional to SRS scattering of a selected vibrational mode in the sample, is plotted against time. The corresponding GUI is shown in figure 5.4. When starting a measurement by pressing the *Start Acquisition* button, a trigger is automatically sent to the Data Stream Module. Furthermore, the GUI displays the current position of the laser's delay stage. The position can be changed in the *Move Delay Stage* input at any time. After terminating the data acquisition by the *Start Acquisition* button, which triggers the start and termination of data acquisition, the acquired data can be saved in a text file. A second subVI can be opened by pressing the *Measure Spectrum* button for measuring a temporal SRS spectrum, which will be explained on page 68 in more detail.

### SRS Scan

The SRS Scan module is the most sophisticated module of the software and hence the most advanced GUI, which is shown in figure 5.5. It synchronizes the acquisition and storage of SRS scattering detected by a photodiode and a LIA as well as the simultaneous detection of the photon-based signature via TCSPC technology during raster scan of the specimen. Therefore, the module deals with the largest number of communications and synchronizations with respect to other modules (Data Stream, Time Harp and Toptica Module) within the software. The graphical interface is vertically split into two categories, of which the left part manages the SRS data acquisition and the right part the TCSPC signals of the TimeHarp260. The left side contains a panel where the image of the SRS scan is built up line by line during data acquisition, which is written into a

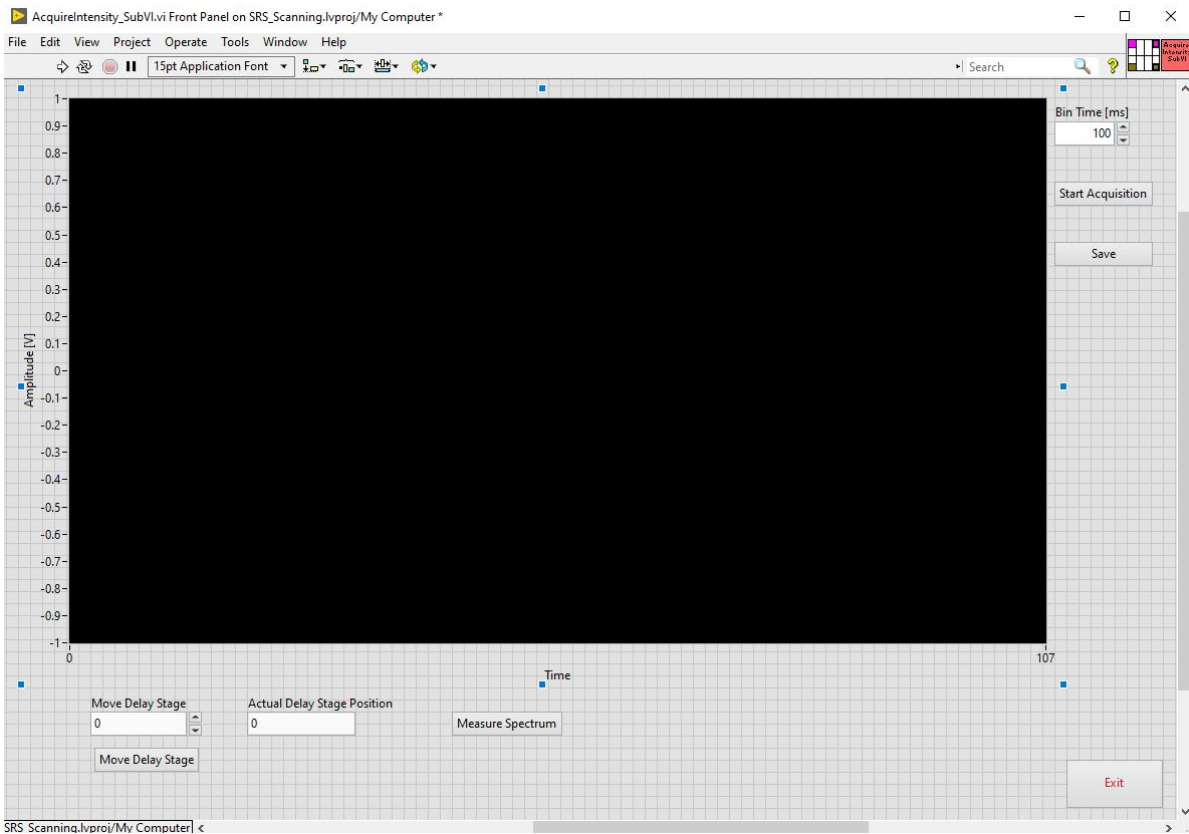


**Figure 5.4: GUI of the Acquire Intensity subVI.** The electronic signal detected by the LIA is plotted over time in this interface. The binning time parameter can be changed by the operator on the fly. Furthermore, the delay stage of the laser can be moved independently from the data acquisition. Another GUI can be launched via the *Measure Spectrum* button, in which temporal SRS spectra can be measured.

tiff and text file. Below this docker, several inputs are provided to the user to define the scan settings. The size and the resolution of the scanned image are in the *Range Scan* [ $\mu\text{m}$ ] and *Lines Plane*, respectively. The software automatically calculates the number of pixels by taking the square of the *Lines Plane* parameter. The acquisition time for each pixel is adjusted in the *Bin Time* [ $\mu\text{s}$ ] input. It further defines the scan time for the whole image, which is automatically calculated by the software and displayed. The number of images to be scanned is set in the *Lines Perpendicular* parameter. For each scan, the image data is written into extra files that are named with consecutive numbers. Furthermore, a set of images can be acquired as a 3D stack defined in the *Range Perpendicular* [ $\mu\text{m}$ ] input (value greater zero). All permutations for 3D stacks on the three room axes are possible. The type of the 3D scan is chosen in the drop down selection of the *Scanning Type* input. Furthermore, the piezo stage can be moved to new coordinates in two different ways. In the first option, the values are defined in the three *Piezo Position* [ $\mu\text{m}$ ] inputs. By pressing the *Move Piezo* button, the stage moves to the new positions. In the second option, the user can click into the image. The corresponding inputs of the lateral coordinate pair are automatically updated by the

values. After activating the *Move Piezo* button, the stage moves to the new positions, defining the center of the image.

On the right side of the GUI, the data acquisition of the dual channel time harp is enabled/disabled by the corresponding button. In the enabled state, the software automatically acquires TCSPC signals from two APDs during a scan. In addition to the two SRS files, the photon data is automatically written into a third ptu file, a standard file format that can be processed by the in-house developed analysis software *PAM* (Schrimpf et al., 2018).

The last modality of this subVI is the acquisition of SRS spectra. The corresponding GUI (further details on page 68) is launched by the *Measure Spectrum* button. In this case, the spectrum is measured at the center of the image. Furthermore, the software is capable of automatically acquiring a set of spectra at different coordinates of a scanned image. For this, several positions have to be selected by clicking into the image. The *Measure Spectra* button then triggers a routine consisting of three steps: moving to the selected coordinates, acquiring the spectrum and saving the data into a dedicated text file. These steps are repeated until all spectra are measured for all positions. A detailed description of the SRS spectrum acquisition will be given in the next section.

### Measure Spectrum

With this subVI, SRS spectra from the current sample are acquired. It is launched from the *Acquire Intensity* (page 66) and *SRS Scan* (page 66) GUIs. In case of a series of spectra scans, the GUI is automatically launched and closed for each execution. During data acquisition, the subVI communicates and synchronizes itself with the *Data Stream* (page 72) and *Toptica* (page 72) modules. The detected electronic signal of the LIA is plotted in Volts against the laser's delay stage position in the upper half of the GUI shown in figure 5.6 after the data acquisition is finished. The corresponding data is written into a text file that it can be saved for later analysis. Below the plot, several inputs are available, which define the settings for the spectrum acquisition. The *Delay Stage Start* and the *Delay Stage End* input parameters define the range on the stage that the step motor of the laser is moved during the spectrum acquisition. These dimensionless numbers are later translated into wave numbers during the analysis. The resolution of the spectrum is controlled by the *Number of Steps* parameter, which sets the step size for the movement of the stage. Furthermore, it is possible to click into the spectrum and move the stepping motor to the selected position. With this feature, the signal can be maximized for each sample by a simple fine tuning of the system.

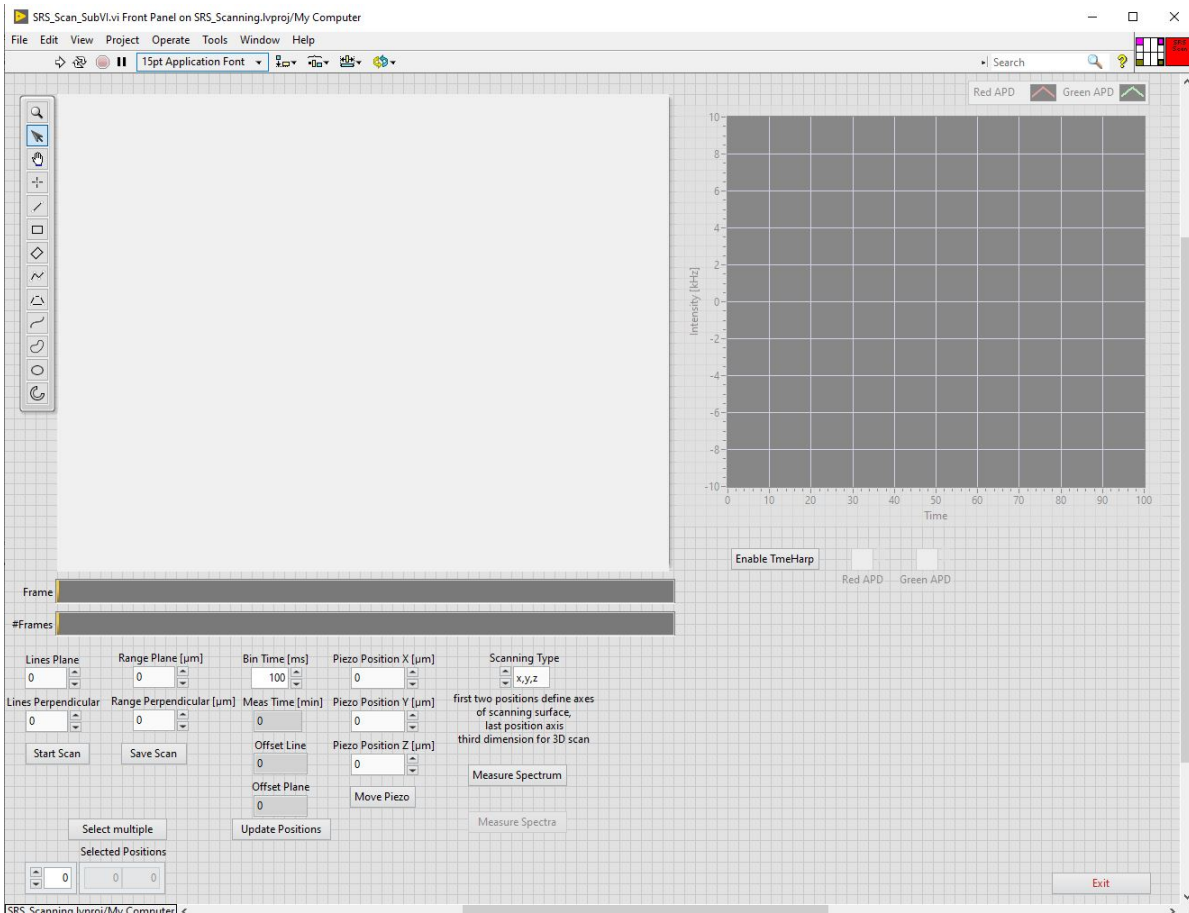


**Figure 5.5: SRS scan GUI of the SRS software.** The graphical interface is vertically categorized into two groups. On the left side, the image of the scan is built up line by line in the gray container. Below this, the input parameters for the scan, which can be adjusted by the user, are located. The parallel acquisition of the TCSPC signal originating from photoluminescence can be en- or disabled on the right side. When enabled, the count rate, acquired by the TCSPC card, is plotted over time in the intensity chart.

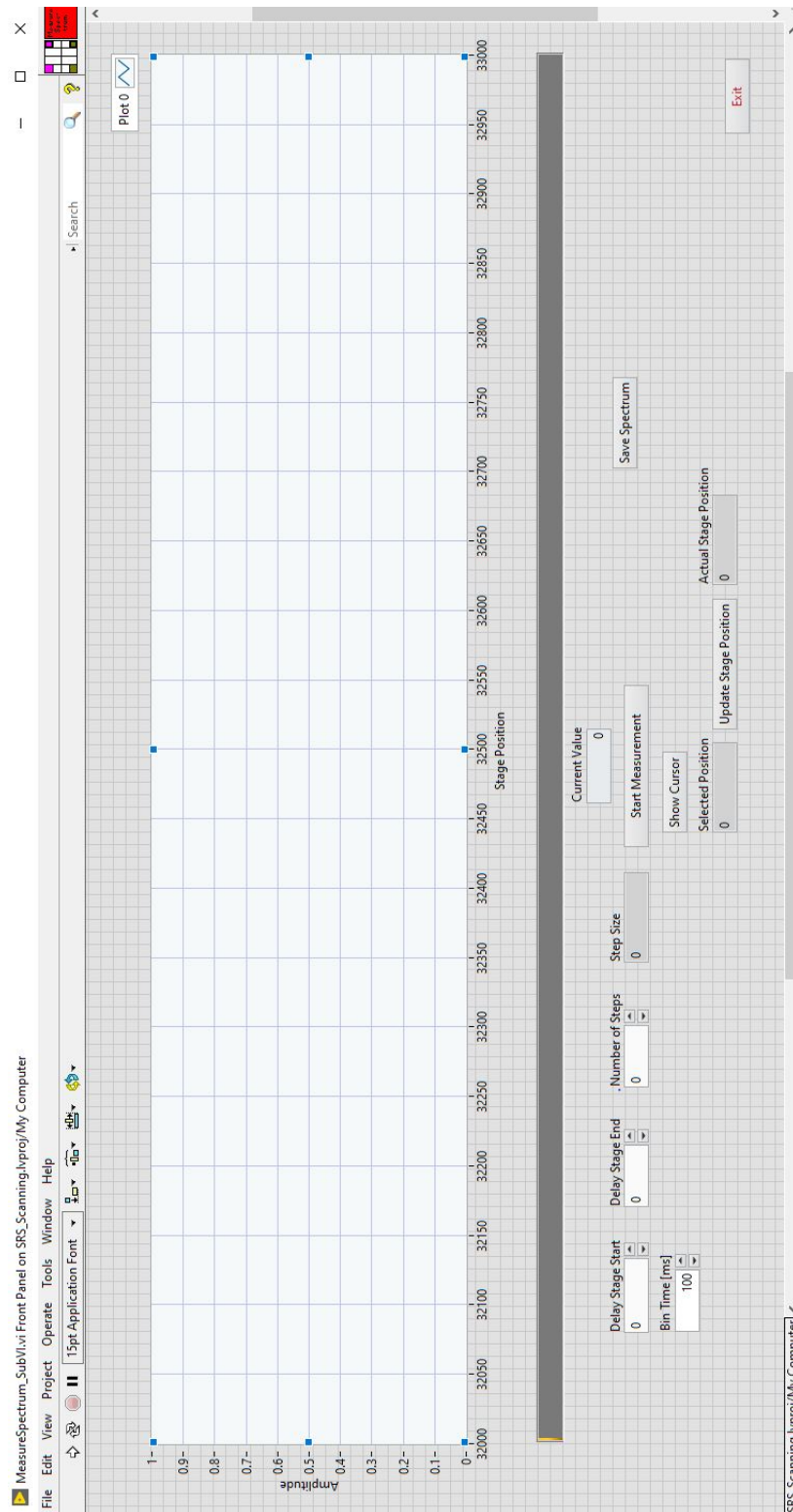


**Figure 5.6: Measure Spectrum GUI of the SRS software.** SRS spectra are measured in this graphical interface that is launched from the Acquire Intensity and SRS Scan GUIs. The input parameters can be adjusted by the operator. In the case of a series of spectra scans, this GUI is automatically launched and closed for each execution.



### 5.1.3 Beam Modulation Module

The modulation frequency for the AOM of the laser and the LIA can be adjusted with this subVI. It is executed independently from the other modules and can be launched at any time. As shown in figure 5.7, the GUI consists of three input parameters: *Modulation Frequency*, *Offset* and *Signal Amplitude*. The frequency input values are defined in [kHz], which are automatically converted to the corresponding period  $T$  and the number of clock cycles on the FPGA by the software. Since the input frequency can only be adjusted by a multiple of 40 MHz, the theoretical value will be rounded to the nearest multiple of the FPGA clock frequency that is then used for the TTL signal generation. All calculated values are displayed in the GUI. The offset parameter defines the time in [ms] that delays the start of the modulation. The *Signal Amplitude* regulates the output power of the laser by applying the input value in [V] to the AOM. Finally, the modulation is switched on/off by the *Beam Modulation* button.

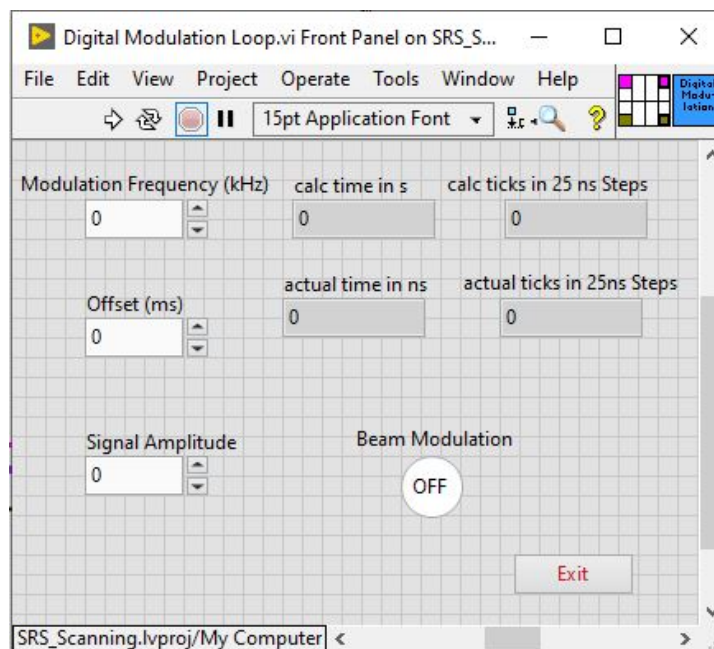


**Figure 5.7: Beam Modulation GUI of the SRS software.** Three parameter inputs, which can be set by the user, are located on the left side of this GUI: *Modulation Frequency*, *Offset* and *Signal Amplitude*. The corresponding period  $T$  of the input frequency is calculated and converted to a multiple of the FPGA clock cycle at 40 MHz. These theoretical values are rounded to the nearest multiple of this clock cycle. An offset for the start of the modulation can be set in the corresponding input, if desired. The laser power in [V] is regulated by the *Signal Amplitude* input. The modulation is then triggered with the *Beam Modulation* button.

### 5.1.4 Toptica Module

The *Toptica Module* is a backend subVI of the QMH architecture that communicates with the laser through a direct ethernet connection and the TCP/IP protocol. When the software is started, this module automatically tries to establish the connection to the device. During data acquisition, it sends or reads parameters such as hardware state or the delay stage position by remote commands called from a DLL.

### 5.1.5 TimeHarp Module

The *TimeHarp Module* is the interface to the TCSPC card, a TimeHarp 260 model, in the backend of the software. The communication is carried out by commands that are called from a DLL. When starting the SRS software, the module automatically initializes the TCSPC card with the parameters loaded from the selected user profile (page 65). When the TCSPC mode is enabled in the SRS Scan Module described on page 66, the *TimeHarp Module* receives a start trigger when a scan begins. The software then generates a ptu file in which the acquired photon data including line and frame triggers are written. This is a standard file format that can, for example, be processed by the in-house developed analysis program *PAM* to reconstruct the scanned images from the photon arrival times as well as the corresponding triggers (Schrimpf et al., 2018). For displaying the currently acquired count rates of both APDs during a scan, the corresponding values are read from the TimeHarp and sent via tag communication (two global variables) to the SRS Scan Module where they are plotted on the left chart shown in figure 5.5. After completion of the scan, the subVI receives a stop trigger and generates a text file containing meta data, which is necessary for the processing in *PAM*. When the software is closed, the module cancels the connection to the TCSPC card.

### 5.1.6 Data Stream Module

The *Data Module* is the interface to the deterministic unit in the backend. When the program is started, it triggers the real-time unit from stand-by to the active state. It contains all algorithms for the different data acquisition modes originating from SRS presented in subsection 5.1.2. The general execution scheme for each case is illustrated in figure 5.8. During the *Initialization* step, the required parameters are read in from the *Data Acquisition Variable* (see table 5.3). If needed, the parameters are converted into a FXP representation before being written into the corresponding network shared variables. Then, a start trigger is sent to the RT unit, followed by starting the *Streaming Loop*. This loop iteratively reads data from the network stream, writes it into the corresponding data file and streams the values to the active GUI of the *Visualization Module* until it receives a stop trigger (cancellation by user) or no data is anymore available on the network stream. A stop trigger is then sent to the RT unit to quit the execution of the current state.

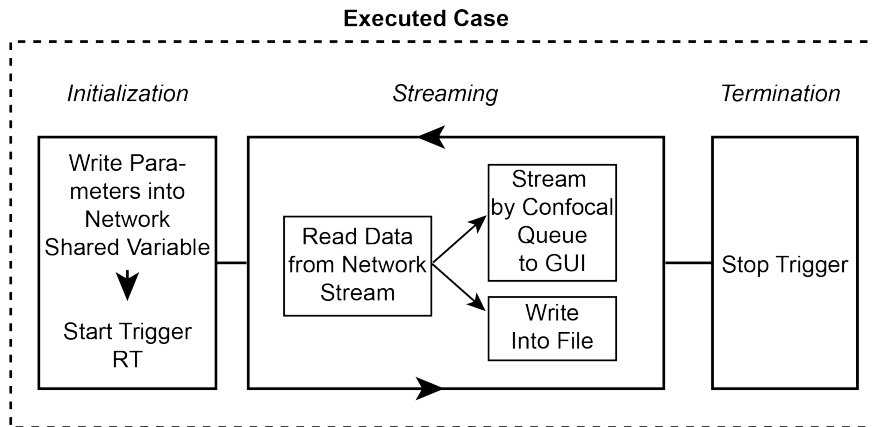


**Figure 5.8:** Main execution steps of the *Data Stream Module* during data acquisition. After receiving a data acquisition command from the Visualization Module, the corresponding case of the state machine is executed. First, the required parameters are updated on the RT unit via network shared variables followed by a start trigger. Then, the streaming loop is executed that reads data from the network stream, writes it into the corresponding data file and streams the values to the currently active GUI of the *Visualization Module*. After data acquisition, a stop trigger is sent to the RT target.

## 5.2 Software Description: The RT Target

The software on the RT unit, a cRIO-9074, is implemented as an executable. After launching the measurement software on the non-deterministic unit, the executable leaves the stand-by mode and loads the corresponding bitfile onto the FPGA. This initializes the program on the chip. The code of the executable consists of two independent blocks, the *Modulation State Machine* and the *Acquisition State Machine*, that run in parallel. The state machine diagrams are provided in figure 5.9(a) and 5.9(b), respectively.

The *Modulation State Machine* consists of four states and is responsible for the modulated signal generation for the laser and the LIA. After initialization, it waits in the *Idle* state until it receives a trigger for *Analog Modulation* or *Digital Modulation*. Currently, the *Analog Modulation* is unused and can be programmed in the future, if needed. In the *Digital Modulation* state, the parameters are read from the network shared variable and updated on the FPGA, which is then triggered by a start command to execute the generation of the modulated signal. The state machine stays in this state until it receives a stop trigger from the non-deterministic unit. It then terminates the signal generation on the FPGA and switches back to the *Idle* state, waiting for the next start trigger. When closing the program on the non-deterministic unit, it executes the shut down procedure of the state machine in the *Stop* state.

The *Acquisition State Machine* state machine is responsible for receiving the acquired data from the FPGA and transferring it to the non-deterministic unit. It consists of eight states. After receiving the start trigger, the *Init* state is executed that establishes a network stream to the non-deterministic unit. After that, it switches to the *Idle* state and waits to receive execution commands for one of the remaining six states. In general,

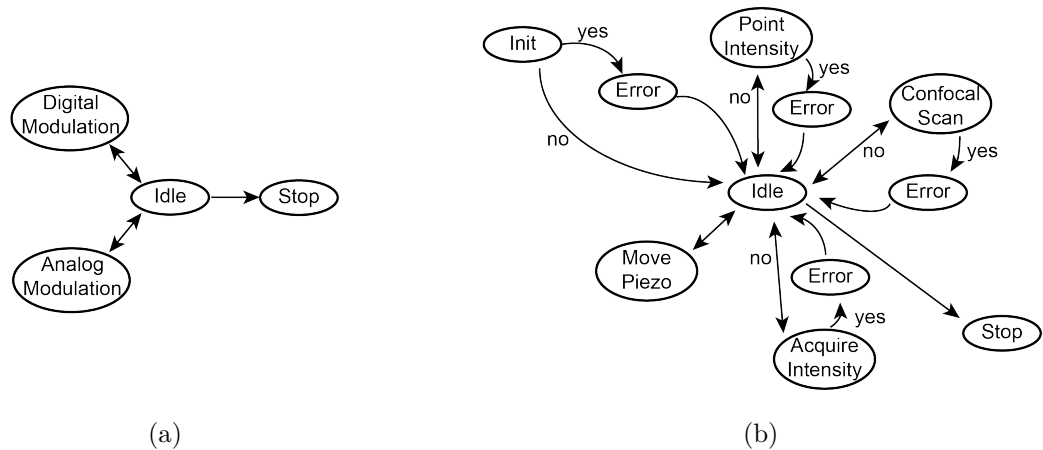


**Figure 5.9: State machines of the SRS software implemented on the RT unit.** (a) The Beam Modulation State Machine manages the generation of the modulated TTL signal. (b) The Data Acquisition State Machine schedules all different data acquisition modes.

the execution of the state specific code can be categorized into three steps that are listed below:

1. Initialization
2. Code execution
3. Termination on FPGA

In step one, the required data is read from the network shared variable *Acquisition Loop Variables* and updated on the FPGA. During step two, the state specific code is executed until terminated. In the third step, the execution on the FPGA is terminated. The remaining six states will be discussed below in detail.

### 5.2.1 Move Piezo

This state is executed when the piezo stage is moved by the operator in the SRS Scan GUI as explained on page 66. The corresponding parameters are sent to the FPGA, which applies the voltages on the stage controller. Afterwards, the state machine switches back to *Idle*.

### 5.2.2 Point Intensity

The *Point Intensity* state is executed during spectrum acquisition carried out by the *Measure Spectrum Module* of the non-deterministic unit described on page 68. Every time the step motor of the laser's delay stage shall be moved to a new position, a trigger for this state is sent to the RT unit. The corresponding acquisition time is updated on the FPGA, which is then sampling the data. As soon as the data is available in

the FIFO, the buffer is read out and the data is transferred via network stream to the non-deterministic unit. Further details regarding data transfer from the FPGA to the RT processor is given in section 4.1. Afterwards, the state machine switches back to the *Idle* state.

### 5.2.3 Acquire Intensity

The non-deterministic unit sends a trigger for the execution of this state when the operator starts the data acquisition in the corresponding GUI described on page 66. After receiving and updating the required measurement parameters on the FPGA, the execution of the corresponding code logic is triggered. In the next step, a while loop is started that constantly reads the acquired data from the FIFO, when available, and writes it into the network stream for the transfer to the non-deterministic unit. This is carried out until the operator terminates the data acquisition in the GUI, which sends a stop trigger to this state. This stop trigger is further transferred to the FPGA. After this, the state machine goes back to the *Idle* state.

### 5.2.4 Confocal Scan

The state machine switches to the *Confocal Scan* state when a SRS scan is started on the non-deterministic unit (page 66). After the update of all required parameters on the FPGA, a while loop is executed that reads the data for each pixel from the FIFO and sends it via the network stream to the non-deterministic unit. The loop execution is either stopped the data of all pixels within the image(s) is received from the FPGA or when the operator terminates the scan in the GUI. In the later case, the stop trigger is also sent to the FPGA. The state machine then switches to the *Idle* state.

### 5.2.5 Error

Whenever an error occurs during the execution of the presented states, the processes are terminated and the state machine automatically switches to the *Error* state, which receives the error and reads it out to inform the operator. The error is cleared and the state machine goes back to *Idle* in order to start a new attempt for data acquisition.

### 5.2.6 Stop

The *Stop* state is executed when the user quits the program on the non-deterministic unit. In this state, the network stream is destroyed, the bit file is flushed from the FPGA and the execution of the state machine is terminated.

### 5.3 Implementation: Field Programmable Gate Array

Analogous to the implemented code on the RT, the software on the FPGA level consists of two independent state machines illustrated in figure 5.10. Compared to the state machines on the RT, they are less complex in design, which results in a lower amount of states. The *Modulation State Machine* (figure 5.10(a)) consists of three states: *Idle*, *Analog Modulation* and *Digital Modulation*. When loading the compiled bitfile onto the FPGA, the state machine is launched in the *Idle* state and waits for triggers. As mentioned for the RT target (page 73), the *Analog Modulation* state is currently not in use. The *Digital Modulation* state is executed upon receiving the start trigger from the RT processor. After updating all required variables, a wait function is called with the defined delay time (it has no effect when the delay time is set to zero) and the defined voltage is applied on the AOM in the laser before the modulation loop is executed. This is a single-cycle timed loop with a clock rate of 40 MHz (further details are given in subsection 4.1.3). This loop generates TTL pulses with the frequency that is defined by the operator in the *Beam Modulation* GUI discussed in subsection 5.1.3. The modulation loop is terminated by a stop trigger. Afterwards, the TTL output is disabled and 0 V is applied to the AOM. The state machine then switches back to the *Idle* state.

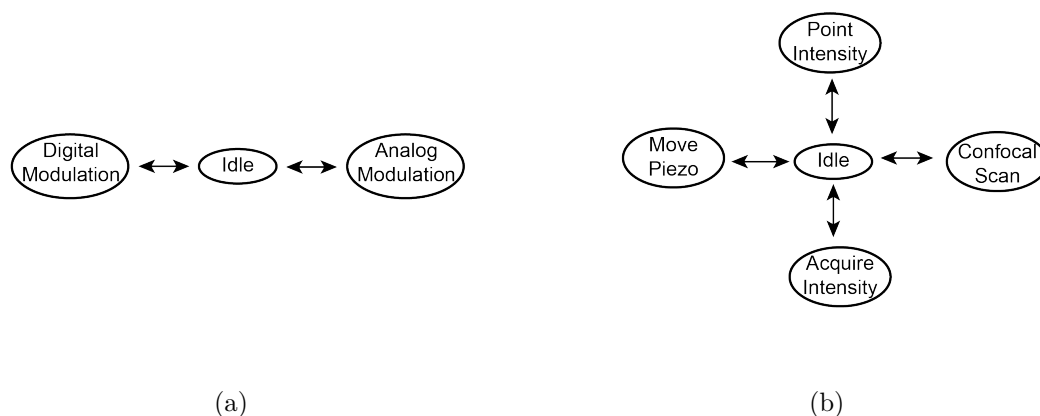


**Figure 5.10: State machines of the SRS software implemented on the FPGA.** The state machines are less complex compared to the state machines of the RT unit. (a) The Beam Modulation State Machine manages the generation of the modulated TTL signal. (b) The Data Acquisition State Machine schedules all different data acquisition modes.

The *Acquisition State Machine* (figure 5.10(b)) of the FPGA consists of five states and is also initialized in the *Idle* state when the bitfile is loaded onto the chip. The algorithm in all states, except for the *Move Piezo* state, can be categorized into three steps:

- Parameter Update
- Data Acquisition
- Data Transfer

A detailed description of the states will be given in the following.

### 5.3.1 Move Piezo

This state is executed when triggered by the user in the SRS Scan GUI discussed on page 66. After updating the corresponding parameters, the NI 9263 module, listed in table 5.1, applies the new voltages to the controller of the piezo stage. Afterwards, the state machine goes back to the *Idle* state.

### 5.3.2 Point Intensity

This state is performed during during the acquisition of a SRS spectrum and obeys the same execution pattern as described on page 74. After parameter update, two loops are started. The first loop reads the analog signal from the NI 9215 module, listed in table 5.1, for every iteration and adds the values. The stop condition of this loop is controlled by the second one, a single-cycle timed loop. This loop automatically terminates when reaching the defined bin time and stops the acquisition loop. In the next step, the average voltage is calculated as

$$\bar{V} = \frac{\sum_{i=0}^n V_i}{n} \quad (5.1)$$

where  $V_i$  is the sampled voltage at loop iteration  $i$  and  $n$  is the number of total iterations. The value is then transferred by a FIFO to the RT unit. The state machine switches then back to the *Idle* state.

### 5.3.3 Acquire Intensity

The state machine is sent to this state when the data acquisition in the in the *Acquire Intensity* GUI described on page 66 is started. First, the corresponding parameters are updated. Next, an acquisition loop that executes the same logic as described above is started. This loop is active until it receives a stop trigger from the RT unit. Afterwards, the state machine goes back to the *Idle* state.

### 5.3.4 Confocal Scan

When a SRS scan is started in the corresponding GUI (discussed on page 66), the state machine switches to this state. After initialization of the parameters, the scanning routine starts, which consists of three nested loops listed in table 5.5. Several attributes exist such as an *Abort Trigger*, a *Loop Counter* and the *Position Update*, which are common for each loop as illustrated in figure 5.11. The *Abort Trigger*, which is initiated by the operator in the SRS Scan GUI, terminates the data acquisition before the scan has finished. In the *Line Scan Loop*, the piezo stage is moved on the corresponding axis pixel by pixel and the signal sampled using the same algorithm as explained before in the *Point Intensity* state. The *Loop Counter* automatically terminates this loop when

**Table 5.5:** Names and corresponding tasks of the nested loops within the scanning routine.

Loop Name	Task
Line Scan	Horizontal position update in scan and data acquisition for each pixel on the current line
Number of Lines	Vertical position update in scan for the next line
Frame/Axial	Position update in third dimension (when range is greater than zero) and number of frames counter

the execution cycle is equal to the number of defined pixels for the scan. The step size is calculated from the scan range and number of pixels. The *Number of Lines Loop* triggers the execution of the *Line Scan Loop*. After each complete line scan, the *Number of Lines Loop* moves the piezo to the new start position of the next line on the defined axis. After this, a *Line Trigger* is sent as a TTL pulse to the TCSPC card. This trigger is necessary for reconstructing the corresponding image from the photon arrival times. A new line scan is then started. This loop automatically terminates when its loop counter is equal to the execution cycle, which corresponds to a fully scanned image. In case of a series of image scans, the *Axial/Position Loop* automatically triggers the start of a new image scan. When a range for a 3D stack is defined, the piezo stage is first moved on the corresponding axis to the new position. Then, a *Frame Marker*, which indicates the start of a new image is sent to the TCSPC card followed by the start of the *Number of Lines Loop*. When the execution cycle of this loop is equal to the loop counter, it is terminated and the scan routine completed. The state machine is then switched back to the *Idle* state.



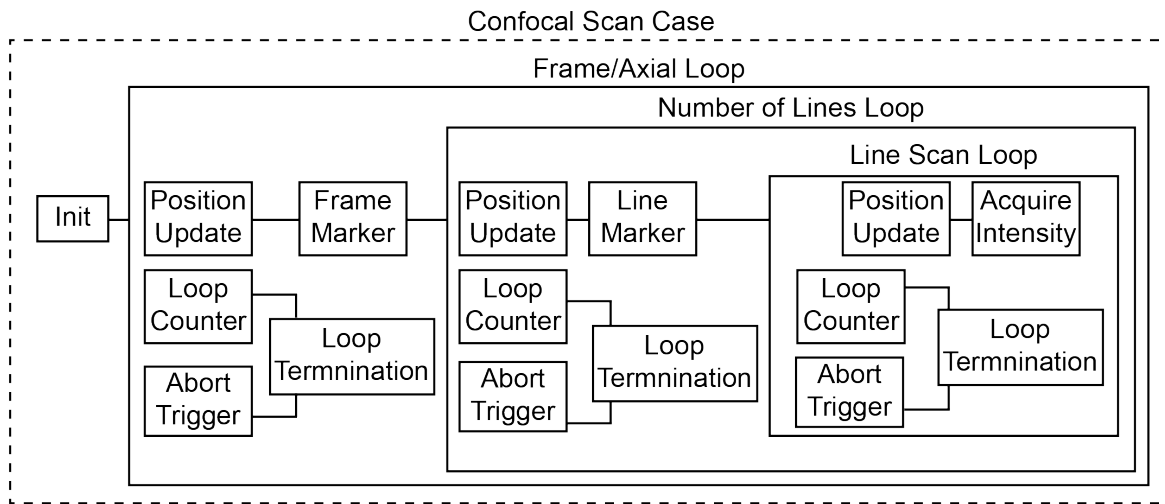


**Figure 5.11: Simplified scheme of the implemented scanning routine.** It consists of three nested while loops, each controlling an axis of the piezo stage. Every loop either terminates automatically when the corresponding loop counter is equal to the execution cycle or when the scan is terminated by the operator. The *Line Scan Loop* moves the piezo stage pixel by pixel horizontally on the image. After each position update, data is acquired with the same logic as explained for the *Point Intensity* state on page 77. This loop is further controlled by the *Number of Lines Loop*. After the vertical position is updated on the image, a line marker is sent to the TCSPC card before the next line scan is carried out. When the defined number of lines are scanned, the data acquisition of the image is complete. The *Frame/Axial Loop* coordinates the acquisition of a (3D) set of images. In the event that a third dimension is scanned, the position on the corresponding axis is updated on the piezo stage. A frame marker is then sent to the TCSPC card and the next image scan is triggered.

## **5.4 Software Proof of Concept on Graphene**

With its outstanding physical properties, graphene is highly interesting as a material as well as in life sciences for single molecule applications. Since the physical properties strongly depend on the number of graphene layers, it is mandatory to benchmark the material before any further assay and experiment. Due to the linear behavior of the scattering intensity of SRS, different amounts of single graphene layers can be easily identified by the ratio of two bands in the spectrum. Figures 5.12 and 5.13 show example data acquired by the newly developed software. The first image contains a widefield image (subpanel 5.12(a)), a SRS (subpanel 5.12(b)) and acquired spectra (subpanel 5.12(c)) of the same FOV. While graphene is hardly recognized in the widefield image, the scan clearly reveals areas with graphene of different amounts of layers indicated by the variety of intensities. As explained on page 68, spectra were measured after scanning the FOV in automatic mode. As expected from the different areas of varying intensities, the ratio of the two graphene bands on those areas vary when comparing to each other, further proving the existence of different numbers of graphene layers. Scans were repeated on a different sample in the combined SRS/TCSPC mode illustrated in figure 5.13. The image acquired by TCSPC logic (panel (5.13(b))) perfectly matches with the scattered image (panel (5.13(c))). Furthermore, the trend is in line with figure 5.12 where areas of different intensities show different spectra. Interestingly, in some areas, the material tends to coil up or have defects indicated by very high intensities on very small areas. With these preliminary experiments, a successful implementation of the software for acquiring simultaneous SRS and TCSPC data with the option of spectrum acquisition is shown.

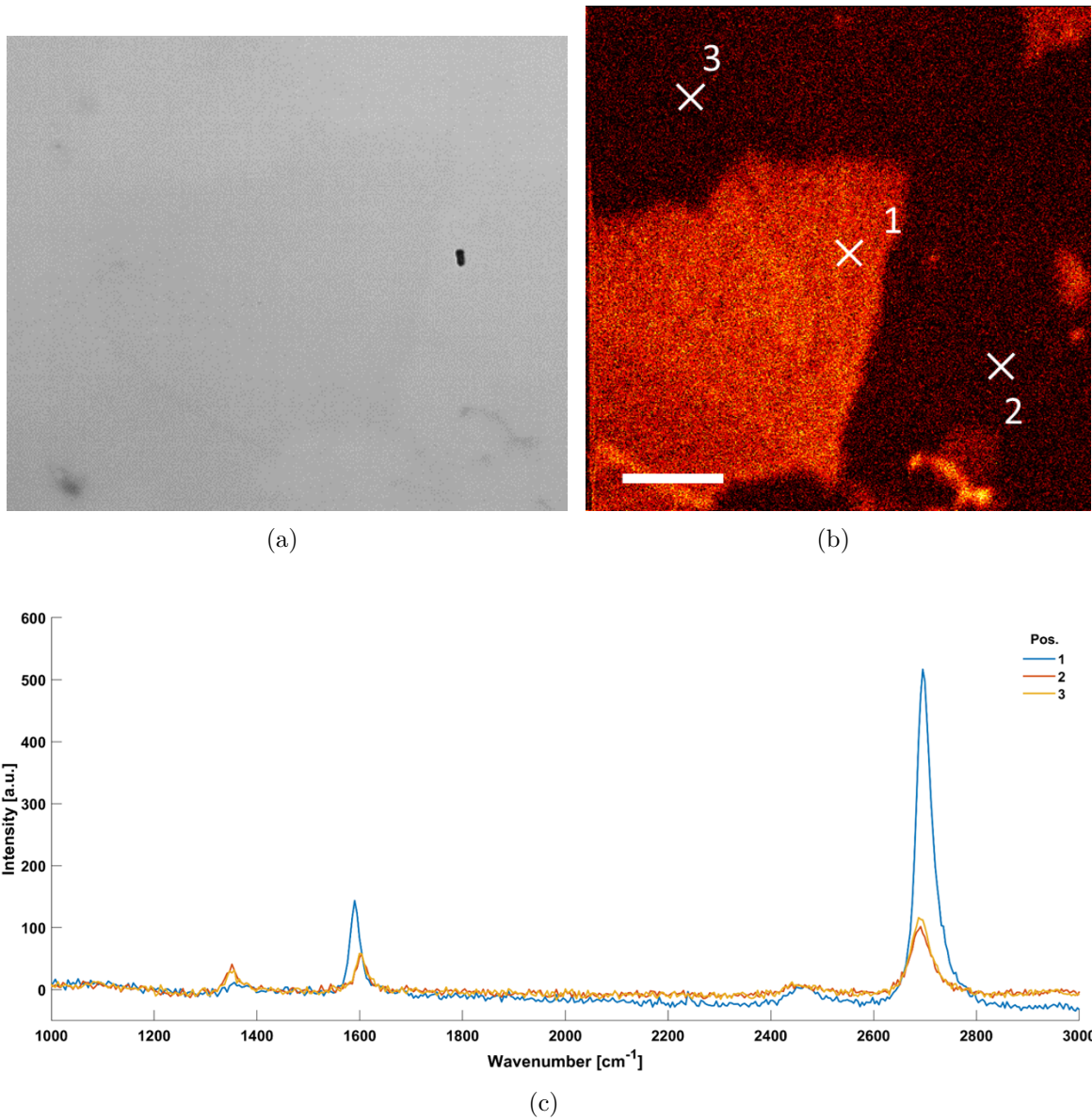


**Figure 5.12: Images and spectra of graphene obtained by the novel SRS software.** (a) Widefield image of the sample. (b) SRS scan. (c) SRS spectra taken at different positions of the FOV in (b). Samples provided by Lars Richter (AK Tinnefeld); measurements carried out together with Fabian Knechtel (AK Lamb/Plöetz).

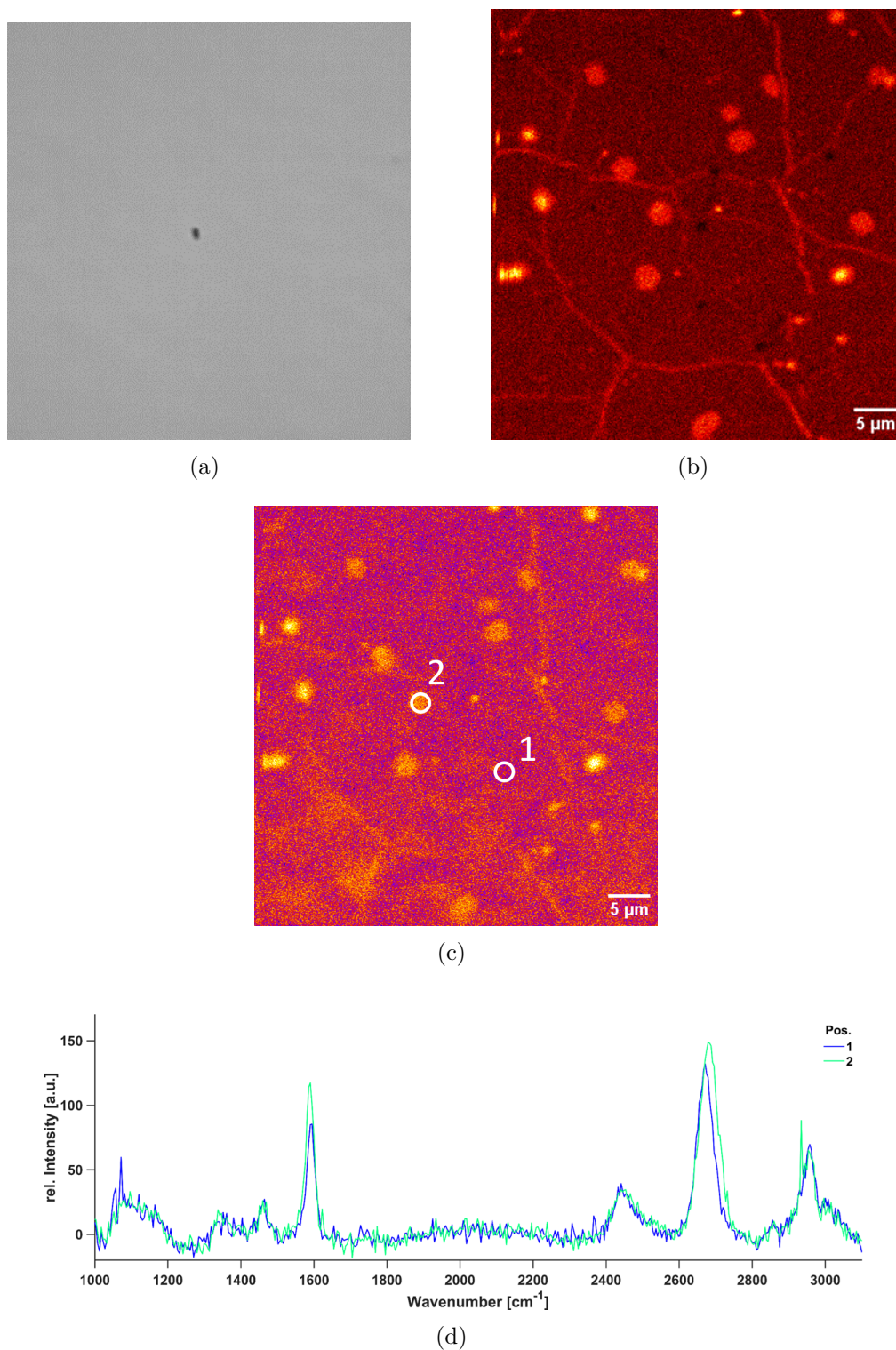


**Figure 5.13: Images and spectra of graphene obtained by the novel SRS software in combined scattering/TCSPC mode.** (a) Widefield image of the sample. (b) TCSPC scan. (c) SRS scan. (d) SRS spectra taken at different positions of the FOV in (c). Samples provided by Dr. Izabela Kaminska (AK Tinnefeld); measurements carried out by Fabian Knechtel (AK Lamb/Ploetz).

## Chapter 6

---

# Conclusion and Outlook

In this thesis, three main projects were presented:

1. impact of correlation analysis on trajectories of living zebra fish larvae
2. development of multicolor 3D Orbital Tracking Microscopy
3. software development for combined SRS scanning with parallel TCSPC readout

In the first part of this thesis, impact of a correlation analysis on interpretation of trajectories acquired in living zebra fish larvae was highlighted. By correlating the angles between two orbits along the trajectory, it is possible to distinguish between active transportation and stationary states. The big advantage of this approach is that this threshold is not globally set to a single value but is accessible by the trajectory data and can be calculated for each one individually.

With the redesign of the data acquisition software of the existing, in-house developed 3D Orbital Tracking microscope, the efficiency of data acquisition has been increased. This allows for carrying out two types of dual-color tracking experiments in solution: tracking two individual particles independently from each other and correlative motion. Here, the active feedback loop is activated in one tracking channel while the presence of the second particle is probed in the second channel with deactivated feedback loop. In the next step, the software was extended for carrying out tracking experiments with simultaneous, live probing of FRET in solution by alternating the corresponding excitation lasers. With the novel OPSPC algorithm, photons emitted from the FRET pair are tagged and detected with 40 MHz time resolution. This tagging allows for the reconstruction all fluorescence intensity traces of the dye pair. In a post-processing step, the intensities can be corrected to obtain accurate FRET values. This new software feature was demonstrated on freely diffusing beads in solution that were labeled with ATTO488 and a dsDNA containing a FRET pair. In these proof of principle experiments, different FRET distances were observed with low, intermediate and high accurate FRET efficiencies. Promising dual-color preliminary experiments were done in living HUH7 RAB5-GFP cells during endocytosis, indicating the robustness of the described tracking modalities for performing experiments in living cells. With the successful proof of concept experiments for combined tracking and FRET, the time resolution of detected FRET photons can further be increased by upgrading the system with TCSPC electronics and pulsed excitation sources, allowing the detection of fast dynamics in the

investigated system. Additionally, it will give access to lifetime information of fluorophores. The corresponding TTL signals arising from the OPSPC algorithm can be used as photon markers for the TCSPC cards, which can then measure the photon arrival times without interrupting the tracking algorithm. Due to the QMH design of the data acquisition software, the implementation of these cards is relatively easy to handle. The third part of this thesis highlights the software development of a data acquisition program for scanning SRS images and automated acquisition of spectra at selected points in an image. Scans can further be combined with single-photon-counting detection arising from photoluminescence using TCSPC electronics. This allows for simultaneous imaging of SRS and two photon-counting channels during the same scan. An example implementation of this software was the investigation of sample quality of graphene. Due to the QMH design of the program, the software could be extended in the future by the implementation of Orbital Tracking features on the SRS channel. This would be the first label-free SPT approach using the Orbital Tracking technique.

All in all, highly sensitive instruments, which can be nowadays purchased in a ready to use soft- and hardware bundle from suppliers out of the shelf, already obtain extraordinary data. However, the executed software is often not capturing the maximum performance of the hardware. Additionally, those bundles can normally not be modified by the end user, limiting the flexibility of usage. In-house developed instruments can tackle these problems. Great care has to be taken not only in choosing the correct electronic devices, but also in planning and developing a proper software for it. While the first part is fairly straightforward, software development is normally more challenging. It is true that coding small applications is fast in the beginning, often leading to a loss of focus on software design. With the implementation of further features, the complexity of the software increases, which can then result in an “organic grown”, unhandy program. Hence, when developing highly sensitive instruments, it should always be kept in mind, that the best hardware never works without the appropriate software and vice versa.

# Bibliography

- Abbe, E. (1873). “Beiträge zur Theorie des Mikroskops und der mikroskopischen Wahrnehmung”. In: *Archiv für mikroskopische Anatomie* 9, pp. 413–468.
- Annibale, P., A. Dvornikov, and E. Gratton (2015). “Electrically tunable lens speeds up 3D orbital tracking”. In: *Biomed Opt Express* 6.6, pp. 2181–90.
- Balzarotti, Francisco, Yvan Eilers, Klaus C. Gwosch, Arvid H. Gynnå, Volker Westphal, Fernando D. Stefani, Johan Elf, and Stefan W. Hell (2017). “Nanometer resolution imaging and tracking of fluorescent molecules with minimal photon fluxes”. In: *Science* 355.6325, p. 606.
- Baros, Jan, Radek Martinek, Rene Jaros, Lukas Danys, and Lukas Soustek (2019). “Development of application for control of SMART parking lot”. In: *IFAC-PapersOnLine* 52.27, pp. 19–26.
- Bartnik, Kira, Anders Barth, Mauricio Pilo-Pais, Alvaro H. Crevenna, Tim Liedl, and Don C. Lamb (2020). “A DNA Origami Platform for Single-Pair Förster Resonance Energy Transfer Investigation of DNA–DNA Interactions and Ligation”. In: *Journal of the American Chemical Society* 142.2, pp. 815–825.
- Berg, Howard C. (1971). “How to Track Bacteria”. In: *Review of Scientific Instruments* 42.6, pp. 868–871.
- Berland, K. M., P. T. So, and E. Gratton (1995). “Two-photon fluorescence correlation spectroscopy: method and application to the intracellular environment”. In: *Biophysical journal* 68.2, pp. 694–701.
- Betzig, Eric, George H. Patterson, Rachid Sougrat, O. Wolf Lindwasser, Scott Olenych, Juan S. Bonifacino, Michael W. Davidson, Jennifer Lippincott-Schwartz, and Harald F. Hess (2006). “Imaging Intracellular Fluorescent Proteins at Nanometer Resolution”. In: *Science* 313.5793, pp. 1642–1645.
- Bloembergen, N. (1967). “The Stimulated Raman Effect”. In: *American Journal of Physics* 35.11, pp. 989–1023.
- Born, M. and R. Oppenheimer (1927). “Zur Quantentheorie der Molekeln”. In: *Annalen der Physik* 389.20, pp. 457–484.
- Cooley, J. W. and J. V. Tukey (1965). “An algorithm for the machine calculation of complex Fourier series”. In: *Mathematics of Computation* 19.90, p. 297.
- Dickson, Robert M., Andrew B. Cubitt, Roger Y. Tsien, and W. E. Moerner (1997). “On/off blinking and switching behaviour of single molecules of green fluorescent protein”. In: *Nature* 388.6640, pp. 355–358.
- Elbert, D L and J A Hubbell (1996). “Surface Treatments of Polymers for Biocompatibility”. In: *Annual Review of Materials Science* 26.1, pp. 365–394.
- Enderlein, J. (2000). “Tracking of fluorescent molecules diffusing within membranes”. In: *Applied Physics B* 71.5, pp. 773–777.

- Enderlein, Jörg (1995). “Maximum-likelihood criterion and single-molecule detection”. In: *Applied Optics* 34.3, pp. 514–526.
- Felekyan, S., R. Kühnemuth, V. Kudryavtsev, C. Sandhagen, W. Becker, and C. A. M. Seidel (2005). “Full correlation from picoseconds to seconds by time-resolved and time-correlated single photon detection”. In: *Review of Scientific Instruments* 76.8, p. 083104.
- Fleischmann, M., P. J. Hendra, and A. J. McQuillan (1974). “Raman spectra of pyridine adsorbed at a silver electrode”. In: *Chemical Physics Letters* 26.2, pp. 163–166.
- Forster, Th (1946). “Energiewanderung und Fluoreszenz”. In: *Naturwissenschaften* 33.6, pp. 166–175.
- Fourier, Jean Baptiste Joseph (1822). *Theorie analytique de la chaleur*.
- Freudiger, Christian W., Wei Min, Brian G. Saar, Sijia Lu, Gary R. Holtom, Chengwei He, Jason C. Tsai, Jing X. Kang, and X. Sunney Xie (2008). “Label-Free Biomedical Imaging with High Sensitivity by Stimulated Raman Scattering Microscopy”. In: *Science* 322.5909, p. 1857.
- Fuchs, Adrian, Petra Mannhardt, Patrick Hirschle, Haoze Wang, Irina Zaytseva, Zhe Ji, Omar Yaghi, Stefan Wuttke, and Evelyn Ploetz (2022). “Single Crystals Heterogeneity Impacts the Intrinsic and Extrinsic Properties of Metal–Organic Frameworks”. In: *Advanced Materials* 34.3, p. 2104530.
- Förster, Theodor (1948). “Zwischenmolekulare Energiewanderung und Fluoreszenz”. In: *Annalen der Physik* 437.1-2, pp. 55–75.
- Hell, Stefan W. and Jan Wichmann (1994). “Breaking the diffraction resolution limit by stimulated emission: stimulated-emission-depletion fluorescence microscopy”. In: *Opt. Lett.* 19.11, pp. 780–782.
- Herschel, John Frederick William (1845). “‘Ao No. I. On a Case of Superficial Colour Presented by a Homogeneous Liquid Internally Colourless”. In: *Philosophical Transactions of the Royal Society of London* 135, pp. 143–145.
- Hou, Shangguo, Xiaoqi Lang, and Kevin Welsher (2017). “Robust real-time 3D single-particle tracking using a dynamically moving laser spot”. In: *Optics Letters* 42.12, pp. 2390–2393.
- Jablonski, A. (1935). “Über den Mechanismus der Photolumineszenz von Farbstoffphosphoren”. In: *Zeitschrift für Physik* 94.1, pp. 38–46.
- Kapanidis, Achillefs N., Ted A. Laurence, Nam Ki Lee, Emmanuel Margeat, Xiangxu Kong, and Shimon Weiss (2005). “Alternating-Laser Excitation of Single Molecules”. In: *Accounts of Chemical Research* 38.7, pp. 523–533.
- Kapanidis, Achillefs N., Nam Ki Lee, Ted A. Laurence, Sören Doose, Emmanuel Margeat, and Shimon Weiss (2004). “Fluorescence-aided molecule sorting: Analysis of structure and interactions by alternating-laser excitation of single molecules”. In: *Proceedings of the National Academy of Sciences of the United States of America* 101.24, pp. 8936–8941.
- Kasha, Michael (1950). “Characterization of electronic transitions in complex molecules”. In: *Discussions of the Faraday Society* 9.0, pp. 14–19.



- Katayama, Yoshihiko, Ondrej Burkacky, Martin Meyer, Christoph Bräuchle, Enrico Gratton, and Don C. Lamb (2009). “Real-Time Nanomicroscopy via Three-Dimensional Single-Particle Tracking”. In: *ChemPhysChem* 10.14, pp. 2458–2464.
- Keller, Aaron M., Matthew S. DeVore, Dominik G. Stich, Dung M. Vu, Timothy Causgrove, and James H. Werner (2018). “Multicolor Three-Dimensional Tracking for Single-Molecule Fluorescence Resonance Energy Transfer Measurements”. In: *Analytical Chemistry* 90.10, pp. 6109–6115.
- Kis-Petikova, Katarina and Enrico Gratton (2004). “Distance measurement by circular scanning of the excitation beam in the two-photon microscope”. In: *Microscopy Research and Technique* 63.1, pp. 34–49.
- Kudryavtsev, Volodymyr, Martin Sikor, Stanislav Kalinin, Dejana Mokranjac, Claus A. M. Seidel, and Don C. Lamb (2012). “Combining MFD and PIE for Accurate Single-Pair Förster Resonance Energy Transfer Measurements”. In: *ChemPhysChem* 13.4, pp. 1060–1078.
- Lamichhane, Rajan, Amanda Solem, Will Black, and David Rueda (2010). “Single-molecule FRET of protein-nucleic acid and protein-protein complexes: surface passivation and immobilization”. In: *Methods (San Diego, Calif.)* 52.2, pp. 192–200.
- Lerner, Eitan, Evelyn Ploetz, Johannes Hohlbein, Thorben Cordes, and Shimon Weiss (2016). “A Quantitative Theoretical Framework For Protein-Induced Fluorescence Enhancement–Förster-Type Resonance Energy Transfer (PIFE-FRET)”. In: *The Journal of Physical Chemistry B* 120.26, pp. 6401–6410.
- Lessard, Guillaume A., Peter M. Goodwin, and James H. Werner (2007). “Three-dimensional tracking of individual quantum dots”. In: *Applied Physics Letters* 91.22, p. 224106.
- Levi, V., Q. Ruan, K. Kis-Petikova, and E. Gratton (2003). “Scanning FCS, a novel method for three-dimensional particle tracking”. In: *Biochemical Society Transactions* 31.5, pp. 997–1000.
- Liu, Yen-Liang, Evan P. Perillo, Phyllis Ang, Mirae Kim, Duc Trung Nguyen, Katherine Blocher, Yu-An Chen, Cong Liu, Ahmed M. Hassan, Huong T. Vu, Yuan-I. Chen, Andrew K. Dunn, and Hsin-Chih Yeh (2020). “Three-Dimensional Two-Color Dual-Particle Tracking Microscope for Monitoring DNA Conformational Changes and Nanoparticle Landings on Live Cells”. In: *ACS Nano* 14.7, pp. 7927–7939.
- Lynch, Nancy and M. R. Tuttle (1989). “An introduction to input/output automata”. In: *CWI Quarterly* 2.3, pp. 219–246.
- Masullo, Luciano A., Florian Steiner, Jonas Zähringer, Lucía F. Lopez, Johann Bohlen, Lars Richter, Fiona Cole, Philip Tinnefeld, and Fernando D. Stefani (2021). “Pulsed Interleaved MINFLUX”. In: *Nano Letters* 21.1, pp. 840–846.
- Mazzaferri, Javier, Joannie Roy, Stephane Lefrancois, and Santiago Costantino (2014). “Adaptive settings for the nearest-neighbor particle tracking algorithm”. In: *Bioinformatics* 31.8, pp. 1279–1285.
- Minsky, Marvin (1961). *Microscopy apparatus*. Patent.
- Müller, Barbara K., Evgeny Zaychikov, Christoph Bräuchle, and Don C. Lamb (2005). “Pulsed Interleaved Excitation”. In: *Biophysical Journal* 89.5, pp. 3508–3522.
- Nehme, Elias, Daniel Freedman, Racheli Gordon, Boris Ferdman, Lucien E. Weiss, Onit Alalouf, Tal Naor, Reut Orange, Tomer Michaeli, and Yoav Shechtman (2020). “Deep-

- STORM3D: dense 3D localization microscopy and PSF design by deep learning”. In: *Nature Methods* 17.7, pp. 734–740.
- Olivo-Marin, Jean-Christophe (2002). “Extraction of spots in biological images using multiscale products”. In: *Pattern Recognition* 35.9, pp. 1989–1996.
- Pavani, Sri Rama Prasanna, Michael A. Thompson, Julie S. Biteen, Samuel J. Lord, Na Liu, Robert J. Twieg, Rafael Piestun, and W. E. Moerner (2009). “Three-dimensional, single-molecule fluorescence imaging beyond the diffraction limit by using a double-helix point spread function”. In: *Proceedings of the National Academy of Sciences* 106.9, pp. 2995–2999.
- Penzkofer, A., A. Laubereau, and W. Kaiser (1979). “High intensity Raman interactions”. In: *Progress in Quantum Electronics* 6.2, pp. 55–140.
- Perillo, Evan P., Yen-Liang Liu, Khang Huynh, Cong Liu, Chao-Kai Chou, Mien-Chieh Hung, Hsin-Chih Yeh, and Andrew K. Dunn (2015). “Deep and high-resolution three-dimensional tracking of single particles using nonlinear and multiplexed illumination”. In: *Nature Communications* 6.1, p. 7874.
- Planck, Max Karl Ernst Ludwig (1900). “Zur Theorie des Gesetzes der Energieverteilung im Normalspectrum”. In: *Verhandl. Dtsch. Phys. Ges.* 2, p. 237.
- Ploetz, E., S. Laimgruber, S. Berner, W. Zinth, and P. Gilch (2007). “Femtosecond stimulated Raman microscopy”. In: *Applied Physics B* 87.3, pp. 389–393.
- Pérez-Jiménez, Ana Isabel, Danya Lyu, Zhixuan Lu, Guokun Liu, and Bin Ren (2020). “Surface-enhanced Raman spectroscopy: benefits, trade-offs and future developments”. In: *Chemical science* 11.18, pp. 4563–4577.
- Qian, Chen, Annica Flemming, Barbara Müller, and Don C. Lamb (2022). “Dynamics of HIV-1 Gag Processing as Revealed by Fluorescence Lifetime Imaging Microscopy and Single Virus Tracking”. In: *Viruses* 14.2, p. 340.
- Raman, C. V. and K. S. Krishnan (1928). “The Optical Analogue of the Compton Effect”. In: *Nature* 121.3053, pp. 711–711.
- Rust, Michael J., Mark Bates, and Xiaowei Zhuang (2006). “Sub-diffraction-limit imaging by stochastic optical reconstruction microscopy (STORM)”. In: *Nat. Methods* 3.10, pp. 793–796.
- Schrimpf, Waldemar, Anders Barth, Jelle Hendrix, and Don C. Lamb (2018). “PAM: A Framework for Integrated Analysis of Imaging, Single-Molecule, and Ensemble Fluorescence Data”. In: *Biophysical Journal* 114.7, pp. 1518–1528.
- Shechtman, Yoav, Lucien E. Weiss, Adam S. Backer, Steffen J. Sahl, and W. E. Moerner (2015). “Precise Three-Dimensional Scan-Free Multiple-Particle Tracking over Large Axial Ranges with Tetrapod Point Spread Functions”. In: *Nano Letters* 15.6, pp. 4194–4199.
- Shimomura, Osamu, Frank H. Johnson, and Yo Saiga (1962). “Extraction, Purification and Properties of Aequorin, a Bioluminescent Protein from the Luminous Hydromedusa, *Aequorea*”. In: *Journal of Cellular and Comparative Physiology* 59.3, pp. 223–239.
- Smit, Jochem H., Jasper H. M. van der Velde, Jingyi Huang, Vanessa Trauschke, Sarah S. Henrikus, Si Chen, Nikolaos Eleftheriadis, Eliza M. Warszawik, Andreas Herrmann, and Thorben Cordes (2019). “On the impact of competing intra- and intermolecu-

- lar triplet-state quenching on photobleaching and photoswitching kinetics of organic fluorophores”. In: *Physical Chemistry Chemical Physics* 21.7, pp. 3721–3733.
- Speidel, Michael, Alexandr Jonáš, and Ernst-Ludwig Florin (2003). “Three-dimensional tracking of fluorescent nanoparticles with subnanometer precision by use of off-focus imaging”. In: *Optics Letters* 28.2, pp. 69–71.
- Stokes, G. G. (1852). “On the Change of Refrangibility of Light”. In: *Philosophical Transactions of the Royal Society of London* 142, pp. 463–562.
- Strutt, J. W. (1871). “XV. On the light from the sky, its polarization and colour”. In: *The London, Edinburgh, and Dublin Philosophical Magazine and Journal of Science* 41.271, pp. 107–120.
- Szkop, Michał, Beata Kliszcz, and Andrzej A. Kasprzak (2018). “A simple and reproducible protocol of glass surface silanization for TIRF microscopy imaging”. In: *Analytical Biochemistry* 549, pp. 119–123.
- Tittel, Jonas, Fabian Knechtel, and Evelyn Ploetz (2023). “Conquering Metal–Organic Frameworks by Raman Scattering Techniques”. In: *Advanced Functional Materials* n/a.n/a, p. 2307518.
- Wehnekamp, Fabian (2016). “3D Orbital Tracking Microscopy: From Cells To Organisms”. Thesis.
- Wehnekamp, Fabian, Gabriela Plucińska, Rachel Thong, Thomas Misgeld, and Don C. Lamb (2019). “Nanoresolution real-time 3D orbital tracking for studying mitochondrial trafficking in vertebrate axons in vivo”. In: *eLife* 8, e46059.
- Widengren, Jerker, Volodymyr Kudryavtsev, Matthew Antonik, Sylvia Berger, Margarita Gerken, and Claus A. M. Seidel (2006). “Single-Molecule Detection and Identification of Multiple Species by Multiparameter Fluorescence Detection”. In: *Analytical Chemistry* 78.6, pp. 2039–2050.
- Zumbusch, Andreas, Gary R. Holtom, and X. Sunney Xie (1999). “Three-Dimensional Vibrational Imaging by Coherent Anti-Stokes Raman Scattering”. In: *Physical Review Letters* 82.20, pp. 4142–4145.



# List of Abbreviations

**2D** two dimensional

**3D** three dimensional

**AFM** atomic force microscopy

**ALEX** alternated laser excitation

**AOTF** acousto-optic tunable filter

**AOM** acousto-optic modulator

**APD** avalanche photodiode

**AV** accessible volume

**BS** beam splitter

**CARS** Coherent Anti-Stokes Raman Scattering

**CMOS** complementary metal-oxide-semiconductor

**CPU** central processing unit

**cryoEM** cryo electron microscopy

**cw** continuous wave

*List of Abbreviations*

**DLL** dynamic link library

**DM** dichroic mirror

**DMA** direct memory access

**DNA** deoxyribonucleic acid

**ds** double stranded

**EMCCD** electron multiplying charge-coupled device

**EOD** electro-optical deflector

**FFT** fast Fourier transformation

**FIFO** first in - first out

**FPGA** field programmable gate array

**FRET** Förster Resonance Energy Transfer

**FOV** field-of-view

**FXP** fixed-point

**GFP** green fluorescent protein

**GUI** graphical user interface

**HMI** human machine interface

**LabVIEW** Laboratory Virtual Instrumentation Engineering Workbench

**laser** light amplification by stimulated emission of radiation

**LIA** lock-in amplifier

**LUT** look-up table

**MFD** multiparameter fluorescence detection

**mRNA** messenger ribonucleic acid

**MSD** mean squared displacement

**NMR** nuclear magnetic resonance

**OPSPC** orbit point single photon counting

**PALM** photoactivated localization microscopy

**PIE** pulsed interleaved excitation

**PIFE** protein induced fluorescence enhancement

**PMT** photomultiplier tube

**PSF** point spread function

**QMH** queued message handler

**RPS** raw photon stream

*List of Abbreviations*

**RT** real time

**SERS** Surface-Enhanced Raman Scattering

**SNR** signal-to-noise ratio

**SRG** Stimulated Raman Gain

**SRL** Stimulated Raman Loss

**SRS** Stimulated Raman Scattering

**SPT** single particle tracking

**STED** Stimulated Emission Depletion

**STORM** Stochastic Optical Reconstruction Microscopy

**TAG** tunable acoustic gradient

**TCSPC** time correlated single photon counting

**TERS** Tip-Enhanced Raman Scattering

**TIR** total internal reflection

**TTL** transistor-transistor logic

**TS** target scoped

**VI** virtual instrument



# List of Figures

2.1	Absorption and emission spectra of ATTO647N. . . . .	6
2.2	Jablonski diagram. . . . .	7
2.3	Jablonski diagram illustrating the processes of FRET. . . . .	8
2.4	Jablonski diagram illustrating <i>Raman</i> scattering processes. . . . .	10
2.5	Jablonski diagram illustrating SRS on the Stokes side. . . . .	14
2.6	Principles of SRL and SRG during SRS. . . . .	14
2.7	Scheme of a confocal microscope. . . . .	16
2.8	Overview of SPT techniques using the post processing approach. . . . .	19
2.9	Instrumentation of the first feedback based SPT setup by <i>Berg</i> . . . . .	20
2.10	Overview of feedback based SPT approaches spanning the detection volume for localizing the particle of interest. . . . .	22
2.11	Overview of feedback based SPT approaches that steer the excitation beam. . . . .	23
2.12	A simulatoin of the signal coming from a fluorescent particle for different positions in the orbit. . . . .	24
2.13	Schematic for position determination of a particle in polar coordinates during an orbit. . . . .	26
2.14	3D particle localization by Orbital Tracking. . . . .	28
2.15	Sketch of the Multicolor 3D Orbital Tracking instrument used for this thesis. . . . .	30
3.1	Correlation analysis of a mitochondrial retrograde trajectory. . . . .	35
4.1	Sketch of soft- and hardware architecture. . . . .	39
4.2	Main GUI and execution hierarchy of the RT Tracker software version 5.1 . . . . .	41
4.3	General settings GUI launched by the Profile Module. . . . .	42
4.4	GUI of the Acquire Intensity subVI. . . . .	44
4.5	GUI of the PSF scan subVI. . . . .	45
4.6	GUI of the mapping subVI. . . . .	46
4.7	GUI of the tracking subVI. . . . .	48
4.8	GUI of the tracking/FRET subVI. . . . .	49
4.9	Main principle steps performed by the <i>Data Module</i> during data acquisition. . . . .	50
4.10	State machines implemented on the RT target. . . . .	52
4.11	Main principle steps of the state machine RTtarget during data acquisition. . . . .	53
4.12	State machines implemented on the FPGA. . . . .	55
4.13	Implemented laser excitation schemes for the new Tracking/FRET mode. . . . .	55
4.14	Producer-consumer design of the OPSPC approach for the Tracking/FRET state. . . . .	57
4.15	Dual color tracking of beads. . . . .	59

List of Figures

4.16	Single-molecule FRET measurements on diffusing DNA molecules. . . . .	60
5.1	Sketch of soft- and hardware architecture for the confocal microscope capable of synchronous SRS imaging and photon-based microscopy. . . . .	62
5.2	Main GUI and execution hierarchy of the SRS software. . . . .	63
5.3	General settings GUI of the SRS software. . . . .	65
5.4	GUI of the Acquire Intensity subVI. . . . .	67
5.5	SRS scan GUI of the SRS software. . . . .	69
5.6	Measure Spectrum GUI of the SRS software. . . . .	70
5.7	Beam Modulation GUI of the SRS software. . . . .	71
5.8	Main execution steps of the <i>Data Stream Module</i> during data acquisition. . .	73
5.9	State machines of the SRS software implemented on the RT unit. . . . .	74
5.10	State machines of the SRS software implemented on the FPGA. . . . .	76
5.11	Simplified scheme of the implemented scanning routine. . . . .	79
5.12	Images and spectra of graphene obtained by the novel SRS software. . . . .	81
5.13	Images and spectra of graphene obtained by the novel SRS software in combined scattering/TCSPC mode. . . . .	82

# List of Tables

2.1	Characteristics of the <i>Fourier</i> coefficients for the Orbital Tracking approach. .	27
3.1	Structure of Orbital Tracking data file including file header and data entries. .	33
4.1	Overview of modules, their tasks and types used in the QMH architecture of the RT Tracker software version 5.1. . . . .	40
4.2	Overview of the variables used in the RT Tracker software version 5.1 listed in alphabetical order. . . . .	43
4.3	Overview of subVIs, its tasks managed by the <i>Confocal Module</i> . . . . .	43
4.4	List of all implemented network streams between the deterministic and non-deterministic units. . . . .	53
4.5	Overview of multiplexed photon information stored as a U64 integer. . . . .	56
5.1	Implemented modules in the cRIO-9074 device. . . . .	61
5.2	Overview of modules, their tasks and types used in the QMH architecture of the SRS software. . . . .	64
5.3	Overview of the variables used in the SRS software listed in alphabetical order. . . . .	64
5.4	Overview of subVIs, the corresponding trigger buttons and their tasks managed by the Visualization Module. . . . .	66
5.5	Names and corresponding tasks of the nested loops within the scanning routine. . . . .	78



## **Appendix A**

---

# **Publications**

### **A.1 Trajectory data of antero- and retrograde movement of mitochondria in living zebrafish larvae**



ELSEVIER

Contents lists available at ScienceDirect

## Data in brief

journal homepage: [www.elsevier.com/locate/dib](http://www.elsevier.com/locate/dib)

## Data Article

# Trajectory data of antero- and retrograde movement of mitochondria in living zebrafish larvae



Frank Mieskes<sup>a</sup>, Fabian Wehnekamp<sup>a</sup>, Gabriela Plucińska<sup>b</sup>,  
Rachel Thong<sup>b</sup>, Thomas Misgeld<sup>b</sup>, Don C. Lamb<sup>a,\*</sup>

<sup>a</sup> Department of Chemistry, Center for Nano Science (CENS), Center for Integrated Protein Science (CIPSM), Nanosystems Initiative München (NIM), Ludwig Maximilians-Universität München, Munich, Germany

<sup>b</sup> Munich Cluster for Systems Neurology (SNergy), Center for Integrated Protein Science (CIPSM), German Center for Neurodegenerative Diseases (DZNE), Institute of Neuronal Cell Biology, Technische Universität München, Munich, Germany

## ARTICLE INFO

## Article history:

Received 31 December 2019

Received in revised form 4 February 2020

Accepted 6 February 2020

Available online 13 February 2020

## Keywords:

Single particle tracking

Orbital tracking

Mitochondria trafficking

Fluorescence

Transport

## ABSTRACT

Recently, a large number of single particle tracking (SPT) approaches have been developed. Generally, SPT techniques can be split into two groups: *ex post facto* approaches where trajectory extraction is carried out after data acquisition and *feedback based* approaches that perform particle tracking in real time [1]. One feedback approach is 3D Orbital Tracking, where the laser excitation beam is rotated in a circle about the object, generating a so called orbit [2,3]. By calculating the particle position from the detected intensity after every orbit in relation to its center, this method allows the microscope to follow a single object in real time. The high spatiotemporal resolution of this method and the potential to optically manipulate the followed object during the measurement promises to yield new deep insights into biological systems [4–7]. By upgrading this approach in a way that the specimen is recentered by a xy-stage on the center of the microscope, particle tracking with this long-range tracking feature is no longer limited to the covered field-of-view. This allows for the observation of mitochondrial trafficking in living zebrafish embryos over long distances. Here, we provide the raw data for antero- and retrograde movement of mitochondria labelled with photo-activatable green fluorescent protein (mitoPAGFP). It relates

\* Corresponding author.

E-mail address: [d.lamb@lmu.de](mailto:d.lamb@lmu.de) (D.C. Lamb).

to the scientific article “Nanoresolution real-time 3D orbital tracking for studying mitochondrial trafficking in vertebrate axons in vivo” [8]. By applying a correlation analysis on the trajectories, it is possible to distinguish between active transport and pausing events with less biasing compared to the mean squared displacement approach.

© 2020 The Authors. Published by Elsevier Inc. This is an open access article under the CC BY license (<http://creativecommons.org/licenses/by/4.0/>).

#### Specifications Table

Subject	Biochemistry, Genetics and Molecular Biology, Biophysics, Neuroscience
Specific subject area	Fluorescence Microscopy, Single Particle Tracking
Type of data	Table Figure
How data were acquired	Hardware: inhouse built confocal microscope based on a Zeiss Axiovert 200 M. For details, see Refs. [8,9] Software: inhouse developed real-time tracking software (LabVIEW)
Data format	Raw Analyzed
Parameters for data collection	Zebrafish larvae (mutant zebrafish line Roy) were embedded in low melting agarose gel. Labelling was carried out by injecting desired UAS construct into eggs immediately after fertilization.
Description of data collection	Data was collected at three days post fertilization at 25 °C in low melting agarose gel. The mitochondrion of interest was photoactivated with 405 nm laser excitation and afterwards tracked using 488 nm excitation. The orbit time was set to 5 ms followed by one 5 ms dark orbit where the specimen was not illuminated. The long-range tracking threshold was set to a threshold of 0.5882 V or 10.18 μm.
Data source location	Department of Chemistry, Ludwig-Maximilians-Universität München, Munich, Germany
Data accessibility	Repository name: Zenodo Data identification number: <a href="https://zenodo.org/record/2815430">10.5281/zenodo.2815430</a> Direct URL to data: <a href="https://zenodo.org/record/2815430#.Xfнк-PwxmUk">https://zenodo.org/record/2815430#.Xfнк-PwxmUk</a> Analysis Program: Repository name: Gitlab Direct URL: <a href="https://gitlab.com/frmie/Orbital-Tracking-Zebrafish2019">https://gitlab.com/frmie/Orbital-Tracking-Zebrafish2019</a>
Related research article	F.Wehekamp, G. Plucińska, R. Thong, T. Misgeld, D. C. Lamb, Nanoresolution real-time 3D orbital tracking for studying mitochondrial trafficking in vertebrate axons in vivo, eLIFE, <a href="https://doi.org/10.7554/eLife.46059.001">https://doi.org/10.7554/eLife.46059.001</a> [8].

#### Value of the Data

- The data provide long traces (up to 111,538 data points and displacements of up to 100 μm) with high spatiotemporal resolution including stationary and directed motion of different velocities.
- The data can be used for developing more detailed models of mitochondrial transport and looking at the transition mechanisms between different motional behaviors.
- Research on neurological diseases may benefit from a detailed analysis of mitochondrial transport as the transport speed and transition probabilities may be affected.

## 1. Data description

Single particle tracking has become a powerful technique for investigating the dynamics of bio-molecules and complexes [1]. Here, we focus on data collected using three-dimensional orbital tracking [2,3], which provides a high temporal and spatial resolution and has already yielded new biological insights (see e.g. [4–7]). In this feedback based approach, the trajectory of the particle is

written to disk during the measurement. Trajectories of individual mitochondria being transported in the axon of sensory neurons in zebra fish embryos are the data we provide in this article (see [8] for details). The trajectories contains a wealth of information regarding the behavior of the particles that can be extracted using various analysis methods. The dataset represents the raw data of several tracked mitochondria in the antero- and retrograde directions. Each .txt file includes all information with respect to one tracked mitochondrion. The file header contains information about the experimental settings, i.e. defined orbit time and -radius, number of delay orbits in which the sample was not illuminated with light and long-range tracking events where the sample is recentered on the microscope (0: disabled; 1: activated) with the corresponding border at which the repositioning is performed. The information available in the .txt files is listed in [Table 1](#).

The first three columns from the data entries provide the particle position information for each coordinate axis. The distances have been updated for any long-range tracking events. In the fourth and fifth columns, the orbit number as well as the orbit time for each orbit during the measurement are saved. For experiments where the particle of interest is moving slowly in comparison to the maximum tracking speed of the setup, dark orbits can be introduced where the excitation laser is turned off during the orbit. This allows the particle to be tracked over longer times with less photobleaching, but at a reduced temporal resolution. Dark orbits are not included in the data file as they do not contribute any new tracking information (but are given an orbit number, which will be missing in the file) and the timing of the dark orbit is included in the determination of the calculated orbit time. In these experiments, data were collected at 5 ms per orbit with every second orbit being a dark orbit, leading to an overall temporal resolution of 10 ms. The detected intensity of each detector per orbit is listed in columns six and seven. When a simultaneous wide field image is measured, the camera frame number is given in column eight. In column nine, information is given of whether a particle is being actively tracked in this orbit. For example, in the beginning of the experiment, when the instrument is looking for a particle, this will be zero. Also, when the intensity of the particle drops below a given threshold indicating photobleaching or that a particle has left the orbit, this will be zero. In the last two columns, information regarding the status of long-range tracking is given. When long-range tracking is enabled, particles that reach a pre-defined distance from the center of the field of view are recentered on the microscope. The orbital

**Table 1**  
Overview of raw data file including file header and data entries.

File Header	
Entry	Description
File Path	Original file path of raw data
Date	Date when experiment was carried out
Time	Begin of experiment
Orbit Time [ms]	User defined time of orbit rotation
Orbit Radius [V]	User defined size of orbit
Tracking Threshold [Hz]	Threshold for distinguishing between the execution of tracking or search algorithm
Delay Orbits	Number of dark orbits
Number of Particles	Number of tracking channels in the experiment
Long Range	Information regarding activation of long range tracking mode (0: disabled; 1: activated)
Long Range Threshold [V]	User defined threshold at which the repositioning of stage is to be executed during a long-range tracking experiment
Data Entries	
Column	Description of entry
1 – 3	Position information (x,y,z)
4	Orbit number
5	Calculated orbit time (including delay orbits and long-range tracking events)
6 & 7	Total detected signal of each detector during the given orbit. Two detectors are used to provide the z-position given in column 3
8	Camera frame for the wide-field detection
9	Tracking (0: inactive; 1: active)
10 & 11	When long-range tracking is enabled, this provides information on whether the sample is being tracked or the microscope stage is being repositioned in x (column 10) and y (column 11) (0: repositioning is inactive; 1: sample is being repositioned)



tracking is performed by adding an offset to the orbiting galvanometer mirrors, which allows fast feedback of the system. Hence, the laser tracks the particle. The quality of tracking decreases as the particle moves farther from the center of the field of view where everything is optimally aligned. Hence, upon reaching a predetermined threshold, the microscope stage is repositioned to place the particle at the center of the field-of-view and the galvanometer mirrors are also recentered. This takes 30–70 ms, which is typically much longer than the time of a single orbit. Hence, these columns indicate whether a reposition event in  $x$  (column 10) or  $y$  (column 11) is taking place during the recorded orbit.

All position values including the particle position (columns 1–3), orbit radius (file header) and long range threshold (file header) are stored as voltages in the corresponding hardware. To transform this information into the trajectory of the particle, the particle position needs to be multiplied by the determined scaling factors (lateral: 17.30  $\mu\text{m}/\text{V}$ ; axial: 10.00  $\mu\text{m}/\text{V}$ ).

## 2. Experimental design, materials, and methods

### 2.1. Sample preparation and data acquisition

A mutated zebrafish line (Roy) was used in these experiments [10–13]. Labelling with mitoPAGFP was carried out by injecting UAS constructs into fertilized eggs [14]. For tracking measurements on the microscope, animals were embedded in low melting agarose gel. The temperature was set to 25 °C during the experiments. The mitoPAGFP of single mitochondria was activated by scanning a region in the vicinity of the particle with 405 nm light and then tracked with 488 nm excitation. As we were tracking moving mitochondria, the mitochondria quickly moved away from the photoactivated area and we did not have problems with multiple photoconverted mitochondria interfering with the tracking algorithm. During tracking experiments with enabled long range tracking, the specimen was automatically recentered in the field of view by a  $xy$ -stage when the mitochondrion was crossing a pre-defined position threshold of 0.5882 V or 10.18  $\mu\text{m}$ . Detailed information regarding sample preparation and data acquisition is provided in the related paper [8].

### 2.2. Correlation analysis

To distinguish between active transport and stationary states, we performed a correlation analysis on the angle between consecutive positions. The idea behind the analysis is that stationary states will have a random distribution of angles where as directed transport will have a preferred direction of motion. If the reader wishes to compare their analysis of the trajectories with what we published (Figure 2 in Ref. [8]), we provide a short description of how we analyzed the data. The axis for the correlation was determined by a line connecting the position between the beginning and end of the trajectory in the  $x, y$  plane. The displacement in  $z$  was small in comparison to the lateral displacement for the trajectories and was ignored. The lateral angle between two orbits  $\Phi(t)$  was calculated along the trajectory. The correlation of the lateral angle was then calculated along the trajectory:

$$\text{Cor}(t, \tau) = \frac{1}{(n - \tau)} \sum_{i=t}^{t+\tau_{\max}-\tau} \Phi(i)\Phi(i + \tau) \quad (1)$$

where  $\tau$  is the correlation lag time,  $t$  the time along the orbit,  $n$  the number of data points and  $\tau_{\max}$  the size of the correlation window. An example of the correlation analysis is shown in Fig. 1 for a retrograde mitochondrial trajectory obtained at 100 Hz (Fig. 1a). The correlation carpets for the zoomed in region of the trajectory were calculated according to equation (1) for three different correlation windows  $\tau_{\max} = 32, 64$  and 128 data points (Fig. 1b). As shown, the noise as well as the sensitivity are strongly dependent on the size of  $\tau_{\max}$ . For our analysis, we choose a time window of  $\tau_{\max} = 64$  data points. For determining the threshold between active transport and stationary states for each trajectory, the angles were randomized and the correlation analysis was repeated for the randomized lateral angles  $\Phi_{\text{rand}}$  obtaining a  $\text{Cor}_{\text{rand}}$ . As the distribution of angles in a trajectory with a large total displacement already contains a bias, we added a negative copy of the trajectory to the data before performing the

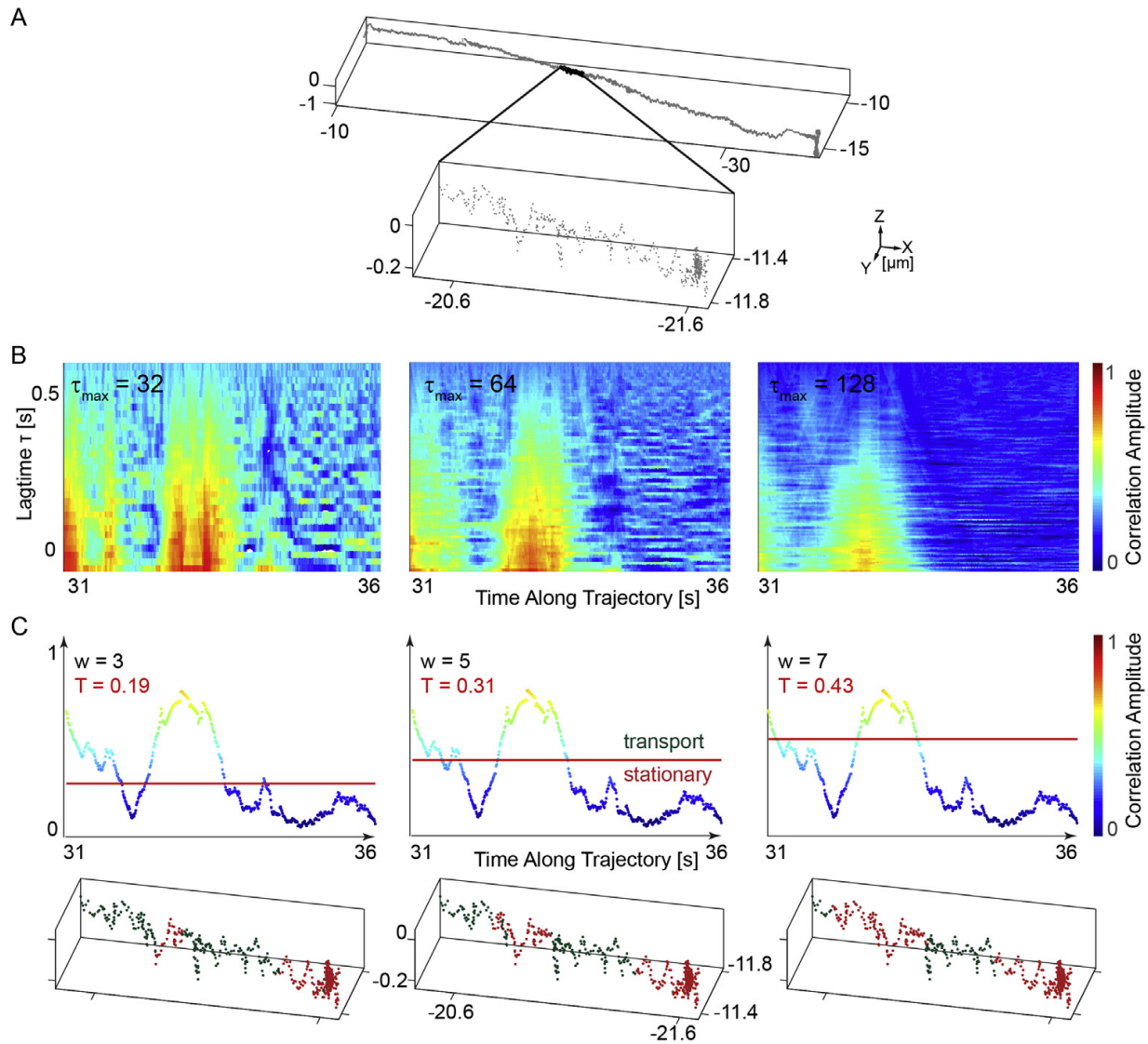


**Fig. 1.** Correlation analysis of a mitochondrial retrograde trajectory. (a) An example trajectory and zoom in of a moving mitochondrion in the retrograde direction with a time resolution of 100 Hz. (b) Correlation carpets of the lateral angles  $\Phi(t)$  between consecutive orbits with different sliding windows  $\tau_{\max}$ . (c) The correlation amplitude determined from the sum of the correlation function over a sliding window of 64 data points is plotted. Three different weighting factors corresponding to thresholds of 3, 5, and 7 times the standard deviation of the correlation function calculated from the randomized trace (Equation (2)) are shown in red. The lower plots show the influence of the different thresholds on the separation of regions of directed transport (shown in green) and stationary phases (shown in red) for the zoomed in region of the trace in panel (a).

randomization. The threshold  $T$  was set by looking for a correlation amplitude that deviated by more than five standard deviations (the weighting factor  $w$  below) from the average of the randomized correlation function, calculated with following equation

$$T = M(Cor_{rand}) + w * \sigma(Cor_{rand}) \quad (2)$$

where  $M$  is the mean of  $Cor_{rand}$  and  $\sigma$  the corresponding standard deviation. Fig. 1c illustrates the influence of three different weighting factors  $w$  to determine the threshold  $T$ . In the lower plot, the zoomed in region of the trajectory in Fig. 1a is separated into stationary phases (shown in red) and transport (shown in green) respectively. As described in the main paper, the weighting factor  $w$  was set to five [8]. Each region of the trajectory above the threshold was treated as a single, directed transport event in which the distance, duration and velocity could be determined. The code for this correlation analysis was written in Matlab and is available online: <https://gitlab.com/frmie/Orbital-Tracking-Zebrafish2019>. It is also worth mentioning the software package of Christoph Gohlke [15], who has

written a Python library to analyze data generated by SimFCS [16]. To analyze our raw data with Christoph Gohlke's software, it is currently necessary to write a read-in function.

## Acknowledgments

We thank Leo Hansbauer and Lisa Haddick for help with the data acquisition, Leanne Godinho for advice on fish genetics, Kristina Wulliman for zebrafish husbandry, Leanne Godinho, Petar Marinković and Monika Brill for cloning some of the used constructs, Douglas Campbell for help with zebrafish injections. We acknowledge the late Chi-Bin Chien (U. Utah) for the *Isl2b:Gal4* line, which was kindly transferred to us by Martin Meyer (King's College London). The authors are grateful for financial support from the Deutsche Forschungsgemeinschaft (DFG) through SFB1032 (Project B3) and SFB870 (Project A11), Priority Program SPP1710, research grants Mi 694/7-1 and 8-1 and the Excellence Clusters Center for Integrated Protein Science Munich (CIPSM), Nanosystems Initiative Munich (NIM) and the Munich Cluster for Systems Neurology (SyNergy). We also thank the Ludwig-Maximilians-Universität, München for support through the Center for NanoScience (CeNS) and the BioImaging Network (BIN). Further support came from the German Center for Neurodegenerative Diseases and the European Research Council under the European Union's Seventh Framework Program (FP/2007–2013; ERC Grant Agreement n. 616791). G.P. was supported by the Graduate School of the Technical University of Munich (TUM-GS) and a postdoctoral fellowship by the DFG.

## Conflict of Interest

The authors declare that they have no known competing financial interests or personal relationships that could have appeared to influence the work reported in this paper.

## Appendix A. Supplementary data

Supplementary data to this article can be found online at <https://doi.org/10.1016/j.dib.2020.105280>.

## References

- [1] A. Dupont, D.C. Lamb, Nanoscale three-dimensional single particle tracking, *Nanoscale* 3 (2011) 4532–4541.
- [2] J. Enderlein, Tracking of fluorescent molecules diffusing within membranes, *Appl. Phys. B* 71 (5) (2000) 773–777.
- [3] V. Levi, Q. Ruan, K. Kis-Petikova, E. Gratton, Scanning FCS, a novel method for three-dimensional particle tracking, *Biochem. Soc. Trans.* 31 (5) (2003) 997–1000.
- [4] I. Verdeny-Vilanova, F. Wehnekamp, N. Mohan, Á. Sandoval Álvarez, J.S. Borbely, J.J. Otterstrom, D.C. Lamb, M. Lakadamyali, 3D motion of vesicles along microtubules helps them to circumvent obstacles in cells, *J. Cell Sci.* 130 (11) (2017) 1904–1916.
- [5] F. Begarani, F. D'Autilia, G. Signore, A. Del Grosso, M. Cecchini, E. Gratton, F. Beltram, F. Cardarelli, Capturing metabolism-dependent solvent dynamics in the lumen of a trafficking lysosome, *ACS Nano* 13 (2) (2019) 1670–1682.
- [6] B.T. Donovan, A. Huynh, D.A. Ball, H.P. Patel, M.G. Poirier, D.R. Larson, M.L. Ferguson, T.L. Lenstra, Live-cell imaging reveals the interplay between transcription factors, nucleosomes, and bursting, *EMBO J.* 38 (12) (2019), e100809.
- [7] S. Coppola, L.C. Estrada, M.A. Digman, D. Pozzi, F. Cardarelli, E. Gratton, G. Caracciolo, Intracellular trafficking of cationic liposome–DNA complexes in living cells, *Soft Matter* 8 (30) (2012) 7919–7927.
- [8] F. Wehnekamp, G. Plucińska, R. Thong, T. Misgeld, D.C. Lamb, Nanoresolution real-time 3D orbital tracking for studying mitochondrial trafficking in vertebrate axons in vivo, *eLife* 8 (2019), e46059.
- [9] F. Wehnekamp, D.C. Lamb, Showcasing student innovation, Available from: <https://forums.ni.com/t5/Showcasing-Student-Innovation/3D-Orbital-Tracking-Microscopy/ta-p/3538000?profile.language=en>, 2016.
- [10] J.Q. Ren, W.R. McCarthy, H. Zhang, A.R. Adolph, L. Li, Behavioral visual responses of wild-type and hypopigmented zebrafish, *Vis. Res.* 42 (3) (2002) 293–299.
- [11] N.B. Fredj, S. Hammond, H. Otsuna, C.-B. Chien, J. Burrone, M.P. Meyer, Synaptic activity and activity-dependent competition regulates axon arbor maturation, growth arrest, and territory in the retinotectal projection, *J. Neurosci.* 30 (32) (2010) 10939–10951.
- [12] M.C. Mullins, M. Hammerschmidt, P. Haffter, C. Nüsslein-Volhard, Large-scale mutagenesis in the zebrafish: in search of genes controlling development in a vertebrate, *Curr. Biol.* 4 (3) (1994) 189–202.
- [13] C.B. Kimmel, W.W. Ballard, S.R. Kimmel, B. Ullmann, T.F. Schilling, Stages of embryonic development of the zebrafish, *Dev. Dynam.* 203 (3) (1995) 253–310.
- [14] L. Godinho, Live imaging of zebrafish development, *Cold Spring Harb. Protoc.* 2011 (7) (2011) p. pdb.top.119.
- [15] C. Gohlke, Python library of laboratory for fluorescence dynamics, Available from: <https://www.lfd.uci.edu/~gohlke/code/lfdfiles.py.html>.
- [16] Globals software - laboratory for fluorescence dynamics, Available from: <https://www.lfd.uci.edu/globals/>.

## **A.2 Multicolor 3D Orbital Tracking**

# Multicolor 3D Orbital Tracking

Frank Mieskes, Evelyn Ploetz, Fabian Wehnekamp, Virgile Rat, and Don C. Lamb\*

**Feedback-based single-particle tracking (SPT) is a powerful technique for investigating particle behavior with very high spatiotemporal resolution. The ability to follow different species and their interactions independently adds a new dimension to the information available from SPT. However, only a few approaches have been expanded to multiple colors and no method is currently available that can follow two differently labeled biomolecules in 4 dimensions independently. In this proof-of-concept paper, the new modalities available when performing 3D orbital tracking with a second detection channel are demonstrated. First, dual-color tracking experiments are described studying independently diffusing particles of different types. For interacting particles where their motion is correlated, a second modality is implemented where a particle is tracked in one channel and the position of the second fluorescence species is monitored in the other channel. As a third modality, 3D orbital tracking is performed in one channel while monitoring its spectral signature in a second channel. This last modality is used to successfully readout accurate Förster Resonance Energy Transfer (FRET) values over time while tracking a mobile particle.**

active feedback loops. In post-processing approaches, the lateral information of the particle is directly encoded in the pixels covering the field of view (FOV). The axial position of the emitter can be obtained by recording images of several planes (z-stacking),<sup>[2]</sup> imaging the diffraction pattern of out-of-focus particles,<sup>[3]</sup> or by engineering the point spread function (PSF).<sup>[4,5]</sup> In the case of 3D active feedback tracking, popular approaches include tetrahedral detection,<sup>[6]</sup> TSUNAMI,<sup>[7]</sup> 3D-SMART,<sup>[8]</sup> and (PIE-)MinFLUX.<sup>[9,10]</sup> Real-time tracking approaches are low throughput but have the advantage of typically higher temporal resolution and the ability to follow a single particle over longer periods of time. As the microscope system is directly focused on the particle of interest, more advanced spectroscopic information can also be collected on the particle during tracking.<sup>[11]</sup> This en-

ables more elaborate analyses of the tracked particle and its measured motion.<sup>[12]</sup>

In this paper, we focus on orbital tracking, which was proposed theoretically for two dimensions by Jörg Enderlein in 2000<sup>[13]</sup> and realized experimentally in three dimensions by Enrico Gratton.<sup>[14]</sup> In orbital tracking, the excitation laser is rotated in a circular pattern or “orbit” around the tracked object. This real-time SPT approach combines high spatial resolution ( $xy$ :  $\approx 3$  nm;  $z$ :  $\approx 20$  nm) with fast response times ( $\approx 5$  ms) over large distances ( $>100$   $\mu\text{m}$ ) and time ranges (up to 10 min). In combination with photoactivation, this method provides unique insights into biological systems, e.g., by tracking cargo transport in vivo or mitochondrial trafficking in zebrafish larvae,<sup>[12,15]</sup> measuring the metabolism in lysosomes by detecting solvent-dependent intensity fluctuations<sup>[16]</sup> or monitoring heterogeneities on surfaces.<sup>[17]</sup> Furthermore, slow conformational changes can be probed in solution, which are not accessible by conventional fluorescence correlation spectroscopy while tracking.<sup>[18]</sup>

Single-particle tracking provides super-resolution information in living dynamic systems. However, often not only subdiffractional resolution is required, but a methodology that additionally allows for investigating the interaction of two particles with high temporal and spatial resolution. This requires the existence of a second channel for SPT and the capability of synchronized tracking. While dual-color SPT is relatively straightforward for camera-based approaches,<sup>[19–21]</sup> feedback-based, dual-color SPT methods have only been developed to track particles in close vicinity ( $<500$  nm) or read out the spectral properties during tracking. Using two-photon excitation, Gratton and


## 1. Introduction

Since the first publication of a single-particle tracking (SPT) instrument for tracking biological samples in 1971 by Berg,<sup>[1]</sup> the field of SPT approaches has tremendously grown. Today, SPT is typically split into two approaches: camera-based measurements where movies are collected and trajectories extracted afterward, and real-time techniques using

F. Mieskes, E. Ploetz, F. Wehnekamp, V. Rat, D. C. Lamb  
Department of Chemistry and Center for NanoScience (CeNS)  
Ludwig-Maximilians-Universität München  
Butenandtstraße 11, 81377 Munich, Germany  
E-mail: d.lamb@lmu.de

F. Mieskes, E. Ploetz, F. Wehnekamp, V. Rat, D. C. Lamb  
Nanosystems Initiative Munich (NIM)  
Ludwig-Maximilians-Universität München  
Schellingstraße 4, 80799 Munich, Germany

F. Mieskes, E. Ploetz, F. Wehnekamp, V. Rat, D. C. Lamb  
Center for Integrated Protein Science Munich (CiPSM)  
Ludwig-Maximilians-Universität München  
Butenandtstraße 5–13, 81377 Munich, Germany

 The ORCID identification number(s) for the author(s) of this article can be found under <https://doi.org/10.1002/smll.202204726>.

© 2023 The Authors. Small published by Wiley-VCH GmbH. This is an open access article under the terms of the Creative Commons Attribution-NonCommercial License, which permits use, distribution and reproduction in any medium, provided the original work is properly cited and is not used for commercial purposes.

DOI: 10.1002/smll.202204726

co-workers demonstrated spectra collection while performing orbital tracking<sup>[11]</sup> and have shown that distances between two closely spaced particles can be measured with nm accuracy.<sup>[22]</sup> Liu et al. tracked conformational changes of tandem partners using two-photon excitation with the TSUNAMI approach.<sup>[23]</sup> Werner and co-workers extended their tetrahedral tracking technique by a second detection volume allowing for the measurement of apparent FRET during tracking.<sup>[24]</sup> In the later dual-color approach, the active tracking is carried out in the donor channel while probing the acceptor signal in parallel. However, none of these approaches have demonstrated the tracking of two particles independently nor of probing accurate FRET.

In this paper, we developed a 3D orbital-tracking system<sup>[12]</sup> for multi-color tracking: It allows for dual-channel tracking of independently as well as correlatively moving particles and provides multi-color detection to enable single-molecule spectroscopy of diffusing particles. First, individual beads emitting at different spectral ranges were tracked independently. A diffusion analysis of the individual 3D trajectories allows for characterization of the motion of particles and monitoring of particle interactions while diffusing in the medium. Here, the position and distance between the particles can be monitored in real time with nanometer resolution. In the next step, we demonstrate its capabilities by dual-color tracking of double-labeled beads in solution mimicking co-diffusive motion. Using two detectors per tracking channel in the presented 3D orbital tracking approach, we employ one detector pair for SPT while using the other detector pair to localize the second fluorescence signal. Alternatively, in a third approach, we use the second detection channel to perform single-molecule spectroscopy. In particular, we performed accurate, single-pair FRET (spFRET) measurements on diffusing particles. This allows us to monitor the position as well as the time trajectories of FRET efficiency of the freely moving particles simultaneously.

## 2. Experimental Section

### 2.1. Materials and Preparation Procedures

Chemicals were purchased from Sigma–Aldrich and used without further purification, if not stated otherwise, including bovine serum albumin (BSA), catalase (*Asp. niger*), ethylenediamine-tetraacetic acid (EDTA), glucose, glucose oxidase (*Asp. niger* Type VII), glycerol, phosphate-buffered saline (PBS), Tris base, Tris HCl, Trolox, and sodium chloride.

For image calibration experiments, multifluorescent beads purchased from Spherotec Inc (FP-0557-2) were used. For dual-color tracking experiments of independently moving beads, we used two suspensions of coated, fluorescently labeled polystyrene particles 0.1% (w/v) purchased from Kisker Biotech: 1) Streptavidin-coated particles (named “yellow”/PC-SAFY-0.5; Kisker) emitting between 460–540 nm and having an average diameter of 450 nm and 2) Avidin-coated particles (named “purple”/PC-AFU-0.5; Kisker) emitting between 580–650 nm with a diameter of 560 nm. For dual-color tracking measurements on co-diffusing labeled objects, the avidin-coated, “purple” particles (PC-AFU-0.5; Kisker) were employed, and

```

5'-GACCTATGCTAATTATTAACCCCTTAXATTCTCTGCACGAC-3'-B10
DNA 3: 3'-CTGGATACGATTAATAAYTGGGGAATATAAGGAGCTGCTG-5'
DNA 2: 3'-CTGGATACGATYAATAATTGGGGAATATAAGGAGCTGCTG-5'
DNA 1: 3'-CTGGAYACGATTAATAATTGGGGAATATAAGGAGCTGCTG-5'
X = T - Atto647N           Y = T - Atto565
    
```

**Scheme 1.** DNA sequences used in Tracking/spFRET experiments. The top strand (T) contained the donor fluorophore (Atto565), while one of three different bottom strands (B) containing the acceptor fluorophore (Atto647N) was annealed to the top strand.

they were labeled with a biotinylated Atto488-dye (AD 488; Atto-Tec GmbH). Dual-color surface localization experiments of the same bead samples were used for verification of the precision of the image calibration procedure (Figure 3B).

Tracking experiments with spFRET readout of dsDNA oligos were carried out on labeled streptavidin-coated silica beads (480 nm, CS01000-2; Polysciences Europe GmbH) with biotinylated dsDNA oligos and Atto488. Labeling as well as mixing of particles was carried out in PBS.

Single-stranded DNA 40-mers containing the desired modifications were obtained commercially (**Scheme 1**). Bottom strands were labeled at the B6, B12, and B18 positions with the donor fluorophore Atto565 and purchased from Metabion. The top strand was purchased from IBA, biotinylated at the 3'-end and contained the acceptor dye Atto647N at position T27. The complementary DNA strands were annealed in 500 mM NaCl, 20 mM TRIS, and 1 mM EDTA at pH 8. After heating the mixture to 95 °C, the temperature was held for 3 min and cooled down to 4 °C at a rate of 1 °C min<sup>-1</sup>.

If not mentioned otherwise, all samples were measured in 8-well chamber slides (Nunc LabTek I, Thermofisher) that had been passivated with 1 mg mL<sup>-1</sup> BSA in PBS for 10 min before the measurement. MFD-PIE experiments<sup>[25]</sup> were carried out on freely diffusing dsDNA molecules at 25–50 μM in PBS at room temperature (20 °C).

### 2.2. Cell Culture

An HuH7 cell line stably expressing Rab5-GFP had been validated and tested negative for mycoplasma contamination. HuH7 Rab5-GFP were cultured in high-glucose DMEM (Gibco) with 10% foetal bovine serum, 100 U mL<sup>-1</sup> Penicillin, 100 μg mL<sup>-1</sup> streptomycin, and 400 μg mL<sup>-1</sup> geneticin (G418, Gibco) with 5% CO<sub>2</sub> at 37 °C. Cells were plated at 80,000 cells per well in a LabTek II chambered coverglass (Nunc, Thermofisher). Twenty-Four hours after seeding, the medium was exchanged with a DMEM red phenol free medium, and the previously described “purple” beads were added half an hour prior to the observation.

### 2.3. Orbital Tracking Setup

#### 2.3.1. Instrument

The general microscope design was based on a previously developed confocal setup for one-color 3D Orbital-Tracking,<sup>[12]</sup> which was extended for multi-channel, dual-color tracking.

Three lasers were used as excitation sources (Sapphire 488-20 CDRH; Coherent/Jive CDRH CW 561; Cobolt/05-LHP-151; Melles Griot) at 488, 561, and 633 nm, respectively. The lasers were guided through an acousto-optical tunable filter (TF525-250-6-3-GH19A, Gooch & Housego) to control the excitation cycles of the three light sources. Afterwards, they were coupled into a single-mode fiber (QPMJ-A3A,3A-405/650-3/125-3-5-1; Oz Optics) to clean up the beam profile and decouple the excitation path from the microscope. The excitation and detection path of the microscope were combined by a quad-band polychroic mirror (zt405/488/561/640rpc; AHF), which transmits the fluorescence emission and reflects the laser beams onto a two-axis galvanometric mirror system (GVSM002/M; Thorlabs). A telescope system (80 and 250 mm achromatic lenses, Thorlabs) was used to image the output of the galvanometric mirrors onto the back aperture of the objective and the laser beam was focused by the objective onto the sample (PlanApo VC 60x/1.20WI; Nikon). The fluorescent signal was collected by the same objective. After passing the quad-band polychroic mirror, a long pass dichroic mirror (H560 LPXR, AHF) reflects the emission triggered by the 488 nm excitation laser. The fluorescence emission was filtered by an emission bandpass filter (525/50 Brightline HC; AHF) and then directed onto the two detection paths by a 50:50 beam splitter (#F21-020; AHF). Afterwards, it was focused by a lens (AC254-050-AB; Thorlabs) onto two 50  $\mu\text{m}$  multimode fibers (M42L01, Thorlabs), which act as confocal pinholes, which guide the light to the separate avalanche photodiode detectors (APD, CountBlue; Laser Components).

The second detection channel was constructed identically. It shared the same geometry as channel one but employed two different focusing lenses (AC254-075-AB; Thorlabs) and APDs (SPCM-CD 3017; Perkin Elmer). For the dual-color tracking modality, the fluorescent signal was split onto two detectors by a 50:50 beam splitter (#F21-020; AHF) and spectrally filtered by an emission filter (685/70; Thorlabs). For parallel spectroscopic readout (in this case FRET), the 50:50 beam splitter was exchanged by a dichroic mirror (zt640rdc; Chroma) separating

the donor from the acceptor signal. Each beam was cleaned up by an additional emission filter (593/40 and 685/70; Thorlabs, respectively).

### 2.3.2. Tracking Software

The experimental setup was controlled using a Field Programmable Gate Array (FPGA) controlled via LabVIEW2018. The software was executed on two different levels, consisting of a non-deterministic and a deterministic execution (Figure 1), to achieve exact hardware triggering during the orbital tracking experiment, as described previously.<sup>[12]</sup> In brief, the self-written program was executed on two systems: the host computer and a deterministic processing unit (cRIO 9082; National Instruments), combining a real-time processor and a FPGA. The real-time unit synchronizes all hardware components, executes the tracking algorithm, and streams the data to the host computer. It synchronizes, in particular, the execution of the hardware via TTL pulses, receives the incoming TTL signals from the detectors, and generates the voltages for repositioning the galvanometric mirrors to generate the rotating orbit of the exciting lasers. Each orbit was divided into 16 segments. The FPGA bins the photon detected for each orbit segment, stores it in a direct memory access first-in-first-out (DMA-FIFO) buffer, and streams it to the real-time processor for calculating the particle position within the orbit (see Section 2.3.3, Tracking algorithm). This was done for both detectors within the detector channel, i.e., the real-time processor receives 32 bins in total. After determining the lateral position of the particle from the summed data of both detectors, the value was transferred back to the FPGA for the next rotation period provided the binned signal exceeds a user-defined threshold (typically 5 kHz). When the signal falls below the given threshold, the particle was considered to be outside of the orbit and a search algorithm is started. In parallel, the data were streamed to the host computer (non-deterministic unit) via a gigabit Ethernet connection and written to a solid-state disc as a text (.txt) file. The text file

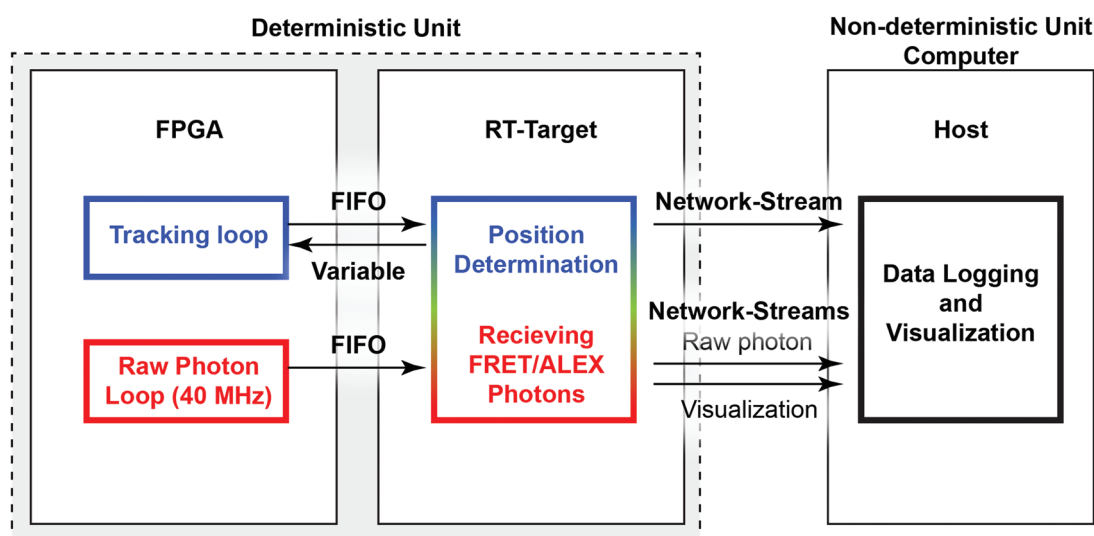


**Figure 1.** Flow chart of data acquisition for the Tracking/spFRET modality.

contains the 3D position information and intensities for each channel.<sup>[26]</sup> In addition to receiving the data, the host computer generally controls the real-time unit, i.e., it defines experimental settings, starts and stops the tracking algorithm, and visualizes the received tracking data during the experiment.

The above-described procedure summarizes the overall software architecture for one tracking channel. For dual-color experiments, both tracking channels were read-out independently. One .txt file was generated per each tracking channel, in which the data per detector-pair were written. Here, the real-time unit alternates the data acquisition and streaming to the real-time processor for each tracking channel resulting in a decrease of time resolution by a factor of 2–10 ms for the experiments here. The software discriminates between the three tracking modalities described in this publication as follows:

- 1) For independent dual-color, real-time tracking experiments, the unit treats each tracking channel independently. The real-time processor calculates the position of each particle and transfers the information to the FPGA, i.e., the instrument switches between both particle positions alternately. When the fluorescence intensity of a particle in one channel falls below the tracking threshold, the search algorithm is executed in the corresponding channel while the second particle is still tracked.
- 2) When probing correlative motion, one tracking channel is defined as the “leading channel”. After orbiting around the particle in the leading channel, the data are streamed to the real-time processor for position calculation and the feedback algorithm applied. The next orbit is performed at the updated position with the excitation laser of the second channel. The data from the second orbit are transferred to the real-time unit, which directly streams it to the host without a position update. Now, the next orbit is executed for the “leading channel”. In this mode, the search algorithm is only started when the detected count-rate is below the threshold of the leading channel.
- 3) In the tracking/FRET modality, one tracking channel is set as the leading channel for position determination while the other channel monitors the fluorescence signal of the tracked FRET pair. The data acquisition, streaming, and position update are the same as described above in the case of correlative motion. After performing an orbit for the tracking channel, a spatially identical orbit is performed for either direct donor or acceptor excitation according to the ALEX sequence. One complete cycle comprises: tracking channel, acceptor excitation, tracking channel, donor excitation.

The TTL signal of each detector was acquired with the 40 MHz time resolution given by the onboard clock of the FPGA. In addition to the micro-time, which was given as the number of clock cycles since the last photon was detected, each detected photon was tagged with further information regarding the orbit number, orbit segment, detector number, and excitation laser. All information was multiplexed into a 64-bit unsigned integer and transferred in separate data FIFO1 to the real-time processor (Figure 1). To have a live update of the FRET signal on the host computer, the detected photons during donor and acceptor excitation are also binned in user-defined time intervals and the values were transferred using a FIFO2 and network stream (visualization stream, Figure 1). This data

transfer was executed independently from the tracking algorithm on the FPGA. On the host, the received data from the FRET stream was written into a binary sidecar file consisting of the same name as the .txt file. The binned count-rate received from the visualization stream was monitored to inform the user about the presence of the FRET pair.

### 2.3.3. Tracking Algorithm

The implemented 3D tracking algorithm separates the position determination for the lateral and axial localization. The total intensity from both detectors was used to calculate the lateral position. This signal was measured along the orbit and binned into 16 different positions and expressed as a Fourier series with coefficients up to the 16th order ( $k = 16$ ):

$$I(\varphi, r) = \frac{a_0(r)}{2} + \sum_{k=1}^{16} (a_k(r) \cos(k\varphi) + b_k(r) \sin(k\varphi)) \quad (1)$$

The lateral position of the particle with respect to the center of the orbit is encoded in the zero- and first-order coefficients obtained from a Fast Fourier Transformation. The angular position,  $\varphi$ , and the radial distance,  $d'_r$ , from the orbit center can be calculated from the zero- and first-order coefficients as follows:

$$\varphi = \tan^{-1} \left( \frac{b_1}{a_1} \right) \quad (2)$$

$$d'_r = r_{\text{orbit}} \cdot f(r) \cdot \frac{\sqrt{a_1^2(r) + b_1^2(r)}}{a_0(r)}$$

where  $r_{\text{orbit}}$  is the radius of the orbit and  $f(r)$  is a theoretically determined scaling function that converts the modulation of the signal to a distance. The axial localization is accessible by comparing the difference in signal between one detector pair. The particle position  $d'_z$  with respect to the focal plane can be calculated as follows

$$d'_z = \Delta z \cdot g(z) \cdot \frac{I_{APD1} - I_{APD2}}{I_{APD1} + I_{APD2}} \quad (3)$$

where  $\Delta z$  is the distance between the detection planes of APD1 and APD2, which are positioned equidistantly above and below the actual focal plane, and  $g(z)$  is the corresponding scaling function for  $z$ . Both scaling functions are implemented as lookup tables to decrease the computation time. Slight differences in the effective detection efficiency for the two detectors in a detection pair will lead to an offset in the position of the particle from the actual focal plane. However, this  $z$ -offset does not impact the determined trajectory and the  $z$ -feedback loop aims to equalize the counts between the two APDs. For two color tracking, the offset from the focal plane along with chromatic aberrations leads to an offset between the two tracking channels. As the objective is moved in the  $z$ -dimension using a piezo stage for the axial tracking routine, this offset is independent of the absolute  $z$ -position and is found to vary only slightly in the  $x$ - $y$  plane (Figure S1, Supporting Information).



### 2.3.4. Data Collection and Analysis

As described above, dual-color tracking experiments can be carried out in two different ways: 1) both tracking channels are treated independently, or 2) the software actively tracks the movement of one particle and probes its surrounding for the second particle. In both variations, the corresponding laser lines can either be simultaneously activated or alternated.

**Image Calibration and Dual Color Localization Experiments:** When measuring the position of multifluorescent beads that were detectable in both detection channels, it was evident that this microscope had a significant shift between the two channels. The main contribution of this offset originates from the chromatic aberrations of the telescope optics between the galvanometer mirrors and the objective, which were crucial for good scanning and imaging. Hence, it was necessary to register the two detection channels to correct for the aberrations. The chromatic aberrations could also be minimized by purchasing optimized lenses, as it was shown recently for another microscope system.<sup>[27]</sup>

To register the positions of the two detection channels, a transition matrix was determined using multifluorescent beads. One hundred microliters of the stock solution (0.2%) of multifluorescent beads was diluted 100-fold in PBS, added to an untreated LabTek chamber and allowed to sediment for 10 min. The beads were then tracked for 5,000–10,000 orbits. The red detection channel was defined as the leading channel for actively tracking one particle and the blue detection channel as the passive localization channel for determining the position from the second signal. Using the position reconstruction from the fluorescent signal of the blue channel, the coordinates were mapped onto the leading channel generating a transformation matrix. The geometric transformation function *fitgeotrans* from MATLAB was used to calculate the transformation matrix. The experiment was repeated with Atto488 labeled, red-emitting avidin coated beads. One hundred microliters of a 100-fold diluted 0.1% suspension was mixed with 100  $\mu\text{L}$  of a 100  $\mu\text{M}$  Atto488-biotin solution and incubated for 10 min. The mixture was then added to an untreated LabTek chamber. The beads were tracked with the same settings for 5,000 orbits each after 10 min of sedimentation time. Whenever the spectral range of one of the tracking channels is changed, the transformation matrix needs to be redetermined.

**Dual-Color 3D Orbital Tracking Experiments:** Dual-color tracking experiments were demonstrated by using 488 and 633 nm excitation to update the position of a particle in the leading channel first and consecutively localize the second particle (independent motion) or its emission (correlative motion). All experiments were carried out at laser powers of 0.32  $\mu\text{W}$  for 488 nm and 0.42  $\mu\text{W}$  for 633 nm laser excitation measured before the microscopy body. The orbit-time for each channel was set to 5 ms.

For independent dual-color tracking, two 0.1% particles suspensions of  $\approx 500$  nm size beads were mixed (see Section 2.1, Materials and Chemical section for further details). Two microliters of the “yellow” beads and 10  $\mu\text{L}$  of “purple” beads were mixed with 188  $\mu\text{L}$  PBS and directly added to the passivated LabTek chamber for the measurements.

For correlative dual-color tracking, a 100-fold diluted suspension of 0.1% “purple” particles was labeled with biotinylated

Atto488. Here, 100  $\mu\text{L}$  of the pre-diluted particle solution was added to 100  $\mu\text{L}$  of a 100  $\mu\text{M}$  Atto488-biotin solution and incubated for 10 min. As the vast majority of the fluorophore is bound to the avidin-coated beads, no purification step was necessary afterwards. The sample was then directly diluted with buffer to a final volume of 750  $\mu\text{L}$  containing 1% (w/v) Glucose, 10% (v/v) Glycerol, 1 mM Trolox, and 10% (v/v) Glucose-Oxidase/Catalase system for photo-stabilizing the Atto488. This imaging mix was immediately added to a passivated chamber of an 8-well LabTek slide and sealed. Experiments were started after waiting for an additional 5 min for oxygen removal.

**Tracking/spFRET Experiments:** For 3D FRET-tracking, the microscope alternates between reading out the position in the tracking channel 1 (488 nm excitation) and probing the FRET signature of the sample in the second channel. ALEX excitation was used at 633 and 561 nm with position determination, probed at 488 nm. For slowly diffusing objects, the donor and acceptor excitation times can be performed for an integer number of orbits before switching to 488 nm excitation for updating the position of the particle. 3D FRET/tracking measurements were carried out using 12  $\mu\text{W}$  for 488 nm, 88  $\mu\text{W}$  for 561 nm, and 18  $\mu\text{W}$  for 633 nm excitation measured before the microscope body.

To extract the distance of fluorescent labels on diffusing dsDNA via FRET, the dsDNA oligos were attached to slowly diffusing streptavidin-coated silica beads (#CS01000-2; Polysciences Europe GmbH). For this, 1  $\mu\text{L}$  of the 146  $\mu\text{M}$  bead suspension was added to 50  $\mu\text{L}$  of 5  $\mu\text{M}$  dsDNA and pre-incubated the mixture for 5 min. During mixing, a few beads were bound with a high concentration of dsDNA but the majority of beads ended up with either one or no dsDNAs attached. Afterwards, 50  $\mu\text{L}$  of 60  $\mu\text{M}$  Atto488-biotin was added to the mixture and allowed to incubate for 5 min. For photostabilization, the prepared solution of 101  $\mu\text{L}$  was filled to a total volume of 750  $\mu\text{L}$  of PBS containing 1% (w/v) glucose, 10% (v/v) glycerol, 1 mM Trolox, and 10% (v/v) mixture of the glucose-oxidase/catalase system (6.25  $\mu\text{M}$  glucose-oxidase in 40% glycerol and 2 mM TCEP; 400–800 nM catalase). This imaging mix was immediately added to a passivated chamber of an 8-well LabTek slide and sealed. First measurements were started after allowing 5 min for oxygen removal.

**Data Analysis:** The obtained data from dual-color tracking experiments were loaded and analyzed with home-written scripts in MATLAB2018a. The FRET data collected during tracking were analyzed with a home-written program developed in LabVIEW2018. After loading the tracking and sidecar files, the full data were extracted and converted into time bins of 50 ms. Next to the information from the first tracking channel including intensity and its 3D trajectory, the software extracts the donor as well as acceptor intensities and calculates the FRET efficiency for the second detection channel. Next, the extracted traces were manually inspected for active tracking in the tracking channel. Otherwise, the respective data files were excluded from further analysis.

#### 1) Diffusion analysis

Theoretical diffusion coefficients of beads were calculated using the Stokes–Einstein Equation

$$D = \frac{k_B T}{6\pi\eta r} \quad (4)$$

where  $k_B$  is the Boltzmann constant,  $T$  the temperature,  $\eta$  the viscosity of the buffer, and  $r$  the hydrodynamic radius of the particle.

Diffusion coefficients for the measured traces were determined using the mean squared displacement (MSD) approach

$$MSD(t) = \left\langle \left( \bar{r}(t+t') - \bar{r}(t') \right)^2 \right\rangle \quad (5)$$

where  $\bar{r}(t)$  is the 3D trajectory of the particle. For reliable results, the MSD was calculated over a quarter or an eighth of the trajectory data, depending on the length of the trace. MSD plots of traces showing Brownian motion (correlative tracks) were fitted to

$$MSD(t) = 6Dt \quad (6)$$

with  $t$  representing the lag time between data points and  $D$  the diffusion coefficient. MSD plots of traces exhibiting diffusion with a flow were fit using:

$$MSD(t) = 6Dt + (Vt)^2 \quad (7)$$

where  $V$  is the flow velocity of the medium.

For motion in cells, one typically observes multiple types of diffusional behavior. To summarize directed transport, Brownian diffusion and anomalous diffusion, the MSD plots were fitted to a generic equation:

$$MSD(t) = b t^{\alpha_D} \quad (8)$$

where the exponent,  $\alpha_D$ , indicates the type of motion and  $b$  is related to the respective diffusion or velocity.<sup>[28]</sup> For  $\alpha_D$ , the MSD was interpreted as directed transport with  $b = V^2$ . For  $\alpha_D \sim 1$  and  $\alpha_D < 1$ , the motion in these regions of the trajectory was interpreted as normal diffusion or anomalous diffusion, respectively, with  $b = 6D$ .

## 2) SpFRET analysis

All trajectories were inspected and characterized as FRET traces when they exhibited either single-step photobleaching of the FRET pair or count rates compatible with single fluorophores. Regions within the selected traces were then categorized as: 1) FRET signal, 2a) donor only or 2b) acceptor only, and 3) as background. Bead specific background correction was performed when possible.

$$bg_{XY} = \frac{1}{(n_{\text{stop}} - n_{\text{start}} + 1)} \sum_{\text{start}}^{\text{stop}} B_{XY}(t) \quad (9)$$

where  $B_{XY}$  is signal intensity of the background measured with  $X$  laser excitation and  $Y$  detected emission channel for the particular bead, and  $n$  represents starting and stopping data points for the selected region. Otherwise, tracked beads not exhibiting a DNA label were used to categorize the background due to scattering or impurities in the buffer. The average background values from non-labeled beads were calculated for each channel ( $\bar{B}_{XY}$ ). The calculated background was then subtracted from the measured fluorescence signal

$$F_{C,XY}(t) = F_{XY}(t) - bg_{XY} \quad (10a)$$

or

$$F_{C,XY}(t) = F_{XY}(t) - \bar{B}_{XY} \quad (10b)$$

After categorizing the corresponding intensity traces and applying background correction for each tracked particle, the correction factors for direct excitation  $\alpha$ , spectral cross talk  $\beta$ , and detection sensitivity  $\gamma$  were determined.<sup>[25,29]</sup> The molecule-wise correction factor  $\alpha$  for direct excitation was derived from “acceptor only” traces according to

$$\alpha = \frac{1}{(n_{\text{stop}} - n_{\text{start}} + 1)} \sum_{t_{\text{start}}}^{t_{\text{stop}}} \frac{F_{DA}(t)}{F_{AA}(t)} \quad (11)$$

Similarly, the correction factor  $\beta$  for spectral cross talk was derived from “donor only” traces, by taking the ratio of:

$$\beta = \frac{1}{(n_{\text{stop}} - n_{\text{start}} + 1)} \sum_{t_{\text{start}}}^{t_{\text{stop}}} \frac{F_{DD}(t)}{F_{DA}(t)} \quad (12)$$

In traces exhibiting acceptor photobleaching, the correction factor  $\gamma$  was derived by

$$\gamma = \frac{\left( \frac{1}{(n_{1,\text{stop}} - n_{1,\text{start}} + 1)} \sum_{t_{1,\text{start}}}^{t_{1,\text{stop}}} F_{DA}(t) \right) - \left( \frac{1}{(n_{2,\text{stop}} - n_{2,\text{start}} + 1)} \sum_{t_{2,\text{start}}}^{t_{2,\text{stop}}} F_{DA}(t) \right)}{\left( \frac{1}{(n_{2,\text{stop}} - n_{2,\text{start}} + 1)} \sum_{t_{2,\text{start}}}^{t_{2,\text{stop}}} F_{DD}(t) \right) - \left( \frac{1}{(n_{1,\text{stop}} - n_{1,\text{start}} + 1)} \sum_{t_{1,\text{start}}}^{t_{1,\text{stop}}} F_{DD}(t) \right)} \quad (13)$$

where regions 1 and 2 are regions of the trace selected before and after acceptor photobleaching, respectively. For cases where bead-specific correction factors could not be calculated, the average value was used instead (i.e.,  $\bar{\alpha}$  for direct excitation,  $\bar{\beta}$  for spectral cross talk, and  $\bar{\gamma}$  for detection efficiency). Using the determined correction factors, a corrected FRET efficiency value  $E$  was calculated:

$$E(t) = \frac{F_{DA}(t) - \bar{\alpha}F_{AA}(t) - \bar{\beta}F_{DD}(t)}{F_{DA}(t) - \bar{\alpha}F_{AA}(t) - \bar{\beta}F_{DD}(t) + \bar{\gamma}F_{DD}(t)} \quad (14)$$

A particle-wise averaged FRET efficiency was then calculated. The FRET efficiency and uncertainty of the different FRET constructs were given by the peak and standard deviation of a Gaussian fit to the spFRET histogram.

## 2.4. SpFRET PIE-MFD Experiments

Solution-based, spFRET experiments on dsDNA were performed on an inverted, confocal microscope (Eclipse Ti, Nikon, Germany) equipped with 565 nm (LDH-D-TA-560, PicoQuant, Germany), and 640 nm excitation (DH-D-C-640, PicoQuant, Germany). The average excitation intensities for dual color measurements were 80  $\mu\text{W}$  at 565 nm and 30  $\mu\text{W}$  at 640 nm. The resulting fluorescence was separated from the excitation beams via a polychroic mirror (zt405/488/561/633, AHF; Germany), passed through a confocal pinhole (75  $\mu\text{m}$ ) and separated via polarization using a polarizing beamsplitter (PBS251, Thorlabs, Germany). The fluorescence was then split

spectrally via additional dichroic mirrors (BS560 and 640DCXR, AHF; Germany) and cleaned up with the appropriate emission filters (ET525/50 for the blue channel; ET607/36, AHF, Germany for yellow detection; ET670/30, AHF, Germany for red detection). Photons were detected using photon-counting APDs (Count-100B, Laser Components, Germany; 2x SPCM AQR-14/2x SPCM AQR-16, PerkinElmer, USA) and registered by independent but synchronized time-correlated single-photon counting (TCSPC) hardware (HydraHarp400, PicoQuant, Germany). The detector signal was recorded using a home-written program in C#.

The recorded data were evaluated using PAM<sup>[30]</sup> to characterize the double-labeled dsDNA constructs. The FRET efficiency, labeling stoichiometry, fluorescence lifetime and anisotropy were determined. To calculate these various parameters, the detected fluorescence photons were sorted according to the detection channels (donor detection channel: D; acceptor detection channel: A) and excitation source, which is encoded in the photon arrival time. Burst selection was performed by considering detected photons to belong to a single burst as long as the local count rate within a sliding window exceeded a certain threshold (5 photons within 500  $\mu$ s or 10 kHz for the experiments performed here). Only bursts with a minimum of 50 photons were further analyzed. After burst selection, the bursts were additionally filtered using a minimum of at least 150 photons and an ALEX-2CDE filter<sup>[31]</sup> between 0 and 30. After background subtraction, the uncorrected proximity ratio  $E^*$  and labeling stoichiometry  $S^{\text{raw}}$  were calculated for each fluorescent burst characterized by three photon-streams, i.e., by its donor-based donor emission  $F_{DD}$ , donor-based acceptor emission  $F_{DA}$  and acceptor-based acceptor emission  $F_{AA}$ .

$$E^* = \frac{F_{DA}}{F_{DD} + FF_{DA}} \quad (15)$$

$$S^{\text{raw}} = \frac{F_{DD} + F_{DA}}{F_{DD} + F_{DA} + F_{AA}} \quad (16)$$

While  $E^*$  monitors the proximity between both fluorophores,  $S^{\text{raw}}$  describes the ratio of donor-to-acceptor intensities. After binning the detected bursts into a 2-D  $E^*$ - $S^{\text{raw}}$  histogram,<sup>[25,29]</sup> the contribution of direct excitation  $\alpha' = S_{AO}^{\text{raw}} / (1 - S_{AO}^{\text{raw}})$  is derived by the acceptor-only population (AO). Using the uncorrected proximity ratio  $E_{DO}^*$  of the donor-only population (DO) allows for determining the amount of spectral cross talk  $\beta' = E_{DO}^* / (1 - E_{DO}^*)$  into the acceptor channel. After correction of spectral cross talk, direct excitation, as well as differences in detection sensitivities between the channels,<sup>[25]</sup> the corrected FRET efficiency  $E$  and stoichiometry  $S$  are given by

$$E = \frac{F_{DA} - \alpha' F_{AA} - \beta' F_{DD}}{F_{DA} - \alpha' F_{AA} - \beta' F_{DD} + \gamma F_{DD}} \quad (17)$$

$$S = \frac{F_{DA} - \alpha' F_{AA} - \beta' F_{DD} + \gamma F_{DD}}{F_{DA} - \alpha' F_{AA} - \beta' F_{DD} + \gamma F_{DD} + F_{AA}} \quad (18)$$

The fully corrected FRET efficiency is related to the distance between donor and acceptor  $r$  using:

$$E = \frac{1}{1 + \left(\frac{r}{R_0}\right)^6} \quad (19)$$

where  $R_0$  refers to the Förster radius, i.e., the distance between donor and acceptor fluorophores at which the FRET efficiency is 50%. The Förster radius for fluorophore pairs in this study (Atto565-Atto647N) was taken to be 69 Å.

### 3. Results

The multicolor 3D orbital-tracking setup developed in this work was implemented based on a previously described confocal microscope.<sup>[12]</sup> A schematic representation of the orbital tracking approach is given in Figure 2A. By circularly rotating the laser excitation volume of the confocal microscope around the diffusing particle, the fluorescence signal will be modulated differently depending on its position within the orbit. By performing a fast Fourier transformation (FFT) on this signal, the phase and amplitude modulation of the emitted fluorescence can be determined, which encode the particle position with respect to the orbit center and allow for lateral tracking. To obtain axial information at the same time, we implemented a detector pair. The detected signal is split equally between both APDs via a beam-splitter (Figure 2B) and the detection volumes of both APDs are equidistantly positioned out-of-focus. They are positioned above and below the focal planes via two separate lens systems and multimode fibers are used as confocal pinholes for defining the detection volume. The signal from both detectors is added together for lateral tracking while the intensity ratio is used for axial tracking (see Experimental Section). With the 3D information at hand, a feedback loop is used to re-center the orbit of the microscope on the diffusing particle and enables single-color, real-time 3D orbital tracking.

To enable dual-color 3D orbital tracking and/or reading-out of the spectroscopic signatures of a tracked particle, the instrument is equipped with two pairs of detectors and three laser lines at 488, 561, and 633 nm (Figure 2B). For generating the orbit of the laser beam, galvanometric mirrors are used. The system is also equipped with a wide-field modality to visualize the environment around the particle being tracked. Diffusing particles in the sample were tracked using orbit repetition rates of up to 200 Hz. After excitation, the resulting emission of the sample was detected on the two pairs of APDs. Using this configuration, experiments with three different modalities can be performed: 1) the dual-channel tracking configuration in which both channels alternately measure the position of two independent particles (Figure 2C), 2) correlative motion where we actively track the particle in three dimensions in one channel while alternatively determining the position of the second fluorescent species in the second channel (Figure 2D), or 3) the tracking of channel 2 was modified for reading out the spFRET signature of the tracked molecule (Figure 2E).

#### 3.1. Independent Dual-Color Tracking

Dual-color tracking experiments were carried out in two different configurations. We first targeted the independent motion

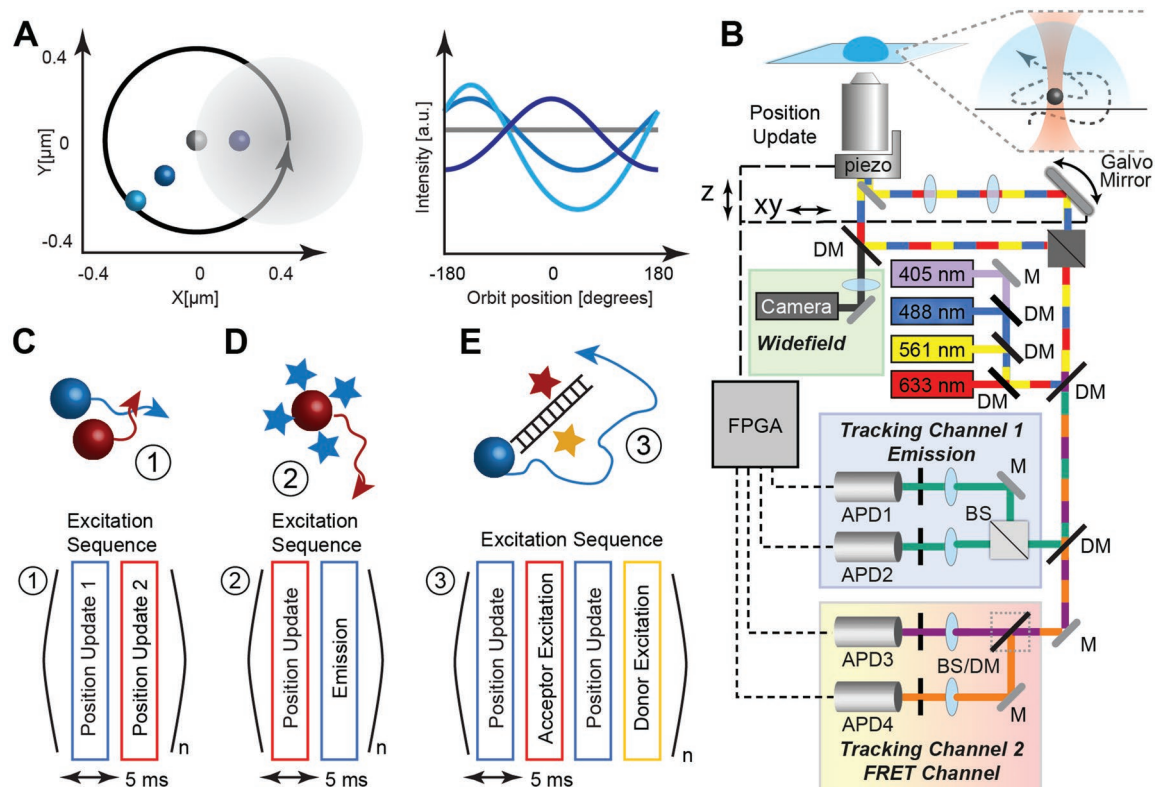


**Figure 2.** Dual-color, real-time 3D Orbital-Tracking: setup, theory, and excitation sequences for the implemented modalities. A) The principle of orbital tracking: left, the laser (grey shaded area) is rotated in an orbit (black circle) generating a fluorescence signal depending on the position of the emitters (depicted as grey and blue spheres) with respect to the orbit. Right, a schematic of the modulated signal is shown for the corresponding positions shown in the left panel. B) Schematic of the instrument. Three excitation lasers are guided onto a galvanometer-driven, two-axis mirror system for generating the orbit. A 60x water objective focuses the beam into the specimen. The fluorescence signal is collected by the same objective and relayed to the detection pathway by a PM. The signal is spectrally separated between the two detection channels via a DM. In each detection channel, the light is either split into two focal planes or into additional spectral regions, and focused on multimode fibers, which act effectively as confocal pinholes and guide the light to the APDs for detection. The detectors are connected to a FPGA which repositions the laser beam via an active feedback loop. Abbreviations: APD, avalanche photodiode; BS, beam splitter; FPGA, field-programmable gate array; PM, polychroic mirror; DM, dichroic mirror; M, mirror; PH, multimode fiber acting as a pinhole. C–E) Multi-color 3D orbital tracking modalities. Spectrally different particles can be tracked C) independently, D) correlatively or E) with spectroscopic readout. The corresponding excitation sequences for the implemented modalities are depicted below. Each rectangle represents one full orbit of the corresponding laser wavelengths. For the worked presented here, an orbit-time of 5 ms was used.

of two different emitters by alternately tracking their position in two separated detection channels. This is similar to the multiplexing approach that allows multiple particles to be tracked simultaneously using orbital tracking<sup>[32]</sup> but with different spectral signatures. To benchmark our instrument and approach, we first checked how accurately we could localize stationary, multifluorescent beads on a coverslip (Figure 3A). A clear shift between detection channels is observed. This is to be expected because chromatic corrections over the large excitation and detection range (488–700 nm) need to be applied. However, even with a well chromatically corrected systems, a registration of the two channels will be necessary to optimize the precision of the data on the nm scale. After applying the transformation matrix (Figure 3A, right panel, see Experimental Section for details), we could localize the beads in both channels with an accuracy of <5 nm and a precision of <15 nm (Figure 3B) in the *x-y* plane. We concentrate here on the axial mapping, as it is significantly influenced by chromatic aberrations. The axial dimension has a chromatic shift of 47 nm, which is fairly independent of the lateral position (Figure S1, Supporting Information).

For the calibration experiments, typical count rates for the individual beads were between 15 and 90 kHz in the blue channel, and between 35 and 400 kHz in the red channel.

In the next step, we mixed two kinds of fluorescent polystyrene beads and tracked them in solution. One kind of bead is 450 nm in size and emits between ≈460 and 540 nm (measured with 488 nm excitation; blue detection channel). The second kind of bead is 560 nm in size and emits between 580 and 650 nm (measured with 561 nm excitation; red detection channel). Representative data from two independently diffusing particles are shown in Figure 4A (blue trace). Further examples are provided in Figure S2 (Supporting Information). The blue particle was constantly tracked over ≈5.0 s with a sensitivity threshold of 5 kHz for position detection (Figure 4A). This threshold defines whether a particle is within the orbit or if the instrument switches to the search algorithm. The measured 3D trajectory is shown in Figure 4B, where the temporal information is color-coded in the trace changing from blue-to-green.

Similarly, the red fluorescence (Figure 4A; red trace) was used to track the 3D position of the second particle. Its

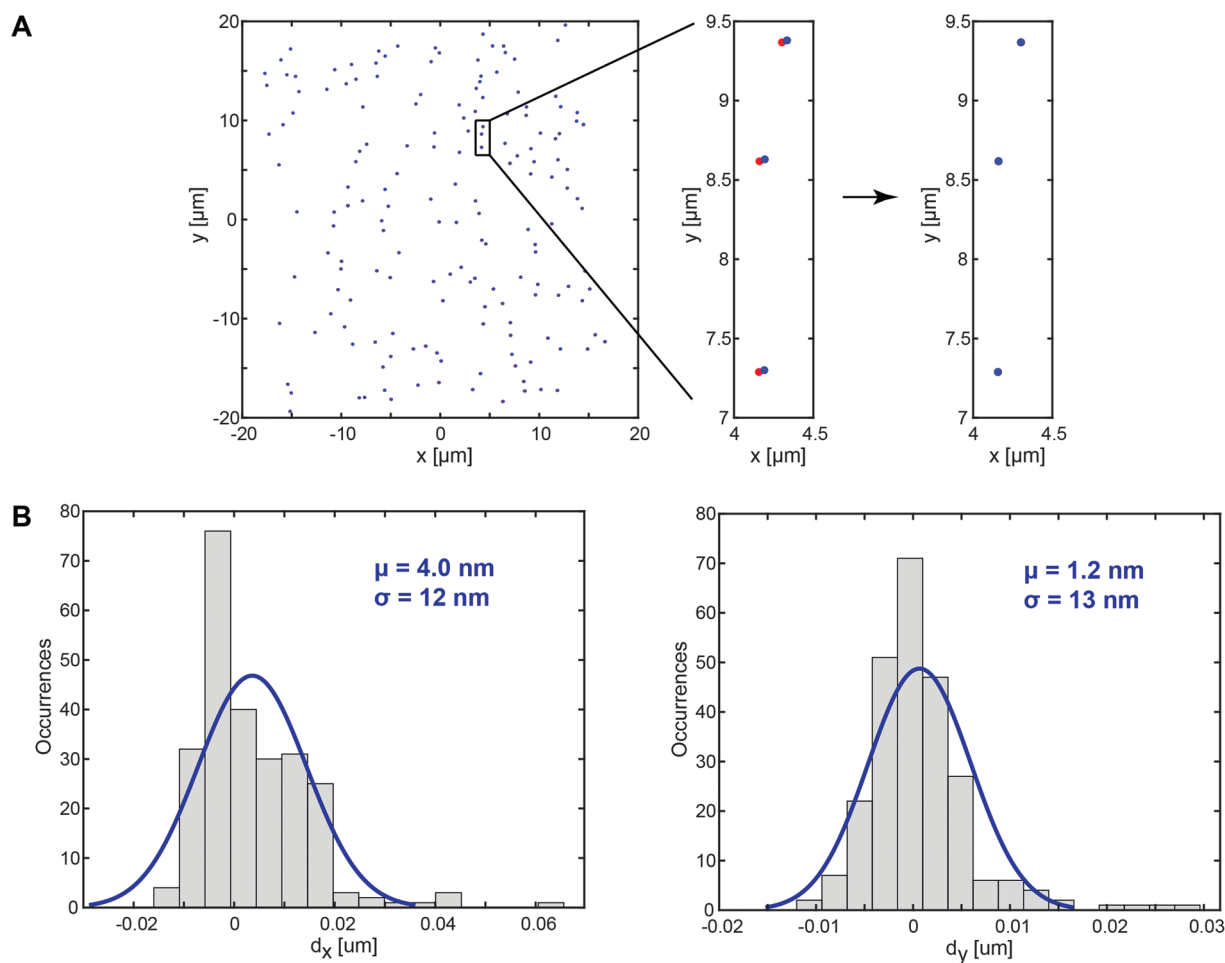


**Figure 3.** Image calibration and corrected registration of the two channels. A) Tracked positions of calibration beads covering the field of view. Red and blue circles represent the center of mass coordinates for the respective channel. The offset between the channels originating from chromatic aberrations is shown in the middle panel. After performing the mapping procedure, the blue detection channel is corrected. B) Histograms of the measured distance between the blue and red signal from individual beads along the x- and y-axis are shown for red-fluorescent beads labeled with Atto488 after applying the image transformation.

corresponding trajectory in solution is shown in Figure 4B. The spirally shaped motions at roughly 3.25 and 3.75 s (shown in light grey) indicate activation of the search algorithm as the corresponding bead was lost by the microscope for a short period of time. This happens when the detected emission falls below the set sensitivity threshold, which occurs more frequently with the red beads due to their approximately fourfold lower intensity. The distance between both particles (Figure 4C) varies during the observation time by  $>20 \mu\text{m}$ . Due to the relatively fast motions of the freely diffusing beads, we only collect one orbit at the previously determined location when alternating between beads. This leads to the large fluctuations observed in Figure 4A. If the objects were moving more slowly or if faster opto-mechanics were utilized in the system, one could perform a few orbits to lock in accurately on the particle, which would decrease the intensity fluctuations. However, as the position of the particle is determined via the phase and modulation of the signal, the absolute intensity does not have a dramatic influence on the location accuracy.

An analysis of the relative movement of both beads clearly indicates that their motions are independent. This can also be seen by comparing the relative and absolute mean-square-displacement (MSD) plots (Figure S3A, Supporting Information). For independent motion, the relative distance has a higher diffusion coefficient than the absolute displacement of either bead. In addition, the MSD (Figure S3A, Supporting Information) also reveals that their diffusion is not dominated by Brownian motion but by turbulence induced upon the addition of the nanoparticles to the imaging buffer. Diffusion with flow is also observed for other example trajectories shown in Figure S2 (Supporting Information). We verified that the turbulence is not introduced by the z-oscillations of the objective switching between particles by performing an MSD analysis on the xy-projected trajectories. Flow is still observable in planes orthogonal to the motion of the piezo. The 3D MSD analysis returned the same average flow rate of  $1.7 \mu\text{m s}^{-1}$  for both particles but was found to decrease over the course of the trajectory. The blue particle has a diffusion coefficient of  $0.84 \pm 0.04 \mu\text{m}^2 \text{s}^{-1}$ , while the red bead diffuses slightly faster with a diffusion coefficient of  $1.03 \pm 0.05 \mu\text{m}^2 \text{s}^{-1}$ . Using

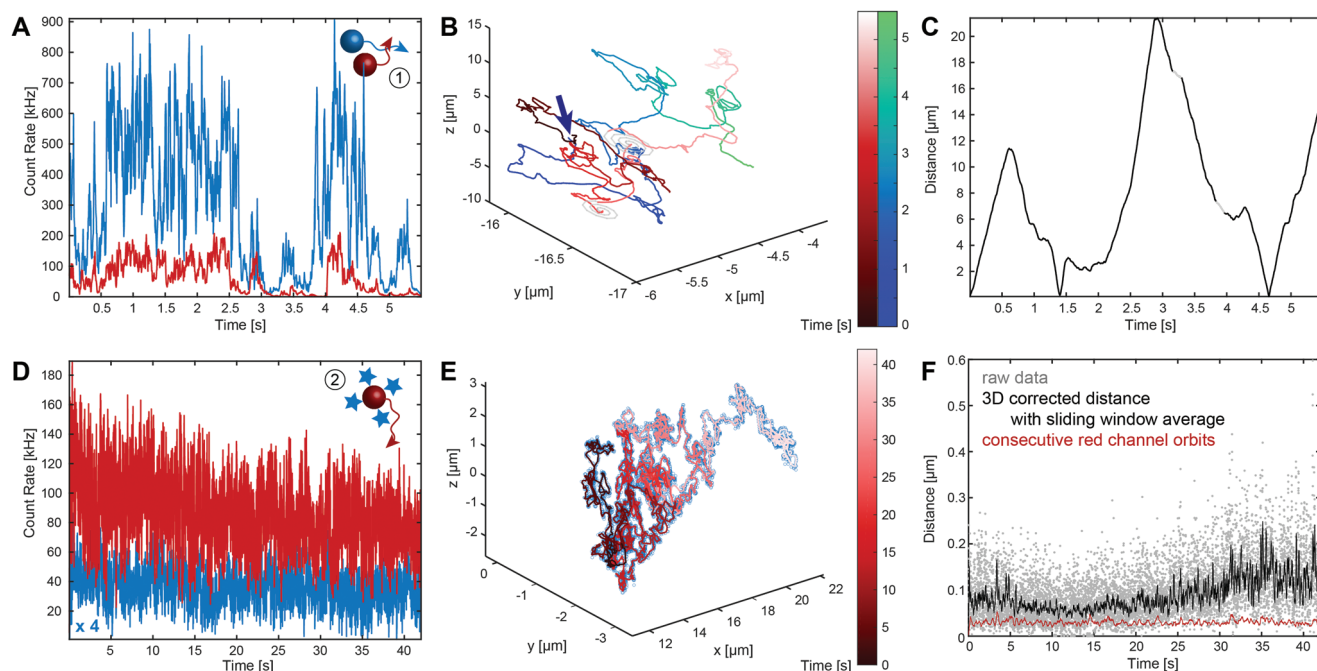


**Figure 4.** Dual-Color Tracking of beads. A–C) Independent motion: A) fluorescence intensities, B) 3D trajectories, and C) relative distance between the two independently diffusing particles. The beginning of the trajectories is indicated by the arrow in panel (B). The particles exhibit separations of up to 20  $\mu\text{m}$ . The blue intensity and blue-to-green color-coded trace correspond to the particle excited at 488 nm. The red signal and the black-to-red color-coded track correspond to the bead excited at 633 nm. The grey data points in panels B and C indicate regions when the red particle was not detected within the orbit. D–F) Correlative motion: D) fluorescence intensities of the red and blue signals corresponding to the fluorescent emission of the bead (with 633 nm excitation) and dye (with 488 nm excitation). To make it more visible, a factor of four has been applied to the intensity of the blue channel. E) A 3D correlated trajectory of a red-emitting bead labeled with Atto488. The red trace represents the position of the red particle and the blue cloud surrounding the trace depicts the localization of Atto488 probed during tracking of the red particle. F) The distance between emission from the red particle and the Atto488 signal (grey). The solid lines represent a sliding window average of 50 orbits for the correlative tracking (black) and for consecutive orbits of the tracking channel (i.e., the red channel in this case shown in red).

the Stokes–Einstein relation, a fixed temperature of 20  $^{\circ}\text{C}$  and the viscosity for pure PBS medium<sup>[33]</sup> at 20  $^{\circ}\text{C}$  of  $\eta = 1.0192 \text{ mPa}\cdot\text{s}$ , the hydrodynamical radius  $r$  of each particle can be estimated. For the blue particle, we found a radius of  $\approx 350 \text{ nm}$  (or 700 nm diameter), and a radius of  $\approx 370 \text{ nm}$  (740 nm diameter) for the red bead. Both values are larger than the average value radius provided by the supplier (Experimental Section) of 225 and 280 nm, respectively. We also measured the size distribution of the beads using scanning electron microscopy (SEM). The dried beads have a size distribution centered  $\approx 200 \text{ nm}$  radius (or 400 nm diameter, Figure S4, Supporting Information) with the blue beads having a slightly larger radius. The hydrodynamic radius determined from orbital tracking deviates from what is expected from the measured particle sizes. However, the absolute values are difficult to compare due to the distribution in bead sizes, protein coating and solvation shell, and uncertainty in the exact solvent composition. We consistently observe a slower diffusion coefficient on average for the larger beads and have the advantage of measuring the diffusion coefficient directly on the tracked bead of interest under the exact experimental conditions.

### 3.2. Correlative Dual-Color Tracking

Often, it is sufficient to measure the distances between two particles when they are interacting, in which case, a correlative

dual-color tracking approach can be used. To implement 3D orbital-tracking of two emitters that show correlative motion, one channel is defined as the leading channel and used for actively tracking one of the particles where the second channel is used to passively localize the second particle. This provides higher localization accuracy with the same time-resolution when the two particles are within the laser orbit radius. Figure 4D,E depicts the intensity (left panel) and 3D trajectory (right panel) of streptavidin-covered red-emitting beads that are coated with biotinylated Atto488 (further examples are given in Figure S5, Supporting Information). The gradient-coded trace (Figure 4E) represents the Brownian motion of the dual-labeled bead. The blue clouds represent the detected emission of the attached Atto488 probed by alternating laser excitation. To verify that scattering is not the origin of this measured signal, control experiments were performed in the absence of Atto488 (Figure S6, Supporting Information) where no signal was detected in the blue channel. As expected for dual-color particles, the distance between both emitters did not change during the tracking experiment (Figure 4F). The relative separation between the particles was found to be  $\lesssim 100 \text{ nm}$ , which is explained by the temporal delay of 5 ms between the alternating orbits. The quasi-identical trajectories share a common diffusion coefficient  $D$  of  $0.11 \mu\text{m}^2 \text{ s}^{-1}$  derived from the MSD analysis (Figure S3B, Supporting Information). The derived hydrodynamic radius  $r = 980 \text{ nm}$  of the Atto488-labeled particle

is significantly larger than the reported radius (290 nm) for the unlabeled red bead, which suggests we were tracking an aggregate in this case.

We observed that the achieved tracking duration for two independent particles is generally shorter than for single-particle tracks as well as dual-color trajectory measured in correlative mode since the instrument has to continually jump between the two particle locations between each orbit. The main limiting factor here is the response time of the z-Piezo nanopositioner for the objective. Hence, the axial position of the particle may not be perfectly matched, leading to a faster loss of the particle. This could be circumvented by decreasing the alternation frequency between the particles. However, this has to be balanced with the motional speed of the particle such that, upon returning to the previously known location, the diffusing particle has a high probability of still being within the orbit.

For tracking correlative motion, the offset between both channels is mainly biased by two phenomena, diffusion and chromatic aberrations originating from the telescope system. Due to the delay between orbits with different excitation wavelengths, there is a shift in the position of the particle. This could be eliminated by combining orbital tracking with pulsed interleaved excitation.<sup>[34]</sup> Chromatic aberrations of the telescope system can also be corrected for to some extent via calibration and applying a mapping algorithm. In this case, specially designed telescope lens can be implemented to dramatically improve the overlap between the two channels as we have recently demonstrated on a laser scanning confocal microscope setup.<sup>[27]</sup>

### 3.3. Spectroscopic Readout during 3D Orbital Tracking

Next, we expanded our dual-color 3D orbital tracking approach to allow spectroscopic investigations in the second channel. In particular, we performed single-pair FRET measurements on diffusing particles. Here, we replaced the 50/50 beamsplitter used above with a dichroic mirror in the second channel such that we can measure single-molecule FRET while tracking the sample in the first channel (Figure 2B). For these experiments, double-labeled, double-stranded DNA (dsDNA) was linked to the surface of streptavidin-coated silica beads (0.48  $\mu\text{m}$  diameter), which were labeled with Atto488-biotin (at a ratio of 1:20). To minimize multiple DNA strands being bound to the same particle, an oligonucleotide concentration of 5  $\mu\text{M}$  was used during incubation with the labeled bead. The Atto488 fluorescence was used for tracking while spFRET was measured between the FRET pair Atto565 and Atto647N attached to the dsDNA.

#### 3.3.1. Sample Characterization by MFD-PIE

Before performing the orbital tracking experiments, we characterized the dsDNA samples in solution using multiparameter fluorescence detection<sup>[35]</sup> with pulsed interleaved excitation<sup>[34]</sup> (MFD-PIE; see Experimental Section).<sup>[25]</sup> Three dsDNA strands labeled at different positions were used to generate a low, inter-

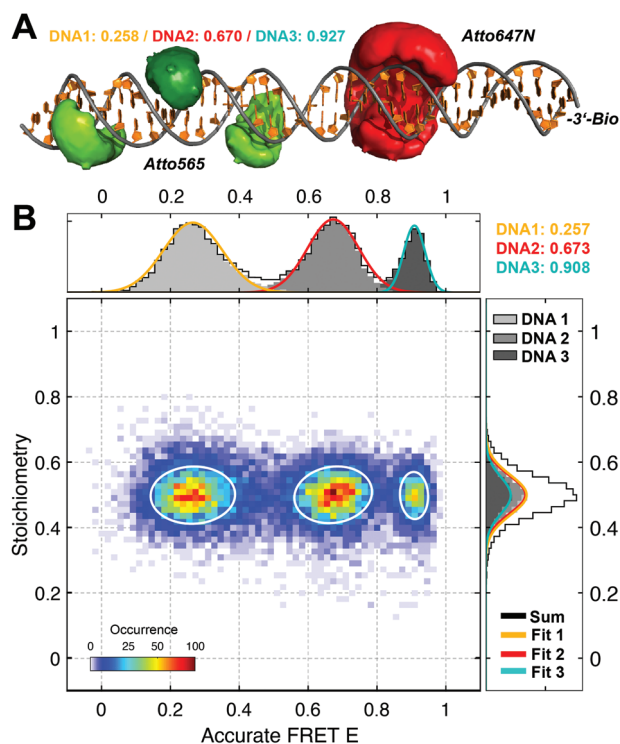


**Figure 5.** Characterization of dsDNA oligonucleotides serving as FRET standards. A) Depiction of location of the donor and acceptor fluorophores using an AV simulation on double-labeled dsDNA. The red and green clouds along the helix mark the accessible positions of the acceptor Atto647N (base pair 27, top strand) and donor Atto565 (base pair 6, 12, 18 on the bottom strand), respectively. The expected FRET efficiencies from the AV simulations are 0.258, 0.670, and 0.927 for the low, middle, and high FRET constructs respectively. B) An accumulative stoichiometry versus FRET efficiency plot of the three dsDNA constructs. Accurate FRET efficiencies of 0.257, 0.673, and 0.908 were determined for the FRET constructs.

mediate, and a high FRET signal (Figure 5A and Scheme 1). The top strand was labeled with an acceptor fluorophore Atto647N (at position 27) and was biotinylated at the 3'-end for immobilization on the silica beads. The bottom strand carries the donor fluorophore Atto565 at either position 6 (DNA1), position 12 (DNA2) or position 18 (DNA3). The accessible positions of the attached dyes along the DNA were determined using AV simulations<sup>[36]</sup> (Figure S7, Supporting Information) and are depicted as red or green clouds along the DNA helix in Figure 5A.

According to the AV calculations, the theoretical FRET values for the three FRET constructs are 0.258 (DNA1; low), 0.670 (DNA2; middle), and 0.927 (DNA3; high). Figure 5B shows the obtained, accurate FRET histograms of each species with efficiencies of 0.257, 0.673, and 0.908. The predicted and measured values are in excellent agreement (Table 1).

#### 3.3.2. Correlated 3D FRET-Tracking Experiments

Having calibrated the dsDNA constructs with MFD-PIE, we then measured the FRET state of dsDNAs attached to beads diffusing in solution using 3D orbital tracking. For this modality, a four-orbit excitation/detection scheme was used

**Table 1.** FRET values obtained from 3D Orbital Tracking, MFD-PIE experiments, and AV Simulations.

$R_0 = 68 \text{ \AA}$	FRET Efficiency	3D OT	3D OT (altern.)	PIE-MFD	AV Simulation
Gamma $\gamma$	—	1.37	0.7	0.61	—
DNA 1	Low	0.151	0.257	0.257	0.258
DNA 2	Middle	0.473	0.631	0.673	0.670
DNA 3	High	0.632	0.806	0.908	0.927

(Figure 2E): 1) tracking orbit (488 nm excitation) with position update, 2) the emission readout after acceptor excitation to probe the presence and photophysical state of the acceptor fluorophore (633 nm excitation) with no position update, 3) tracking orbit with repositioning (488 nm excitation) and 4) the FRET readout, i.e., dual-color emission after donor excitation (with 561 nm) (see Experimental Section). With this approach, we gather the diffusion information as well as

spFRET data with alternating laser excitation to monitor the presence and photophysical state of the acceptor.<sup>[29,37]</sup>

The trajectory of the diffusing particles (Figure 6A–C) showed the expected Brownian motion of the particles in solution. The determined hydrodynamic radius ( $\approx 800 \text{ nm}$ ), determined from the distribution of diffusion coefficients, is centered around  $\approx 0.17 \mu\text{m}^2 \text{ s}^{-1}$  (Figure S8A, Supporting Information) and again slower than expected. Using fluorescence correlation

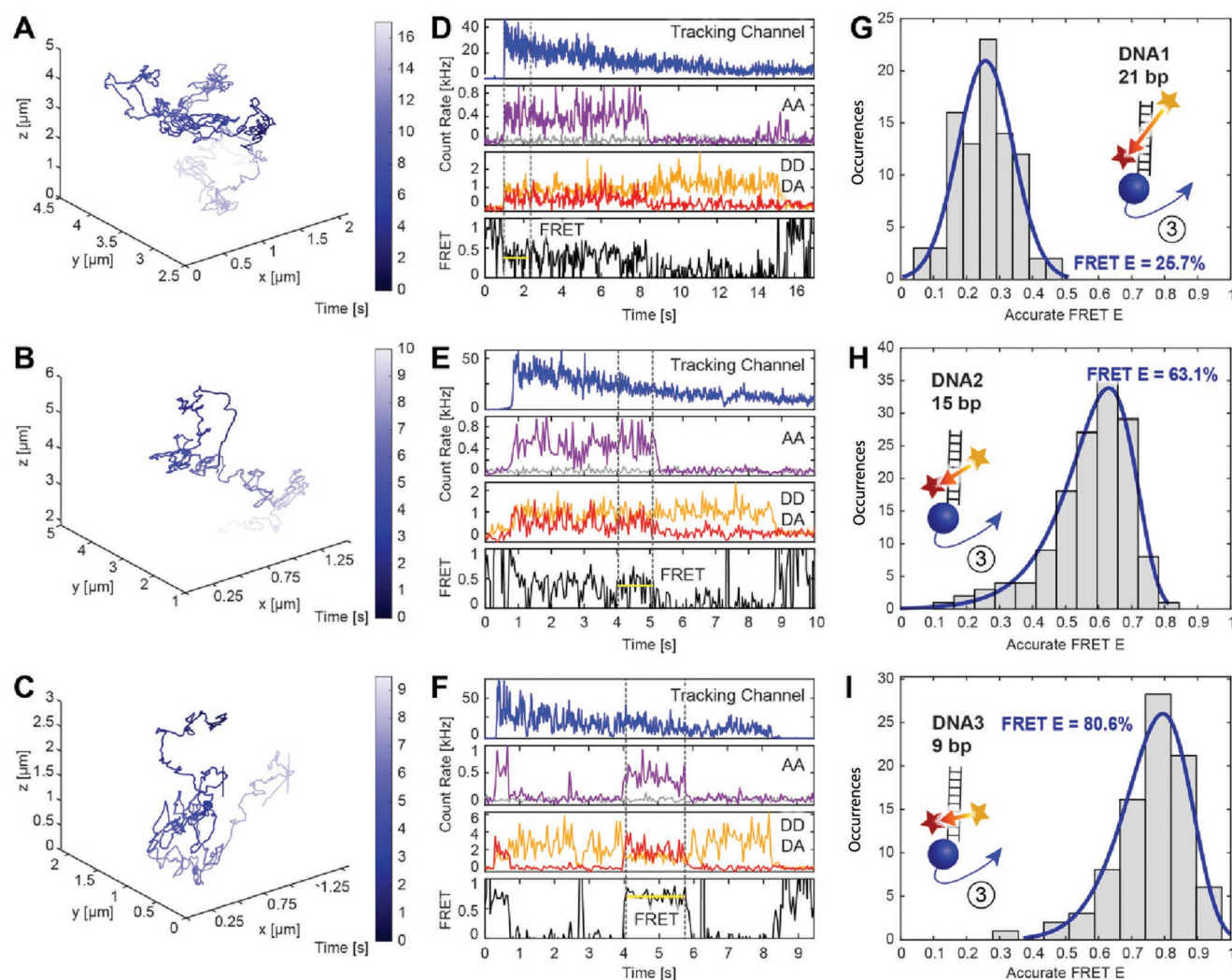


**Figure 6.** Single-molecule FRET measurements on diffusing DNA molecules. While tracking the reference beads marked with Atto488 dyes in solution panel (A–C), we monitored the signature of single DNA-based FRET standards panel (D–F) that were attached to the particle via a biotin-streptavidin interaction. The dsDNA oligos were double-labeled with Atto565 and Atto647N. The donor dye was positioned at three different distances with respect to the acceptor dye. The resulting oligos are characterized by a G) low FRET value of  $\approx 26\%$  (DNA1), H) an intermediate FRET value of  $63\%$  (DNA2), and I) a high FRET value of  $81\%$  (DNA3).



spectroscopy to study the diffusional behavior of the Atto488-labeled silica beads alone (Figure S8B, Supporting Information), we could confirm these results and further show that labeled particles dispersed in imaging buffer also tend to aggregate as seen from the tail at long lag times. This increased particle size due to the protein corona and glycerol was further observed in DLS experiments (Figure S9, Supporting Information). In addition, SEM reveals a substantial contribution of non-spherical joint silica particles with an extended length between 400 and 700 nm (Figure S10, Supporting Information), which would decrease the measured diffusion coefficient. Given the variety of characterization methods and sensitivities, these findings highlight the strength of our 3D Orbital tracking approach, which provides a direct readout on the diffusional properties of the individual particles being tracked.

The corresponding fluorescent intensities for the particles measured in Figure 6A–C are shown in Figure 6D–F. The blue intensities correspond to the tracking channel, the purple signal to acceptor emission after 633 nm excitation (ALEX channel or AA channel), and the orange (DD channel) and red intensities (DA channel) correspond to the Atto565 (donor) and Atto647N (acceptor) signal after donor excitation, respectively. As seen in Figure 6D–F, the Atto488 signal in the tracking channel comes from  $\approx 25$  to 30 Atto488 molecules (estimated using an average brightness of 1.5 kHz per emitter) that are photobleaching over time while tracking the motion of the bead. The donor and acceptor signal intensities were examined from experiments where single-step photobleaching events were observed. These traces and those exhibiting a similar intensity range were further analyzed. This ensured that only a single dsDNA was present on the bead. The signals were then background corrected for Rayleigh scattering of the laser light, estimated from beads not containing dsDNA strands, and further corrected for direct excitation ( $\alpha = 0.47$ ), spectral cross talk ( $\beta = 0.21$ ) and the detection efficiency  $\gamma$ .<sup>[29,37–39]</sup> The correction against direct excitation and spectral cross talk (see Material Section) could be reliably carried out by applying the mean values  $\bar{\alpha}$  and  $\bar{\beta}$  to all recorded FRET traces (Figure S11A,B, Supporting Information).

Determination of the detection correction factor  $\bar{\gamma}$ , however, is more challenging. The obtained  $\gamma$  values are particle-dependent and varied between 0 and 4 with an average value of 1.37 (determined from acceptor photobleaching steps, Figure S11C, Supporting Information). However, this value is too large for the filters used in the instrument and leads to an underestimation of the FRET values by 15–30%. The difficulties in determining  $\gamma$  are due to several factors. Chromatic aberrations and geometric mismatch of the excitation volumes lead to biases in the detection efficiency and thus to a position-dependent  $\gamma$  factor. Scattering from the bead to which the dsDNA is attached depends on the position of the particle in the orbit as well as the size and morphology of the bead. Hence, correct subtraction of the scattering for the individual beads is challenging. Moreover, in contrast to PIE/nsALEX<sup>[33,40]</sup> and  $\mu$ sALEX<sup>[37]</sup> single-molecule experiments, the 5 ms alternating timescale of moving objects leads to a broadening of the measured stoichiometry value, which makes it unusable for the determination of the detection correction factor  $\bar{\gamma}$ .<sup>[29]</sup>

As an alternative, we used the  $\gamma$  factor from the MFD-PIE instrument, which incorporates very similar filters and detectors ( $\bar{\gamma} = 0.7$  Table 1). Using this detection correction factor, we obtained values of 25.7%, 63.1%, and 80.6% for the low, intermediate, and high FRET constructs. The low and intermediate FRET values are well in line with the MFD-PIE data and the expected results from AV simulations. The high FRET efficiency value deviates more than it should but is clearly distinguishable from the other two constructs.

#### 4. Discussion

By expanding the number of fluorescence species that can be tracked at a time, the amount of information collected in a single experiment can be greatly enhanced. Using a second detection channel, 3D orbital tracking is capable of following the position and thereby distance between two spectrally distinct particles either independently or within the vicinity of one of the species. In addition, the second channel can also be used for performing spectroscopy (spFRET in this case) on the tracked particle.

In the first mode, we were able to track both particles independently with separations of over 20  $\mu\text{m}$ . Other recently published dual-color approaches are only able to track two particles when they are within the detection volume of the microscope.<sup>[23,24]</sup> From the 3D trajectories, the typical information such as the hydrodynamic radius of individual particles and diffusional kinetics can be monitored with time. However, the independent, dual-color tracks were generally restricted to shorter measurement times before being lost by the setup due to the repositioning of the optical devices. In particular, the piezo stage for the objective used to follow the  $z$  motion of the particle has a response time on the  $\approx 10$  ms timescale.

In the current configuration, the system is capable of robustly tracking molecules with diffusion coefficients up to  $\approx 1\text{--}2 \mu\text{m}^2 \text{s}^{-1}$ . For a diffusion coefficient of  $1 \mu\text{m}^2 \text{s}^{-1}$ , there is a 0.2% chance of the particle moving  $\geq 500$  nm (out of the orbit radius) within 10 ms, in which case the microscope will lose the particle in the lateral direction. The piezo stage used for moving the objective is the element in the system that limits the overall 3D tracking speed. Hence, the particle will be lost after a few seconds (Figure S12, Supporting Information). When tracking a single particle, it is only necessary to move the objective by the distance the particle has moved in  $z$ . However, when independently tracking two particles, the objective needs to oscillate between the two different  $z$  positions. With the slow response time of the piezo combined with our orbit time of 5 ms, the system in its current implementation has difficulties following rapidly diffusing particles in three dimensions for long periods of time. This could be improved by replacing the piezo with an electronically tunable lens, as has been shown by Annibale et al.<sup>[41]</sup> Replacing a piezo nanopositioner with an electronically tunable lens for  $z$ -tracking in 3D orbital tracking has led to more than a tenfold increase in response time of the system. In this configuration, one could consider replacing the water objective with a high NA oil objective to collect more photons as the objective is not moving during tracking.

When one is not pushing the temporal limits of the system, multiple orbits can be performed on each particle to properly “lock-in”, which would decrease the fluorescence fluctuations observed during tracking (e.g., in Figure 4A). However, the position of the particle is determined from the modulation of the signal during the orbit and the difference in intensity between the different z-planes. Hence, the

tracking precision is much less affected by the fluctuations in intensity.

We would like to mention that the microscope was designed for measuring processes in live cells or organisms.<sup>[12,15]</sup> To demonstrate this, we followed the endocytosis of “purple” fluorescent silica beads in HuH7 cells (Figure 7A). Figure 7B shows the trajectory of a bead uptaken by an early endosome and its

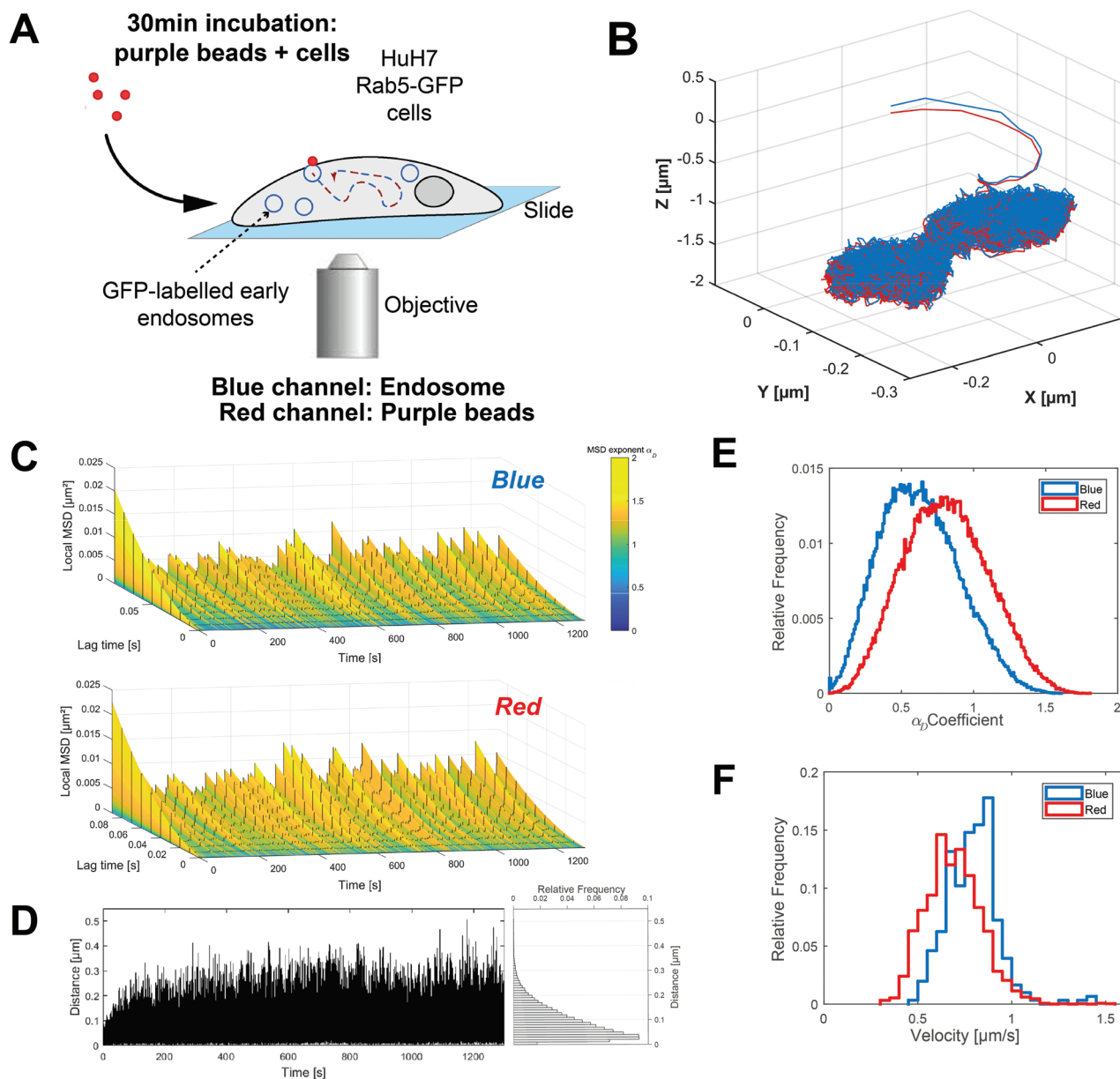


**Figure 7.** Long-duration dual-color tracking of a bead during endocytosis. A) The principle of the experiment: polystyrene beads (Red, 633 nm laser excitation) are incubated with HuH7 cells expressing the fluorescently tagged marker Rab5-GFP for early endosomes (blue, 488 nm laser excitation) at room temperature. B) The corresponding trajectory is represented as a 3D plot showing a fast uptake followed by transport and diffusion within the cytosol over 22 min. C) The corresponding MSD plots obtained along the trajectory using a sliding window are plotted in 3D. The values of the  $\alpha_D$ -coefficient calculated with the equation (Equation 8) are encoded in color. The value characterizes the type of diffusion the particles exhibit: an  $\alpha_D$ -coefficient  $<1$  indicates sub-diffusion,  $\approx 1$  for random diffusion, and  $>1$  super-diffusion. Each value was determined by fitting the MSD function for every time point  $t$ . D) The chromatically corrected distances between the two particles were calculated along the trajectory as a function of time. A relative frequency histogram is plotted to the right. E) The distribution of  $\alpha_D$ -coefficients is shown for the bead in red and the endosome in blue. F) For regions containing  $\alpha_D > 1.4$ , we plot the distribution of extracted velocities (See Experimental Section for details). The velocities are between 0.5 and  $1 \mu\text{m s}^{-1}$ , which is a typical range for transport processes in cells.

transport within the endosome through the cell. The trajectory was collected over >20 min yielding more than 120,000 data points that were analyzed in both channels. By performing a sliding window MSD analysis along the trajectory, we could identify regions of directed transport interspersed with pauses or random motion (Figure 7C). We also investigated the separation between the position of the endosome and the bead (Figure 7D). The typical separation is  $\approx 20$  nm with occasional fluctuations to larger distances. As we expect the two objects to colocalize, the separation of 20 nm can be interpreted as an upper limit of the precision of the independent tracking modality in a living cell. The distribution of determined exponent,  $\alpha_D$ , and the velocities during transport are shown in Figure 7E,F (see Experimental Section for details). This provides a glimpse of the type of information the two-color, 3D orbital tracking system can provide in a cellular environment.

For most biological processes in living cells, the response time of the system is sufficient. In addition, the axial travel range of objects in cells tends to be limited.

For determination of the  $z$  position, we split the observation into two planes. As for any bi-plane technique, this leads to a trade off in photons detected in each focal plane for increased temporal resolution. Alternatively, one can oscillate the objective and measure orbits above and then below the laser focus, as has been done previously using 2-photon excitation.<sup>[14]</sup> For determination of the  $x$  and  $y$  position, we sum the photons from both detectors together before calculating the radial position. Hence, the loss of sensitivity for  $x$ - $y$  detection is minimal. Unfortunately, there is currently no convenient and efficient way of separating photons being emitted from two focal planes spaced  $\approx 200$  nm apart.

In the second mode, one spectral channel can be used for tracking while the fluorescence of another species is probed during alternating orbits. This improves the robustness of tracking algorithm while the instrument is focused on following a single particle and not jumping between locations. This modality is similar to the extended TSUNAMI approach<sup>[23]</sup> with similar precision, and the spatial distance between both species encodes information regarding conformational changes of the tracked particle. For our system, there were no conformational changes and the distance was constant as expected.

By modifying the second tracking channel and the data collection software, we could successfully combine 3D orbital tracking experiments with single-molecule-sensitive FRET detection. In contrast to the tetrahedral approach,<sup>[24]</sup> by alternating the corresponding laser lines and our novel detection algorithm, we could determine the FRET correction factors of the species and thereby calculate an accurate FRET efficiency. For the very high-FRET construct, we did have discrepancies in the determined accurate FRET value. Measuring accurate FRET when the dyes are in very close proximity is very tricky. First of all, the signal from the donor fluorophore is low and accurate correction of the background signal is necessary for an accurate estimation of the FRET efficiency. At short distances, other phenomena such as Dexter transfer or dye-dye quenching can influence the FRET measurement. In addition, as we already discussed, the 10 ms delay between the FRET and the ALEX measurements biases the calculation of the correction factor for detection efficiency.

The three modalities united within one single setup represent an advanced and biophysical tool that opens the possibility

to monitor the interaction of freely diffusing reaction partners, such as an endosome on a microtubule. In addition, spFRET can be accurately measured on an actively tracked object.

## Supporting Information

Supporting Information is available from the Wiley Online Library or from the author.

## Acknowledgements

The authors are indebted to Christoph Zimmermann from the group of Olivia Merkel for assisting with dynamic light scattering experiments and Benjamin März from the laboratory of Knut Müller-Caspar for collecting the electron microscopy images. The authors thank Dr. Nadia Ruthardt for providing the HuH7 Rab5-GFP cell lines. The authors gratefully acknowledge the financial support from the Deutsche Forschungsgemeinschaft (DFG, German Research Foundation) – Project-ID 201269156 – SFB 1032 Project B03 to D.C.L. and PL 696/4-1 to E.P. and funding by the Federal Ministry of Education and Research (BMBF) and the Free State of Bavaria under the Excellence Strategy of the Federal Government and the Länder through the ONE MUNICH Project Munich Multiscale Biofabrication. The authors also thankfully acknowledge the support of the Excellence Clusters Nanosystems Initiative Munich (NIM) and the LMU via the Center of NanoScience Munich (CeNS) and the LMU innovative Bioluminescence Network. F.M. and D.C.L. are eternally indebted to the coffee machine.

Open access funding enabled and organized by Projekt DEAL.

## Conflict of Interest

The authors declare no conflict of interest.

## Author Contributions

The project was conceived by and carried out under the supervision of D.C.L. F.W. added a second detection channel to the 3D orbital tracking microscope. F.M. programmed the data acquisition and data evaluation software, designed the bead assay, and carried out the tracking experiments in vitro. E.P. designed, prepared, and characterized the FRET standards using PIE-MFD and performed accessible volume calculations and DNA simulations. V.R. designed the in cellulo assay, carried out the associated tracking experiment and characterized the beads using FCS. F.M., E.P., V.R. and D.C.L. analyzed and interpreted the data. F.M., V.R. and E.P. designed the figures. F.M., E.P., V.R. and D.C.L. wrote the manuscript.

## Data Availability Statement

The data that support the findings of this study are available from the corresponding author upon reasonable request.

## Keywords

active feedback tracking, dual-color tracking, Förster resonance energy transfer (FRET), real-time three-dimensional (3D) single particle tracking, single molecule spectroscopy

Received: August 2, 2022

Revised: December 23, 2022

Published online: January 29, 2023

- [1] H. C. Berg, *Rev. Sci. Instrum.* **1971**, *42*, 868.
- [2] S. Ram, D. Kim, R. J. Ober, E. S. Ward, *Biophys. J.* **2012**, *103*, 1594.
- [3] M. Speidel, A. Jonáš, E.-L. Florin, *Opt. Lett.* **2003**, *28*, 69.
- [4] S. R. P. Pavani, M. A. Thompson, J. S. Biteen, S. J. Lord, N. Liu, R. J. Twieg, R. Piestun, W. E. Moerner, *Proc. Natl. Acad. Sci. USA* **2009**, *106*, 2995.
- [5] Y. Shechtman, L. E. Weiss, A. S. Backer, S. J. Sahl, W. E. Moerner, *Nano Lett.* **2015**, *15*, 4194.
- [6] G. A. Lessard, P. M. Goodwin, J. H. Werner, *Appl. Phys. Lett.* **2007**, *91*, 224106.
- [7] E. P. Perillo, Y.-L. Liu, K. Huynh, C. Liu, C.-K. Chou, M.-C. Hung, H.-C. Yeh, A. K. Dunn, *Nat. Commun.* **2015**, *6*, 7874.
- [8] S. Hou, J. Exell, K. Welsher, *Nat. Commun.* **2020**, *11*, 3607.
- [9] F. Balzarotti, Y. Eilers, K. C. Gwosch, A. H. Gynná, V. Westphal, F. D. Stefani, J. Elf, S. W. Hell, *Science* **2017**, *355*, 606.
- [10] L. A. Masullo, F. Steiner, J. Zähringer, L. F. Lopez, J. Bohlen, L. Richter, F. Cole, P. Tinnefeld, F. D. Stefani, *Nano Lett.* **2021**, *21*, 840.
- [11] C. Hellriegel, E. Gratton, *J. R. Soc., Interface* **2009**, *6*, S3.
- [12] F. Wehnekamp, G. Plucińska, R. Thong, T. Misgeld, D. C. Lamb, *Elife* **2019**, *8*, e46059.
- [13] J. Enderlein, *Appl. Phys. B* **2000**, *71*, 773.
- [14] V. Levi, Q. Ruan, K. Kis-Petikova, E. Gratton, *Biochem. Soc. Trans.* **2003**, *31*, 997.
- [15] I. Verdeny-Vilanova, F. Wehnekamp, N. Mohan, Á. S. Álvarez, J. S. Borbely, J. J. Otterstrom, D. C. Lamb, M. Lakadamyali, *J. Cell Sci.* **2017**, *130*, 1904.
- [16] F. Begarani, F. D'aulia, G. Signore, A. Del Grosso, M. Cecchini, E. Gratton, F. Beltram, F. Cardarelli, *ACS Nano* **2019**, *13*, 1670.
- [17] M. Gabriel, A. Anzalone, E. Gratton, L. C. Estrada, *Microsc. Res. Tech.* **2019**, *82*, 1835.
- [18] K. McHale, H. Mabuchi, *J. Am. Chem. Soc.* **2009**, *131*, 17901.
- [19] Y. Yu, Y. Gao, Y. Yu, *ACS Nano* **2018**, *12*, 11871.
- [20] Y. Ding, C. Li, *Biomed. Opt. Express* **2016**, *7*, 4187.
- [21] D. Albrecht, C. M. Winterflood, H. Ewers, *Methods Appl. Fluoresc.* **2015**, *3*, 024001.
- [22] K. Kis-Petikova, E. Gratton, *Microsc. Res. Tech.* **2004**, *63*, 34.
- [23] Y.-L. Liu, E. P. Perillo, P. Ang, M. Kim, D. T. Nguyen, K. Blocher, Y.-A. Chen, C. Liu, A. M. Hassan, H. T. Vu, Y.-I. Chen, A. K. Dunn, H.-C. Yeh, *ACS Nano* **2020**, *14*, 7927.
- [24] A. M. Keller, M. S. Devore, D. G. Stich, D. M. Vu, T. Causgrove, J. H. Werner, *Anal. Chem.* **2018**, *90*, 6109.
- [25] V. Kudryavtsev, M. Sikor, S. Kalinin, D. Mokranjac, C. A. M. Seidel, D. C. Lamb, *ChemPhysChem* **2012**, *13*, 1060.
- [26] F. Mieskes, F. Wehnekamp, G. Plucińska, R. Thong, T. Misgeld, D. C. Lamb, *Data Brief* **2020**, *29*, 105280.
- [27] N. Al Danaf, Ph.D. Thesis, *Advanced Fluorescence Methodologies for the Exploration of the Nanoworld*, Ludwig-Maximilians-Universität München, Germany, **2021**.
- [28] A. Dupont, M. Gorelashvili, V. Schüller, F. Wehnekamp, D. Arcizet, Y. Katayama, D. C. Lamb, D. Heinrich, *New J. Phys.* **2013**, *15*, 075008.
- [29] N. K. Lee, A. N. Kapanidis, Y. Wang, X. Michalet, J. Mukhopadhyay, R. H. Ebright, S. Weiss, *Biophys. J.* **2005**, *88*, 2939.
- [30] W. Schrimpf, A. Barth, J. Hendrix, D. C. Lamb, *Biophys. J.* **2018**, *114*, 1518.
- [31] T. E. Tomov, R. Tsukanov, R. Masoud, M. Liber, N. Plavner, E. Nir, *Biophys. J.* **2012**, *102*, 1163.
- [32] V. Levi, Q. Ruan, E. Gratton, *Biophys. J.* **2005**, *88*, 2919.
- [33] P. Toonkool, D. G. Regan, P. W. Kuchel, M. B. Morris, A. S. Weiss, *J. Biol. Chem.* **2001**, *276*, 28042.
- [34] B. K. Müller, E. Zaychikov, C. Bräuchle, D. C. Lamb, *Biophys. J.* **2005**, *89*, 3508.
- [35] J. Widengren, V. Kudryavtsev, M. Antonik, S. Berger, M. Gerken, C. A. M. Seidel, *Anal. Chem.* **2006**, *78*, 2039.
- [36] S. Kalinin, T. Peulen, S. Sindbert, P. J. Rothwell, S. Berger, T. Restle, R. S. Goody, H. Gohlke, C. A. M. Seidel, *Nat. Methods* **2012**, *9*, 1218.
- [37] A. N. Kapanidis, N. K. Lee, T. A. Laurence, S. Doose, E. Margeat, S. Weiss, *Proc. Natl. Acad. Sci. USA* **2004**, *101*, 8936.
- [38] E. Lerner, A. Barth, J. Hendrix, B. Ambrose, V. Birkedal, S. C. Blanchard, R. Börner, H. Sung Chung, T. Cordes, T. D. Craggs, A. A. Deniz, J. Diao, J. Fei, R. L. Gonzalez, I. V. Gopich, T. Ha, C. A. Hanke, G. Haran, N. S. Hatzakis, S. Hohng, S.-C. Hong, T. Hugel, A. Ingargiola, C. Joo, A. N. Kapanidis, H. D. Kim, T. Laurence, N. Ki Lee, T.-H. Lee, E. A. Lemke, et al., *Elife* **2021**, *10*, e60416.
- [39] C.-B. Salem, E. Ploetz, D. C. Lamb, in *Spectroscopy and Dynamics of Single Molecules*, (Ed.: C. K. Johnson), Elsevier, Amsterdam **2019**, pp. 71–115.
- [40] A. N. Kapanidis, T. A. Laurence, N. K. Lee, E. Margeat, X. Kong, S. Weiss, *Acc. Chem. Res.* **2005**, *38*, 523.
- [41] P. Annibale, A. Dvornikov, E. Gratton, *Biomed. Opt. Exp.* **2015**, *6*, 2181.

## Appendix B

---

# Acknowledgments

As many of you might know, a PhD thesis is not an easy going short trip but a long time journey that can't be done alone. Taking the time after I left the lab into account, this journey took me seven years until writing these words. This might sound as a long time, but being among the right people it does not feel like that.

First of all, I would like to thank you Don for the opportunity to to make this all happen. Thank you for your trust and the freedom to realize the combined Tracking/FRET approach, especially when the project was really struggling. Our coffee battles were so much fun, even though there was a period of time where the coffee consumption reached an unhealthy quantity. Unfortunately, there is still one unanswered question: why the heck is it called American FOOTball, when the ball is barely touched by any foot?!

Secondly, I would also like to thank you Philip. Not only for being so kind to agree on being second supervisor of the thesis, but also for implementing football as an afterwork activity throughout different lab groups and departments.

Furthermore, a very big thank you to Prof. Paul Wiseman, Prof. Laura Estrada, Prof. Dr. Knut Müller-Caspary and Prof. Achim Hartschuh for being part of my committee. Of course acknowledgments are no acknowledgments without mentioning FABLab. First I want thank the "old" generation. Nader, we had great time on the 25th PicoQuant workshop in Berlin. I remember, when we entered the exhibition room and you literally knew every employee of the company. I am happy to be part you your transition to Siegmund aka Siggi...hopefully, you wear your white socks with pride ;).

Vanessa thanks for successfully distracting me from work, especially when we sat in same office :D. Even though I couldn't understand, why you moved from the best office in the world to another one, but I guess, Karma hit back with the "never repaired" blender :P. I appreciate all of our gossiping sessions during lunch or in BioSys during incubation times...and of course all our Leberschuss games.

Adrian, what can I say? I appreciate all of our uncountable "after experiments" beer, darts and Schafkopf sessions in all possible permutations. I will never forget this legendary football game of our teams back in the days, when they were still in the same league. I am still wondering how the speaker did not break when you shouted in it: "Was für eine sch\*\*\*\* Woche....und Corona ist dabei mein kleinstes Problem!" :D

Special thanks to Evelyn. I learned a lot during our discussions either in your office or in the Tinnefeld kitchen. Whenever my thoughts were stuck in a dead-end, you always sacrificed a few minutes of your time for me to push me back on track. Furthermore, thanks for showing me the interesting and super confusing world of Stimulated Raman.

## *Appendix B Acknowledgments*

I will never forget this Friday evening when we for the first time got Stimulated Raman signal on the setup with the new software...priceless faces of the others on the floor, when we ran out of lab screaming from happiness :D.

Furthermore, I appreciate that FabLAB is in good hands of the new generation. Pooyeh, the calm soul of the lab. Whenever it was busy like hell and people would go crazy, you drowned stoically. I guess we were the A-Team grouping up for the three color origamis and the IR upgrade for the TIRF setup. Pleeeeeease, don't lose your skill of nailing almost every situation with the perfect sarcastic comment! :D

Irene...sorry...EHHH GIABALDI! :D Unfortunately, we did not share any projects, but doesn't matter. We just hanged out in kitchen after work for discussing and gossiping literally everything, making it even more fun by triggering you with my stereotypic jokes. Thanks again for the Sambuca supply chain from Italy.

Ecenaz, my office buddy! I really enjoyed the time in our office. We had great discussions. Some were of scientific and some of non-scientific topics. Some of the non-scientific talks were gossip, but the majority was about proper food! Unfortunately, we did not share the office earlier.

Yooo Knechtel! Thanks for our after lunch sessions at the darts board. It was a pleasure to show you how to throw darts properly! :P It was a pleasure to work with you during the implementation of Stimulated Raman. But we still have to talk about this weird blue desktop on the setup computer...

Virgile aka Dr. Advice aka the new care taker of the tracking setup. It's good to know, that the setup is in good hands. And always remember: if it does not behave, shout at it! If it still does not behave, it tries to tell you that you have spend enough time with it for that day and you should go back to the surface. I remember the moment, when I showed you Obadzda for the first time. You had so much happiness in your eyes!

Of course, special thanks to building E. First of all Moritz, master of the bills, who takes care that all bills are paid in time. When taking over the lab order duty in the group, I could totally understand your darkest and sarcastic humor about this bureaucracy. Special thanks to a big group of people from building E: Alex, Veit, Johann, Kristina, Tim, Sarah, Viki, Lennart, Flosel, Stefan, Mario and Jonas. I will keep it short...we had an amazing time during the monday meetings and/or after work!

Finally, I want to thank my family. First of all my parents, Antonella and Rainer. You not only encouraged me to start my studies at LMU but constantly supported me during the whole time. Furthermore, I want to say thank you to my aunt Ute and uncle Klaus as well as my grandma Anneliese for giving me the strength in hard times. And of course a big thank to you Katya that we go through all our ups and especially downs together.